Republic of Iraq
Ministry of Higher Education and Scientific Research
University of Babylon
College of Sciences for Women/Department of Laser Physics

Preparation and Studying the Structural and Optical Properties TeO_2/CdO/G Nanocomposite Prepared by Laser Ablation

A Thesis

Submitted to the Council of the College of Sciences for Women at the University of Babylon in Partial Fulfillment of the Requirements for the degree of Master Science in Laser Physics

By:

Ghusoon Saeed Jaber

(B.Sc. , Physics) (2013)

Supervised by:

Assist.prof. Mohammed Hamza AL- Mamoori *Prof.Dr. Kaiser Neama Madlum*

2022 A.D **1444 A.H**

بسم الله الرحمن الرحيم

﴿ وَعِندَهُ مَفَاتِحُ الْغَيْبِ لَا يَعْلَمُهَا إِلَّا هُوَ وَيَعْلَمُ مَا
فِي الْبَرِّ وَالْبَحْرِ وَمَا تَسْقُطُ مِن وَرَقَةٍ إِلَّا يَعْلَمُهَا وَلَا حَبَّةٍ
فِي ظُلُمَاتِ الْأَرْضِ وَلَا رَطْبٍ وَلَا يَابِسٍ إِلَّا فِي
كِتَابٍ مُّبِينٍ ﴾ .

صدق الله العلي العظيم
سورة الأنعام
الآية (59)

Supervisor’s Certificate

I certify that this thesis entitled “Preparation and studying the structural and optical properties TeO_2/CdO/G Nanocomposite prepared by Laser Ablation” was prepared by student (Ghusoon Saeed Jaber) under my supervision in the Department of Laser physics, College of Science for Women, University of Babylon, as a partial fulfillment of requirement of the degree of Master in Laser Physics.

Signature	Signature
Dr Kaisér Néama Madlum	***Dr. Mohammed Hamza AL- Mamoori***
Title: Professor Dr.	Title: Assistant Professor
Supervisor	Supervisor
Date:	Date:

Head of Department Certificate

In view of the available recommendation, I forward this dissertation for debate by the examining committee.

Signature:

Name: ***Dr. Jinan Ali Abd***

Title: Assistant Professor

Date:

(Head of Laser Physics Department)

Dedications

This thesis is dedicated to my husband ,Who has been a constant source of support and encouragement during the challenges of study and life . I am truly thankful for having you in my life . This work is also dedicated to my parents and children who have always loved me unconditionally and whose good examples have taught me to work hard for the things that I aspire to achieve .

Ghusoon

Acknowledgments

First, I would like to express my deep thanks to the Almighty God, **ALLAH**, for what I have been.

I would like to express my deep gratitude and appreciation to my supervisors ***Dr.Mohammed Hamza AL-Mamoori*** for suggesting the topic of the thesis, continuous advice and their guidance through out thiswork.

I am very grateful to ***Dr. Kaiser N. Madlum*** for submission scientific advice throughout the period of search .

Special thanks are due to the College of Sciences for women and all the staff of the Department of Physics and all for providing the necessary facilities and help especially.

Also, I would like to express my appreciation to the staff of Advanced Nanotechnology laboratory at the University of Babylon –College of Sciences for Women especially ***Rafie Tuama.***

Ghusoon

الخلاصة

في هذه الدراسة، تم تحضير كل من اوكسيد التليريوم، اوكسيد الكادميوم، كرافين نانوشيت، اوكسيد التليريوم/اوكسيد الكادميوم/كرافين نانوشيت (خليط 1) واوكسيد التليريوم/اوكسيد الكادميوم/كرافين نانوشيت (خليط 2) بواسطة التشظية بليزر الندميوم –ياك النبضي مقفل النمط والذي يعمل عند الطول الموجي 1064 نانومتر، والطاقة لكل نبضة 80 ملي جول ،والتردد (معدل تكرار النبضة) 6 هيرتز ، وامد النبضة 10 نانوثانية وعدد النبضات 500 نبضة .

تم دراسة الخواص التركيبية والبصرية لكل المواد المحضرة باستخدام حيود الاشعة السينية، المجهر الالكتروني الماسح، تحويلات فورير للأشعة تحت الحمراء ومطياف الاشعة المرئية وفوق البنفسجية . أظهرت نتائج حيود الاشعة السينية ان كل العينات المحضرة لها تركيب بلوري .ويلاحظ ان حجم الجسيمات النانوية لأوكسيد التليريوم تناقصت بشكل طفيف في الخليط 1 ،بينما الحجم للجسيمات النانوية لأوكسيد الكادميوم ازدادت من 29.1 الى 71.8 نانومتر. بالنسبة للخليط 2 ،لوحظ ان الحجم الجسيمات النانوية لأوكسيد التليريوم تناقص من 73.4 الى 29.7 نانومتر ،بينما حجم الجسيمات النانوية لأوكسيد الكادميوم ازداد بشكل طفيف. وان حجم الجسيمات النانوية لأوكسيد التليريوم واوكسيد الكادميوم في الخليط 1 والخليط 2 كانا متساويين. بصورة عامة ،نلاحظ وجود ازاحة بسيطة في القمم قبل وبعد الخلط، لكن يوجد نمو بلوري واضح لبعض قمم اوكسيد الكادميوم النانوي ،هذا بسبب عملية الترابط بين عنصر التليريوم وعنصر الكادميوم في المركب النانوي خليط 1 و خليط 2 كانت عملية بينية وليست عملية إحلاليه .

من نتائج طوبغرافية السطح للكرافين ، يلاحظ ان الكرافين قد تم تحضيره على شكل صفائح نانوية من الكرافايت. جسيمات اوكسيد التليريوم النانوية تمتلك شكل كروي وبأحجام مختلفة ، ويلاحظ وجود بعض التكتلات في مناطق مختلفة. معدل الحجم لجسيمات اوكسيد التليريوم النانوية كان 65 نانومتر. بعض من جسيمات اوكسيد الكادميوم النانوية تمتلك اشكال غير منتظمة و البعض الاخر كروي الشكل. معدل الحجم لجسيمات اوكسيد الكادميوم النانوية كان 98.4 نلنومتر.

اظهرت نتائج طوبغرافية السطح للخليط 1 تكون جسيمات باحجام مختلفة ،البعض منها كروي، بسبب تكون جسيمات اوكسيد التليريوم واوكسيد الكادميوم النانوية على ارضية شيتات الكرافين النانوية ، والتي تودي الى تكون المركب النانوي اوكسيد التليريوم /اوكسيد الكادميوم /شيتات الكرافين النانوية (خليط 1) وبمعدل حجم 98.9 نانومتر. كذلك اظهرت نتائج طوبغرافية السطح للخليط 2

تكون جسيمات مكعبة وبأحجام مختلفة نتيجة تكون جسيمات اوكسيد الكادميوم واوكسيد التليريوم النانوية على ارضية شيتات الكرافين النانوية ،والتي تودي الى تكون المركب النانوي اوكسيد التليريوم/اوكسيد الكادميوم/شيتات الكرافين النانوية (خليط 2) وبمعدل حجم حبيبي 63.5 نانومتر .

اظهرت تحويلات فورير للأشعة تحت الحمراء قمة عند 1632.6 سم $^{-1}$ والتي تشير الى اصرة تذبذب المط للاصرة C=C(تذبذب اواصر الكابون غير الموكسدة). لوحظت قمم تذبذب المط للآصرة C=O (الكوكسي) عند 1044.4سم $^{-1}$. نطاق الامتصاص عند 561.5 سم$^{-1}$ تعود الى تذبذب اصرة المط للتليريوم-اوكسجين . تذبذب اصرة المط للكادميوم –اوكسجين تقابل قمة امتصاص عند 564.2 سم $^{-1}$. وجود قمة الامتصاص هذه تشير الى نجاح تحضير جسيمات الكادميوم النانوية. نطاقا الامتصاص للمركب النانوي أوكسيد التليريوم /اوكسيدالكادميوم/شيتات الكرافين النانوية (خليط 1) و المركب النانوي اوكسيدالتليريوم /اوكسيدالكادميوم/شيتات الكرافين النانوية(خليط 2)على التوالي عند 580.5 سم $^{-1}$ و 588.2 سم $^{-1}$ ،هي بسبب ترابط جسيمات الكادميوم مع جسيمات التليريوم على صفائح الكرافين

اظهرت قياسات مطيافية الاشعة المرئية وفوق البنفسجية ان وجود قمة امتصاص عند الطول الموجي 265 نانومتر تعود الى الانتقال الإلكتروني $\pi \rightarrow \pi^*$. هذا الانتقال يشير الى وجود اصرة كاربون-كاربون في العالق النانوي. قمة الامتصاص عند 292 نانومتر ترتبط بتكوين جسيمات التليريوم النانوية .قمة الامتصاص هذه تنتج من الانتقال من حزمة التكافؤ (تآصر –بي الثلاثي) الى حزمة التوصيل (اللاتآصر-بي الثلاثي) خلال عملية تأكسد التليريوم الى اوكسيد التليريوم في الماء .ويلاحظ حدوث ازاحة زرقاء بالمقارنة مع مادة التليريوم الاساس (فجوة الطاقة 0.35 الكترون فولت) بسب حدوث ظاهرة الحصر الكمي الناتجة من تأثير الليزر النبضي. من الممكن ان تعرض جسيمات اوكسيد الكادميوم النانوية امتصاص في المدى 250-500 نانومتر .ان البداية الامتصاص عند 285 نانومتر تشير الى تكون جسيمات اوكسيد الكادميوم النانوية .مطياف الاشعة المرئية وفوق البنفسجية بين ان جسيمات اوكسيد الكادميوم النانوية تمتلك ازاحة زرقاء بالمقارنة مع عنصر الكادميوم الاساس بسبب حدوث ظاهرة الحصر الكمي الناتجة من تأثير الليزر النبضي .توجد قمم امتصاص حديدة عند 274.5 نانومتر و 277.3 نانومتر لكل من الخليط 1 والخليط 2 على التوالي . قمم الامتصاص الجديدة تمتلك ازاحة حمراء بالمقارنة مع صفائح الكرافين النانوية و جسيمات اوكسيد الكادميوم النانوية وتمتلك ازاحة زرقاء بالمقارنة مع جسيمات اوكسيد التليريوم النانوية بسبب ظاهرة الحصر الكمي الناتجة من الليزر النبضي. هذه القمم الجديدة تشير الى تكون المركب النانوي اوكسيد التليريوم/اوكسيد

الكادميوم /صفائح الكرافين النانوية (خليط 1) و اوكسيد التليريوم/اوكسيد الكادميوم /صفائح الكرافين النانوية (خليط 2)على التوالي .وجد ان فجوات الطاقة لكل العينات المحضرة تزداد بسبب صغر حجم الجسيمات النانوية بالمقارنة مع المواد الاساسية بسبب حصول ظاهرة الحصر الكمي.

فيما يتعلق بالتطبيق البيئي (ازالة صبغة المثيل الزرقاء)، يلاحظ انه عندما يكون الزمن اطول نحصل على شدة امتصاصية اعلى .هذه النتيجة تشير الى انه من غير الممكن استخدام جسيمات اوكسيد التليريوم ،جسيمات اوكسيد الكادميوم، والخليط 1 والخليط 2 في ازالة صبغة المثيل بلو ،لكن من الممكن استخدامها في تصنيع الخلية الشمسية لأنها تعزز الامتصاصية في المدى المرئي بينما صفائح الكرافين النانوية المحضرة باستخدام الليزر النبضي تمتلك كفاءة عالية في امتزاز صبغة المثيل الزرقاء بالمقارنة مع بقية المواد النانوية المحضرة .قيمة كفاءة الامتزاز تصل الى 65.3 % و 68.7 % عند الزمن 5 دقيقة و 15 دقيقة على التوالي .

اظهر اختبار السمية الخلوية باستخدام خطوط خلايا طبيعية وأخرى سرطانية ان التليريوم النانوي لديه تأثيرات سمية شديدة ضد الخلايا الطبيعية والسرطانية مقارنة بمجموعة السيطرة. بينما اظهر الكادميوم سمية اقل ضد كلا النوعين. لم تظهر الأنواع الأخرى من المركبات النانوية أي تأثيرات سمية لكلا النوعين من الخلايا عند نفس التراكيز المستخدمة مما يشير الى ان بعض المواد المحضرة ذات سمية خلوية للخلايا البشرية.

اظهرت اختبارات الفعالية المضادة للبكتيريا باستخدام تقنية الانتشار من الحفر وجود فعالية انتقائية ضد البكتيريا للجسيمات النانوية. اظهر كل من صفائح الكرافين النانوية والخليط 1 تأثيرا على S. aureus, . بينما جسيمات التليريوم والخليط 1 اظهرت تأثيرا على بكتريا E.coli. اظهرت بكتيريا *P.aerugenosa* و*E.faecalis* مقاومة لكل انواع الجسيمات النانوية المختبرة. هذا يشير الى ان تأثير الجسيمات النانوية يمكن ان يستخدم في معالجة بعض الامراض البكتيرية .

جمهورية العراق

وزارة التعليم العالي والبحث العلمي

جامعة بابل

كلية العلوم للبنات /قسم فيزياء الليزر

تحضير ودراسة الخواص التركيبية والبصرية للمركب النانوي كادميوم\تيليريوم\الكرافين المحضر بالليزر النبضي

رسالة مقدمة الى

مجلس كلية العلوم للبنات- قسم فيزياء الليزر- جامعة بابل

وهي جزء من متطلبات نيل درجة الماجستير في العلوم\فيزياء الليزر

من قبل الطالبة

غصون سعيد جابر

(بكالوريوس فيزياء) (2013)

بإشراف

أ.م.د محمد حمزة المعموري   أ.د قيصر نعمه مظلوم

2022م   1444هـ

1.1 Introduction

Nanoscience is the study of phenomena and the manipulation of materials at the atomic, molecular, and macromolecular sizes, where characteristics (such as optical, mechanical as well as electrical properties) differ greatly from those at larger sizes (bulk). A nanomaterial is defined as " including at least one dimension on the nanoscale scale (approximately 1 to 100 nm)"[1]. Nanoparticles are constituted of several tens or hundreds of atoms or molecules and can have a variety of sizes and morphologies (amorphous, crystalline, spherical, needles, etc.)[2]. The effect of nanotechnology is directly related to the spatial and temporal dimensions under consideration: nanometer-scale materials and devices indicate precise manipulation of individual constituent molecules and atoms in how they are arranged to make the bulk macroscopic substrate. As a result of the control over their molecular production and assembly, nano-engineered substrates may be made to display extremely particular and regulated bulk chemical and physical characteristics. It should be noted that nanotechnology is not a single emerging scientific discipline in it self, but rather the convergence of traditional sciences such as chemistry, physics, materials science, and biology to bring together the necessary collective expertise to develop these novel technologies[3]. Scientists have discovered numerous ways for producing and analyzing several material properties during the last decade, including nanoparticles (NPs) and nanotubes [4, 5], Nanorods[6] Nanowires[7] Nanosheets [8]…..etc, in this study ,optical and structural properties for some of compounds, elements and their mixtures and known applications such biology application's.

1.2 Fabrication of Nanomaterials

There are two ways for nanomaterial fabrication: top-down and bottom-up [9]. The top-down method involves slicing or successively cutting a bulk substance to obtain nanosized particles. Bottom-up approaches relate to the construction of material from the ground up atom by atom, molecule by molecule, or cluster by cluster. Milling, for example, is a typical top-down method for creating nanoparticles, whereas colloidal dispersion is an excellent example of a bottom-up strategy in nanoparticle synthesis. Both techniques are extremely important in nanotechnology, as seen in Figure(1-1) [10] .

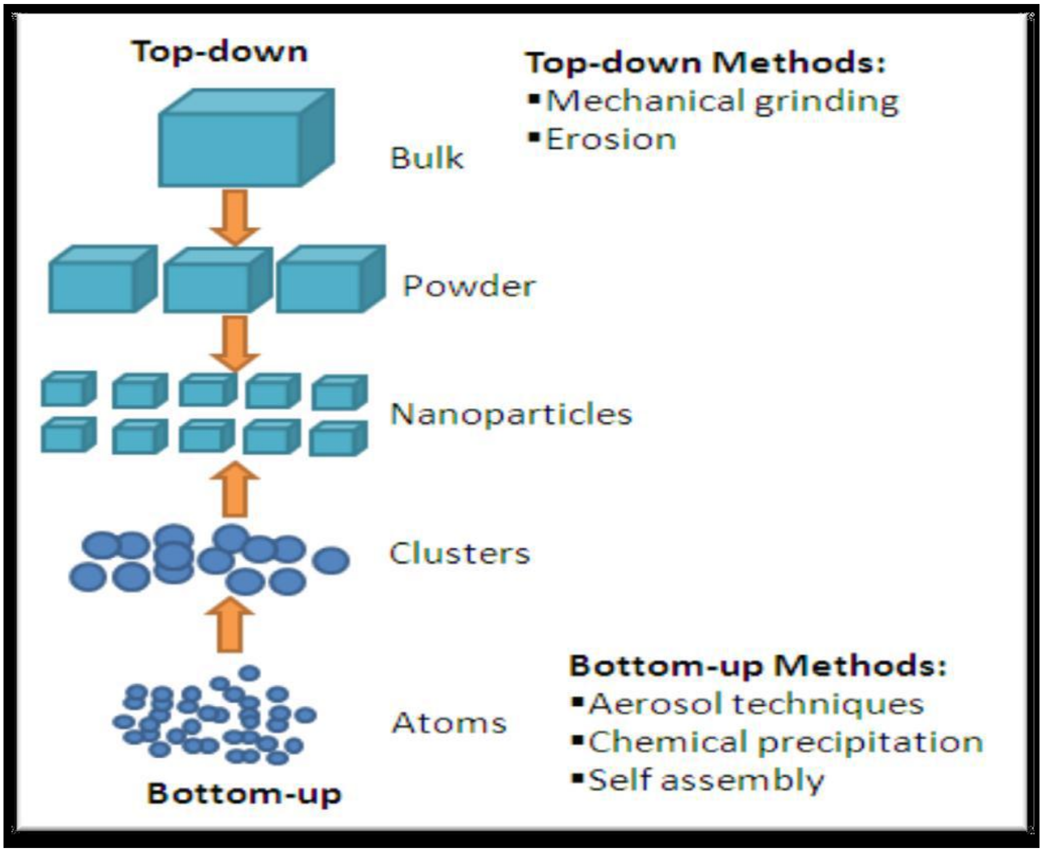

Figure (1-1): Top-down and Bottom-up fabrication are illustrated [10].

1.3 Classification of Nanostructure According to Dimensionality

There are three classes in the nanostructure:

1.3.1 One-dimension confinement (Quantum Well)

The resultant nanostructure is known as a quantum well when only one dimension is reduced to the nanometer range while the other two dimensions remain large [9] . The schematic representation and density of states versus the energy diagram of a quantum well are shown in Figure (1-2).

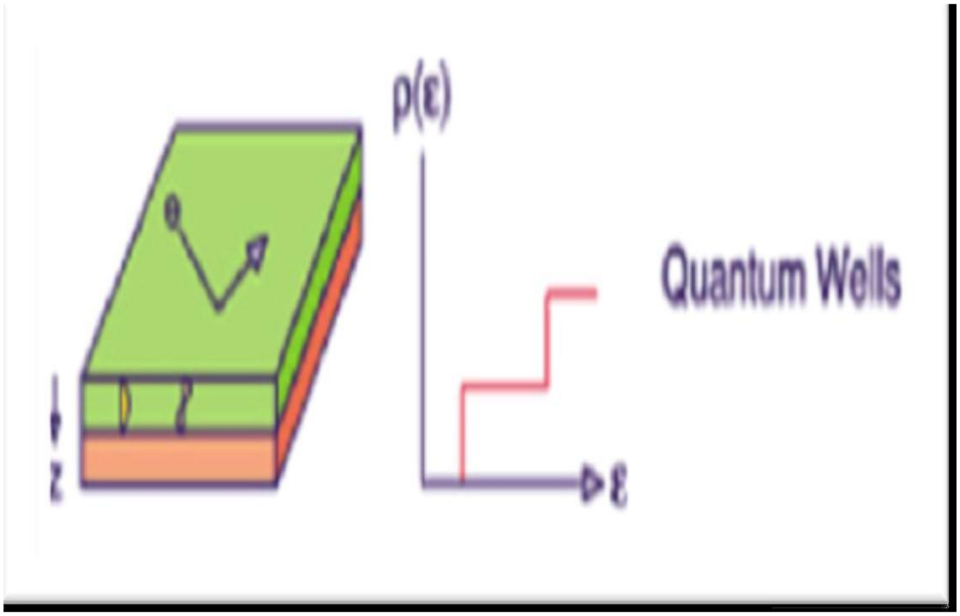

Figure (1-2): Variation of state density with a quantum well's energy diagram [9].

The energy levels that electrons and holes can take are discontinuous yet distinct. In the 2D plane of the QW, electrons and holes are free to move [9].

1.3.2 Two-Dimension Confinement (Quantum Wire)

One-dimensional materials have two confined directions and one unconfined direction. This permits electrons and holes to travel freely along the unconfined direction. As a result, it has distinct optical and electrical characteristics when compared to other dimensional nanomaterials. Because of their original and distinctive features and a vast variety of uses, one-dimensional (1D) nanomaterials such as nanowires, nanotubes, nanorods, nanofibers, and nanobelts have gotten a lot of interest [11] , as shown in Figure (1-3).

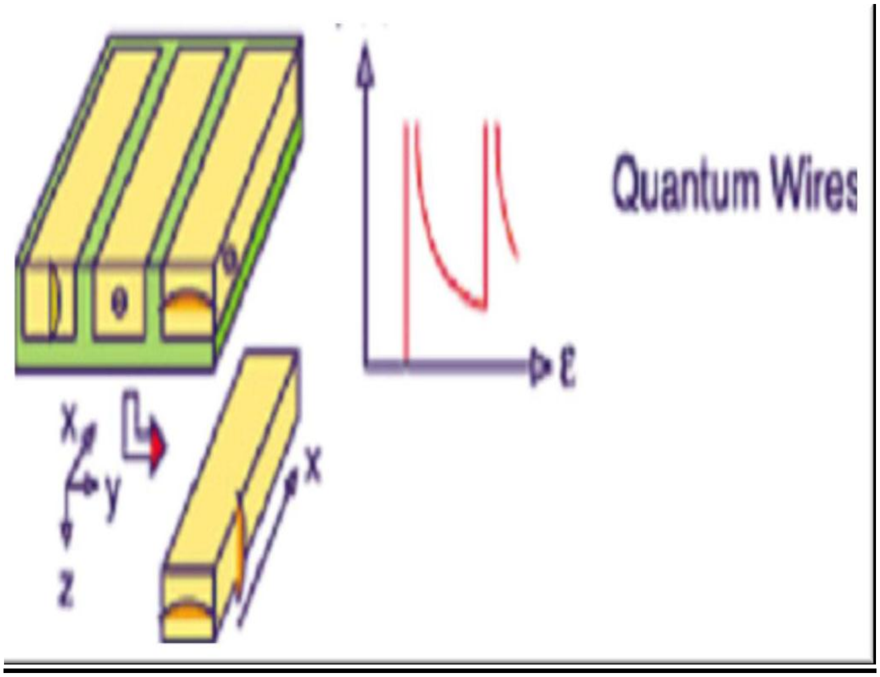

Figure (1-3): Variation of state density with a quantum wire's energy diagram [9].

1.3.3 Three-Dimension Confinement (Quantum Dot)

The carriers in this system are confined in all directions by a quantum box or a quantum dot [9]. Semiconducting quantum dots with nanometer particle sizes have quite interesting properties. The transport of electrons and holes is spatially limited to the Q.D dimension, causing a rise in excitonic transition energy and the observable blue shift in the Q.D band-gap and luminescence. The exciton Bohr radius is a critical parameter, and the confinement effect becomes significant as the Q.D radius decreases [12]. Because electrons in quantum dots possess distinct energy levels, similar to atoms, confinement has a significant impact on the energy spectrum of carriers [13], as shown in Figure (1-4) [9].

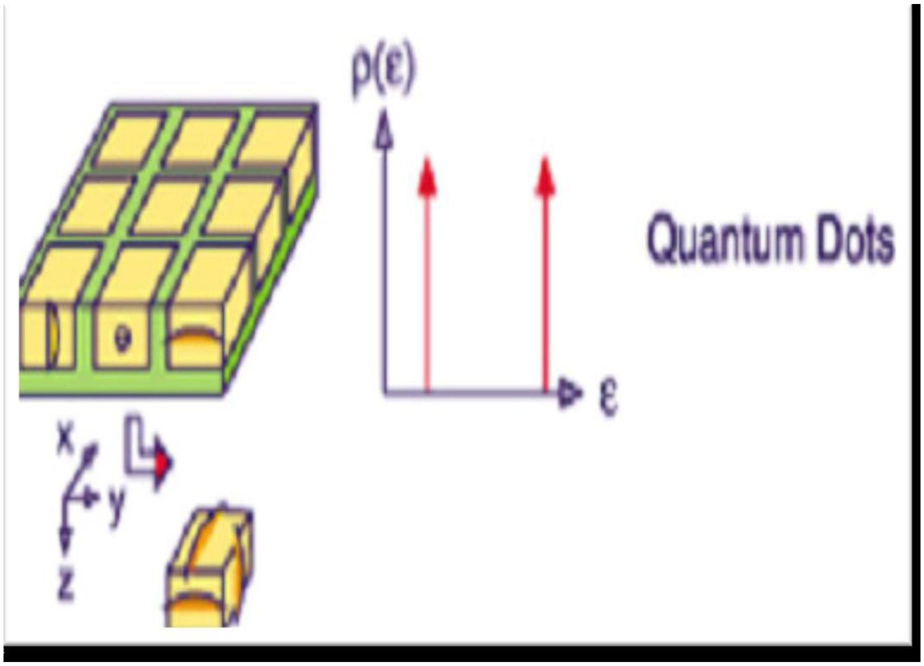

Figure (1-4): A quantum Dot's density of states varies with its energy diagram [9].

1.4 Methods of Preparing the Nanomaterials

For the synthesis of nanomaterials, a number of procedures have been used, depending on the material of interest and the size range involved. A variety of metals, metal oxides, sulfides, polymers, and composite nanomaterials may be created utilizing a variety of synthetic procedures, which are essentially divided into two categories: physical and chemical approaches. The most frequent method for producing nanoparticles is [11].

1.4.1 Sputtering Method

Because of its low cost, simplicity, and low operating temperature, magnetron sputtering is a preferred method [9]. Magnetron sputtering is a type of Physical Vapour Deposition (PVD) process in which films are formed from single atoms or very tiny clusters and any reactions that occur at the film surface (such as oxidation or nitridization). The energetic particle bombards a target surface with enough energy to eject one or more atoms. Inert gas ions (e.g., Ar+, Kr+, Xe+) are the most widely utilized incident species[14].

1.4.2 Electro-Deposition Method

Electro deposition is a simple method for producing high-quality films at low temperatures and costs. An electrical field moves ions through a solution to cover an electrode in an electrodeposition procedure. The most basic electrochemical cell uses a two-electrode arrangement consisting of a cathode and an anode. The voltage is measured between these two electrodes in the 2-electrode system, while the current is measured everywhere in the circuit. Under equilibrium conditions, this device works excellently[15].

1.4.3 Spray Pyrolysis Method

Spray pyrolysis has been used to deposit a broad range of thin films. These films have been employed in a variety of technologies, including solar cells, sensors, and solid oxide fuel cells. The characteristics of the deposited thin films are heavily influenced by the preparation conditions. Spray pyrolysis involves spraying preheated substrates with a solution containing soluble salts of the target product. The most crucial parameter is the substrate surface temperature, which effects film thickness, cracking, crystallinity, etc [16]. Spray pyrolysis deposition is a low-cost, up-scale technology for producing thin polycrystalline films over large surface areas. [17]. The important parameters can be changed in this technique substrate type, growth temperature, spray rate and solvent type[18].

1.4.4 Sol-Gel Method

The sol-gel method includes transforming a system from a liquid "sol" (usually colloidal) phase to a solid "gel" phase [19]. One of the most often used solutions processing methods for manufacturing metal oxide nanoparticles is the sol-gel approach. A reactive metal precursor, such as metal alkoxide, is hydrolyzed with water in sol-gel processing, and the hydrolyzed species are allowed to condense with one other to generate precipitates of metal oxide nanoparticles. The precipitate is then cleaned and dried before being calcined at high temperatures to produce crystalline metal oxide nanoparticles[20]. Sol-gel technique may also be used to produce nano powders, fibers, solid structures, and thin film coatings with great efficiency and purity. Another advantage of sol-gel is the development of a homogenous substance[21].

1.4.5 Spin Coating

In this process, solutions are deposited on a substrate that is spun at high speeds, causing the solution to spread, resulting in a homogenous thin layer with great repeatability. Spinning parameters such as spin speed, duration, and temperature impact film formation, as do solution properties such as viscosity, volatility, concentration, and molecular weight [22]. Some advantages of this method include the ability to simply change the film thickness by changing the spin speed, as well as its low cost and quick operating system [23]. The Spin coating has four stages: deposition, spin-up, spin-off, and solvent evaporation. The thinnest films with the roughest surfaces are created by the greatest spin rates, while the thickest films with the nicest surfaces are formed by the lowest spin rates[24].

1.4.6 Hydrothermal Technique and Reaction Autoclaves

Hydrothermal synthesis is a subset of solvothermal synthesis in which solvents rather than water are utilized. The phrase hydrothermal derives entirely from geology. Sir Roderick Murchison (1792-1871), a British geologist, used the term to describe the impact of water at high temperatures and pressure on the earth's crust, resulting in the production of diverse rocks and minerals. Hydrothermal processing is any heterogeneous reaction that takes place under high pressure and temperature settings in the presence of aqueous solvents or mineralizers to dissolve and recrystallize (recover) materials that are relatively insoluble under ordinary situations [25].

1.4.7 Pulsed Laser Ablation in Liquids(PLAL)

When the laser beam falls on the surface of the metal immersed in the liquid, it will reflect part of the surface of the metal immersed in the liquid.The falling button beam and the rest are absorbed by the surface of the metal and liquid. This leads to an increase the heat energy and the melting and evaporation of the surface of the metal This leads to a higher degree of Heat, pressure, and limitations to the formation of a dense plasma (Plasma Plume)[26]. According to the study conducted by yang[27]. It will extract multiple types of different ions and atoms from the surface of the metal immersed in the liquid during the removal process. These types have large kinetic energy when the beam of the laser is used in high-capacity ablation. In addition, these types of different ions and atoms that were extracted as a result of the laser ablation process have a high density of gases, solids and liquids, which are among the basic components of plasma (Plasma Plume).

As a result of various laser beam pulses on the surface of the metal contained in the liquid, this created plasma expands, resulting in extra pressure inside the plasma. This high pressure produces a rise in temperature, which causes more liquid to vaporize and bubbles to develop, and by intensifying the evaporation process. These bubbles will tend to grow further until they explode inside the liquid at a specific critical pressure and temperature. It is believed that the formation of nanoparticles of the dissolved metal inside the liquid is due to the high temperatures and extreme pressure resulting from the collapse of the plasma[27].

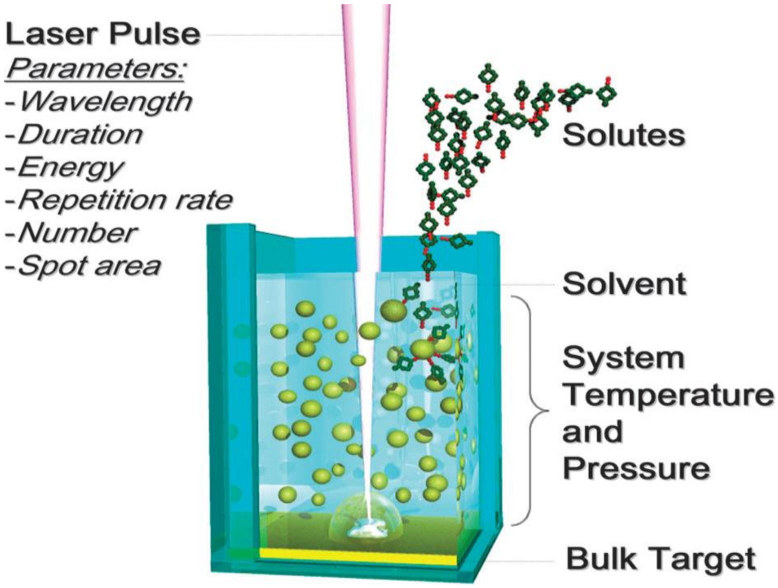

Figure(1-5) Representing a schematic diagram of the laser ablation method in fluids

Figure (1-5) shows the PLAL process[28]. The result of the chemical interactions that occur between the molecules of the solid and the dissolved materials in the liquid is nanoparticles (NPs), which are made up of atoms from the target and the liquid that collide in the liquid[29]. There are several factors that affect the laser ablation process, including: the laser wavelength, the laser energy, the type of liquid medium, the depth of the optical path of the laser beam inside the liquid, and the type of target material. PLAL is a more effective technique, as the aggregation of nanoparticles can be avoided by using dispersants and ultrasonic vibration in addition to changing the pH of the solution[30]. The liquid-phase pulsed laser ablation process offers several advantages, including the following: the chemical composition is simple and clean, and the end product is produced fast and without the need for extra purification, low cost and easy control of parameters. In addition, it is characterized by preparing nanomaterials at low temperatures, producing more than one material at the same time, and homogeneous and pure compounds[31]. The first process of laser ablation is the interaction of a laser beam with the surface of a hard target that causes the steel target to evaporate and vapourize into a liquid created by a colloid solution. Chemical interactions may occur between solids and solids in liquid, and the result of these interactions is generally nanoparticles (NPs) composed of atoms from both the target and the liquid that collide when floating in the liquid[32]. The optical absorption spectra of metal nanoparticles are well known to be dominated by surface-plasmon resonance (SPR)[33], and shift to longer wavelengths as particle size increases. The plasmon resonances of noble metal nanoparticles are visible. The collective vibration of electrons causes this plasmon resonance[34], which is sensitive to size, shape and the surrounding medium[35]. The plasmon resonance enables the monitoring of size and shape transitions using just the UV/V is absorbance.

1.5 Properties of Nanomaterials

1.5.1 Mechanical Properties

Mechanical properties are the mechanical properties of components in different situations and under diverse external stresses. Mechanical qualities vary depending on the substance. Metals' mechanical properties normally consist of 10 parts, which include brittleness, strength, plasticity, and hardness. Hardness, toughness, fatigue strength, elasticity, ductility, stiffness, and yield stress are all important properties to consider. Most inorganic non-metallic materials are brittle and lack characteristics including plasticity, toughness, elasticity, and ductility. Moreover, many organic materials are flexible, having characteristics such as brittleness and hardness[36].

1.5.2 Optical properties

Surface dimers have a strong influence on the optical characteristics of extremely small nanoparticles (less than 1 nm), and surface steps are responsible for the biggest optical gap decreases in most nanoparticles. These predictions prove true for a wide range of semiconductor nanostructures with highly curved surfaces, including quantum dots and wires, NEMS devices, and nanocantilevers [33].

1.5.3 Electrical properties

Because of their large grain boundary (surface) area, nanomaterials can carry far more energy than typical coarse-grained materials. They are materials in which an optical absorption band may be introduced or an existing band can be changed by passing a current through them or applying an electric field. Many applications that require electrical energy use both standard and rechargeable batteries. The energy density (storage capacity) of these batteries is often extremely low, necessitating regular recharging. Nanocrystalline materials are excellent options for separator plates in batteries because they can store far more energy than traditional materials. Nickel-metal hydride batteries constructed of nanocrystalline nickel and metal hydrides are expected to require significantly less frequent recharging and to last much longer [37].

1.5.4 Thermal properties

In general, increasing the number of grain boundaries increases phonon scattering at disordered borders, which results in reduced thermal conductivity. As a result, nanocrystalline materials are projected to have poorer heat conductivity than traditional materials. However, when grain sizes approach the nanoscale, they become similar to the mean free pathways of phonons that transfer thermal energy. Because of the photon confinement and quantization effects of photon transport, nanomaterials can have very different characteristics than course yes materials. It has been discovered that, in addition to particle size, the form of nanomaterials influences their thermal characteristics [37].

1.6 Characteristics of The Laser Beam

The laser beam has four main characterized by[38]:

1-Monochromatic: Monochromatic refers to a single wavelength, or "one color" of light. Laser radiation contains a narrow band of wavelengths and can be produced closer to monochromatic than light from other sources.

2- High Directionality: The radiation is produced in a beam that is spatially narrow and has low divergent angel relative to other light sources.

3-coherency: It means that the difference between any two points on the wave of the laser beam is constant when it moves in time and space. The laser is the only light source that has the characteristic of coherence compared to other traditional light sources

4-Brightness: It is the amount of energy emitted per unit time, unit area of the surface, and unit solid angle unit [39].

1.7 Nd-YAG Laser

The Nd-YAG laser is one of the most important solid-state lasers discovered in 1964. The active medium has a crystal of (YAG), which is (yttrium–Aluminum-Garnet) doped with neodymium ions (Nd^{+2}). The inoculation ratio does not exceed (1.5%), and the color of the crystal is purple. The YAG crystal is characterized by high resistance to damage, hardness against breakage, and high optical quality. The Nd –YAG laser operates in a four-level system with a continuous pulse mode, and the effective medium is pumped using a flash lamp. As an electric voltage is shed between the two ends of the lamp, producing light rays that are absorbed by the crystal to irradiate, or by using a semiconductor laser (diode laser). Nd-YAG laser emits a beam of wavelength (1064 nm) in the infrared region[40]. It is possible to obtain wavelengths 532 nm (SHG) and 335(THG) using nonlinear crystals. Figure (1-6) shows a diagram of the energy levels of the Nd-YAG laser [40].

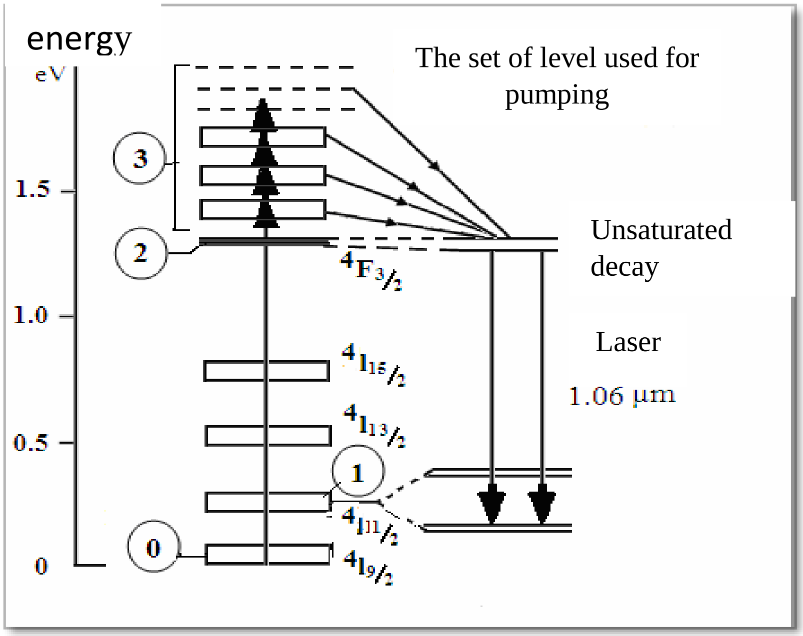

The Figure(1-6) The main regions of a diagram of the energy levels of Nd-YAG Laser [40].

1.8 Semiconductors

Solid materials can be classified according to their ability to conduct electricity into conductive materials such as copper metals. This tab came depending on the range of free electrons available in the outer orbit of the atom, which is known as the valence orbit. Therefore, metallic materials are good electrical conductors, as the density of the presence of free electrons is responsible for the conduction increases, while it is low in insulating materials, there are a group of materials called semiconductors, such as silicon and germanium, that are not subject to this classification because they are an exceptional material, where the value of the volumetric density of its free electrons ranges between conductors and insulators. Semiconducting materials have two bands: the valence band, which is packed with electrons, and the conduction band, which is empty of electrons, and between them is a gap called the energy gap can be defined as the energy needed to raise an electron from the valence band to the conduction band. This gap is small compared to insulating materials[41]. Figure (1-7) shows the schematic of the energy bands in the resources [42].

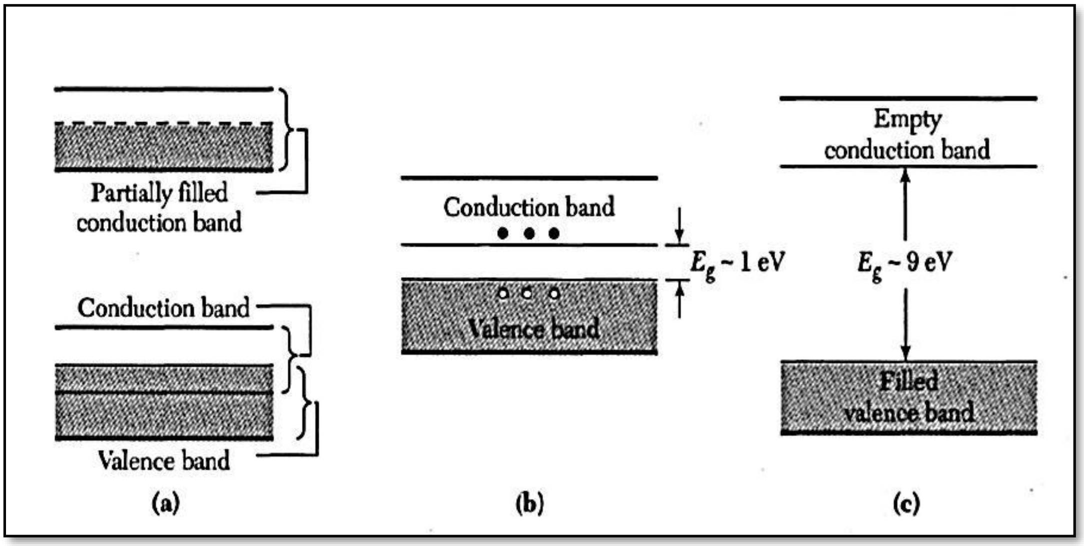

Figure(1-7): The main regions of the energy bands in materials a/ conductive b/ semiconductor c/ dielectric [42].

1.8.1 Classification of Semiconductors

Semiconducting materials are classified according to their crystalline structure into:

a- Crystalline Semiconductors

1-single crystalline semiconductors

These materials are characterized by the fact that their atoms are arranged in all directions and in a regular periodic manner, meaning that it is repeated periodically in the three dimensions and for a long period, and the arrangement of the atoms in this way is called(Long Range Order)[43]. As shown in Figure (1-8 a), where the atoms of the substance are arranged in all directions in a regular manner[44].

2- Polycrystalline Semiconductors

These materials consist of many small crystals called (Grains). Each crystal grain consists of thousands of cell units, where each cell has a(Long-Range Order), while the crystal grains as a whole have a (Short-Range Order), and the areas of the confluence of the grains (at which the periodic order of each grain is cut off) are called the(Gain Boundaries)[45]. as shown in Figure (1-8 b) [44].

b- Amorphous Semiconductors

The structure of these materials is characterized by a regular (Short Range order), where their atoms are arranged in an amorphous shape forming a complex group, and the atoms of these materials cannot periodically rearrange themselves in the three dimensions due to the loss of the periodic arrangement for distances greater than two or three halves atomic diameters[46]. As shown in Figure (1-8 c) [44], all crystalline materials are characterized as having different directional (Anisotropic) characteristics, meaning that the direction of the axes of the crystal has an effect on its distinctive properties. In addition to its sudden melting at a certain temperature , as random materials, they are characterized by being identical in directional properties (Isotropic), and this shows that there is no effect of direction on their properties, in addition to that they melt at a certain range of temperatures[47].

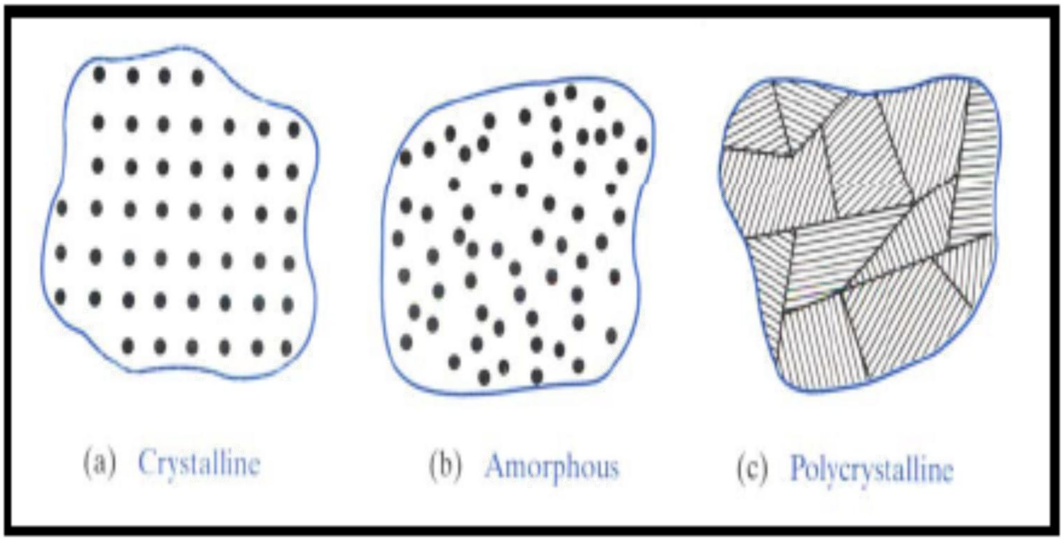

Figure (1-8) : Different types of semiconductors a-crystalline b- Amorphous c- Polycrystalline[44].

1.9 Optical Properties

Studying the optical properties of semiconductors is an important way to understand the mechanism of electronic transitions between energy bands, by measuring the radiation absorption and transmittance of the semiconductor material. The characteristic and common characteristic of all semiconductors is the rapid increase in absorption when the energy of the absorbed radiation is approximately equal to the forbidden energy gap, called (Fundamental Absorption Edge)[48]. The absorption region of a semiconductor can be divided into three basic regions, as shown in Figure(1-9) [49], which are:

1-High Absorption Region (A)

The amount of absorption coefficient in this region is ($\alpha \geq 10^4 cm^{-1}$) .This region is produced due to the transitions that occur between the (extended levels) of the valence and conduction bands[50].

2- Exponential Absorption Region (B)

The range of absorption coefficients is ($1<\alpha<10^4$) cm^{-1}. It is the transition area between the extended levels in the valence band and the local levels at the bottom of the conduction band, as well as the transition region between the extended levels in the conduction band and the local levels in the valence band [50].

3-Low Absorption Region (C)

The absorption coefficient in this area is very small($\alpha<1 cm^{-1}$)The amount of absorption coefficient in this region is very small, and it represents the transitions between the energy tails within the optical gap[51].

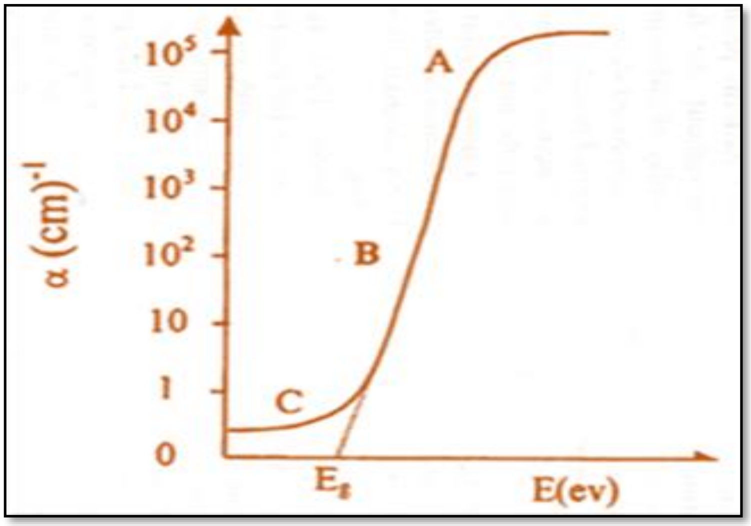

(1-9): The main regions of the main regions of the absorption edge[49].

1.9.1 Transmittance (T)

It is known as the ratio between the intensity of the transmitted light ray(I) to the intensity of the incident light ray(I^o)and it is written in the following form [52].

$$T = \frac{I}{I^0} \quad \dots\dots\dots\dots\dots\dots\dots\dots\dots\dots\dots\dots (1-1)$$

Where I: is the intensity of the light at the wavelength (λ) that passes through the sample (the intensity of the transmitted light) .

I^o: The intensity of the light before entering the sample or the intensity of the incident light .

1.9.2 Absorbance (A)

The absorbance (A) or optical density is the mathematical quantity that connects the particle density (concentration C) in a sample to the sample thickness (optical path lengths X).

$$A = log\frac{I^0}{I} \quad \dots\dots\dots\dots\dots\dots\dots\dots\dots\dots (1-2)$$

The absorption of the incident rays cause an electronic activity that may lead to the breaking up of molecules if the value of the absorbed energy is greater than the value of the dissolution of one of the bonds or its transfer to a higher energy level [53].

1.9.3 Absorbance Coefficient (α)

It is defined as the amount of decrease in the energy of the incident ray relative to the unit length in the direction of wave propagation within the medium, and it is possible to identify the nature of the electronic transitions whether they are direct or indirect through the values of the absorption coefficient(α)[54]. The absorption coefficient can be calculated using the following relationship[55].

$$\alpha = \frac{2.302\ \log(\frac{I^0}{I})}{x} \ldots\ldots\ldots\ldots\ldots\ldots\ldots\ldots..(1-3)$$

Where $\log(\frac{I^0}{I})$ represent the absorbance (A).

If the value of the absorption coefficient (α) is equal to ($\alpha \geq 10^4$ cm^{-1}), the electronic transfers are direct, but if the value of the absorption coefficient is ($\alpha \leq 10^4$ cm^{-1}), the electronic transitions are indirect[56].

1.10 Types of Transitions

There are two types of transitions in semiconductors, which are direct and indirect transitions, depending on the location of the highest point at the top of the valence band, and the lowest point at the bottom of the conduction band.

1.10.1 Direct Transitions

Occurs when the electron moves directly from the top of the valence band (V.B) to the bottom of the conduction band (C.B), and when the locations of the top of the valence band and the bottom of the conduction band are identical″and at the same magnitude of the wave vector i.e. (ΔK = 0) [56]:

$$\alpha h\vartheta = B\ (h\vartheta - Eg)^r \ldots\ldots\ldots\ldots\ldots\ldots\ldots\ldots (1-4)$$

Where:

B: a constant that depends on the nature of the material

Eg: Optical band gap of material

hν: photon energy

r: A constant if takes the value (1/2) in the case of the allowed direct transmission ,and the value (3/2)in the case of the forbidden direct transmission .

1.10.2 Indirect Transitions

These transitions occur when there is a mismatch in the wave vector space(k) between the energies of the valence band top and the bottom of the conduction band, where the transition is from the highest point of the valence band to the lowest point of the conduction band in a non-vertical way which in **($\Delta K \neq 0$).** This transition results in a change in the crystal's momentum. In order to achieve the law of conservation of energy and momentum, this change in momentum is compensated by the lattice either by phonon absorption or its emission. The absorption equation for this type of semiconductor is given by the following relationship[57].

$$\alpha h\vartheta = B\ (h\vartheta - Eg \mp Ep)^{r} \ \ldots\ldots\ldots\ldots\ldots\ldots(1\text{-}5)$$

Where:

B: constant that depends on the nature of the material

E_P: Photon energy represent the sign (+)phonon emission , and sign(-) absorption phonon, r: constant and take the value(2) in the case of indirect allowed transmission ,and the value (3)in the case of indirect forbidden transmission .

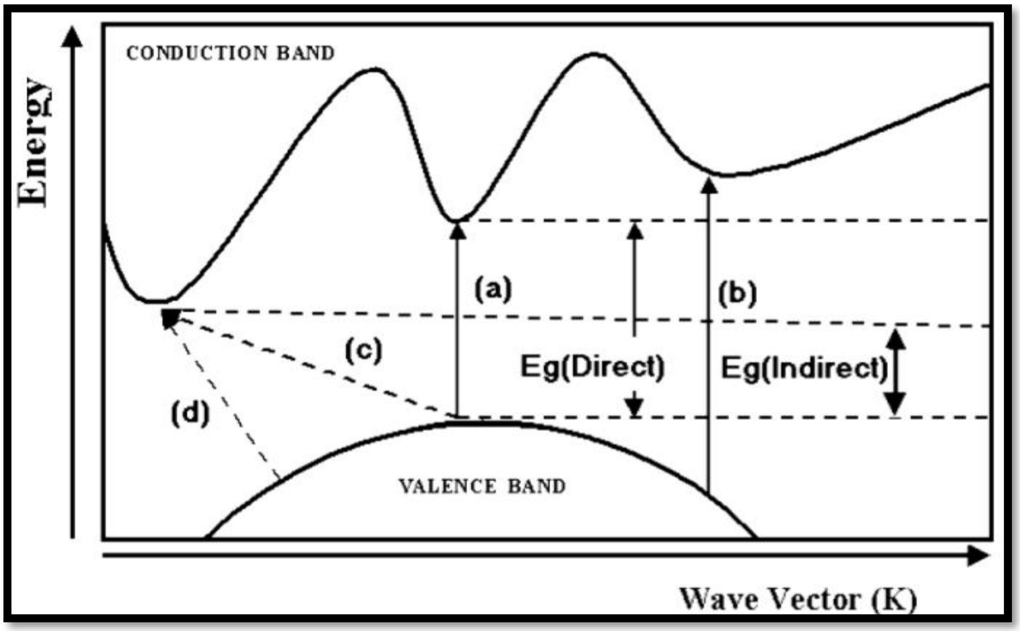

Figure(1-10): The main regions of the types of electronic transmissions (a) direct transmission allowed. (b) Direct transmission is forbidden. (c) Indirect transmission is permitted. (d) forbidden indirect transmission [58].

1.11 Nano Materials

Carbon is the one, which still gets a lot of attention, carbon is a ubiquitous molecule capable of forming many allotropes with many potential applications. The major ones are graphite and diamond[59]. Nanocarbons belongs to carbon all carbon nanotubes and two-dimensional (2D) graphene. Nanocarbons have lately received increased interest because of their unusual electrical, optical, thermal, and chemical characteristics, which promise applications in a range of areas [60].

1.11.1 Graphite and Graphene

Graphite is a carbon allotrope. Natural graphite is classified into three types: flake graphite, vein graphite, and microcrystalline graphite. The most frequent kind of graphite utilized in chemical reactions is flake graphite. Because of its great crystallinity, the vein graphite structure is electrically conductive. Amorphous graphite is another name for microcrystalline graphite. Graphite is a low density, low-cost material, and microcrystalline graphite has long been employed in pencil manufacture. Graphite is a material with high electrical and thermal conductivity [61]. Graphite's conductivity is determined by its structure. Polycrystalline graphite, on the other hand, has a vastly higher resistivity due to the crystal boundaries. Graphite has a multi-layer structure with hexagonal lattice arrays in each layer. This meansn that graphite is formed of parallel layers of graphene with hexagonal rings[62], as shown in Figure (1-11) [63]. Each yellow sphere represents a carbon atom, and each blue line represents a covalent link between carbon atoms. The dotted line depicts the weak Vander Waals forces that allow sliding movement between the parallel hexagonal rings.

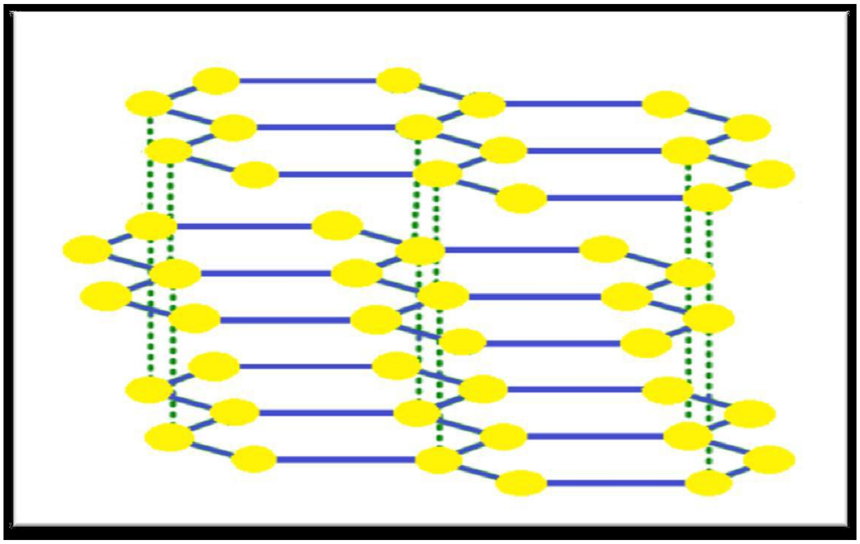

Figure (1-11): Structure of graphite [65].

Graphene, a two-dimensional (honey comb lattice),a single-layered sheet of sp2 hybridized carbon atoms, has caught the interest of researchers because of its intriguing mechanical, thermal, electrochemical, and electrical characteristics. These outstanding qualities have created new prospects for the use of this nanomaterial in future devices and systems [64], as shown in Figure (1-12).

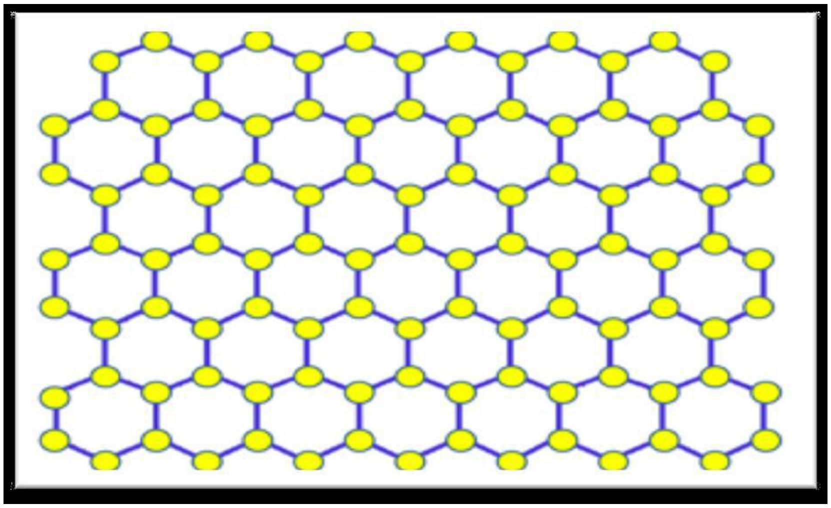

Figure (1-12): Graphene structure [66].

Graphene may be made by micro-mechanical exfoliation of highly ordered pyrolytic graphite, epitaxial growth, chemical vapor deposition, and graphene oxide reduction (GO)[65]. Graphene nanoparticles can be used in a variety of biological applications. The possibility of graphene as nanocarriers for medication delivery, gene delivery, and nanomedicine for future anticancer therapy has been shown [66]. Graphene materials have the potential to be utilized in improved energy-conversion devices such as solar cells and fuel cells, as well as energy-storage devices such as supercapacitors and lithium-ion batteries [67].

1.11.2 Graphene Oxide (GO)

Graphene oxide has a layered structure comparable to graphite, but the plane of carbon atoms in graphene oxide is highly adorned by oxygen-containing groups (epoxy hydroxyl and carboxyl groups), which not only increase the interlayer distance but also make the atomic-thick layers hydrophilic[68]. GO is of tremendous interest owing to its inexpensive cost, ease of access, and wide ability to convert to graphene. GO is frequently regarded as an electrical insulator. The capacity of GO to conduct electrons is determined by the quantity of oxidization in the molecule as well as the technique of production[69]. It contains a mixture of sp^2 and sp^3 hybridized carbon atoms. In contrast to pure graphene, GO is fluorescent over a broad range of wavelengths [70], as shown in Figure (1-13)[71].

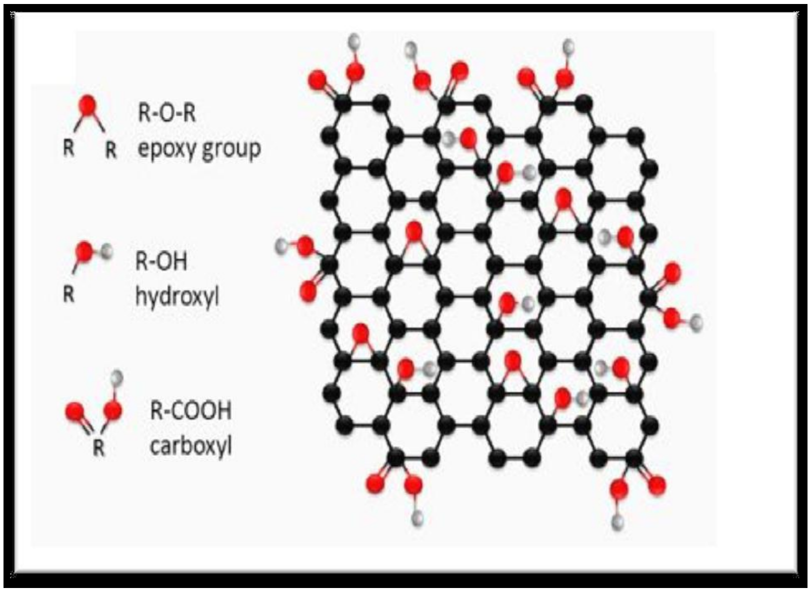

Figure (1-13): Graphene oxide structure [71].

GO could act as a photocatalyst in the water splitting process [72]. Graphene compounds' unique and interesting features, including, high UV absorption, fluorescence, and fluorescence quenching capabilities, make them one of the most promising materials for biosensors, therapies, tissue engineering, and electronics[73].

1.12 Method of preparation of Graphene Oxide

There are numerous methods for producing graphene oxide (GO), and they are as follows: [74].

1.12.1 Hummer's Method

It is one of the chemical ways for producing graphene oxide, and it is achieved by adding potassium permanganate $KMnO_4$ to a combination of graphite, sodium nitrate $NaNO_3$, and sulfuric acid H_2SO_4. This process is widely used for producing large amounts of graphene oxide (GO)[75].

1.12.2 Modified Hummer's Method

This technique is widely used to create significant amounts of graphene oxide. This technique combines (1gm) of pure and fine graphite powder, (1gm) of sodium nitrate, and (6gm) of potassium permanganate $KMnO_4$ with (46ml) of concentrated sulfuric acid (H_2SO_4) in an ice bath for two hours and after adding the ice bath was raised, then stirred the mixture using a magnetic stirrer and for three days at laboratory temperature, it was observed that the color of the mixture changed from green to brown. Later, (60ml) of hydrogen peroxide (H_2O_2) and (200ml) of distilled water was slowly added, where it was observed that the color of the mixture changed from brown to yellow, and which indicates the formation of graphene oxide. Then, the graphene oxide is separated using a centrifuge at (6000rpm)[76]. Then it is washed and purified using hydrochloric acid (HCL) and distilled water.

1.12.3 Staudenmairs Method

It is one of the appropriate chemical methods for producing graphene oxide (GO) by changing the ratio of HNO_3/H_2SO_4. In this method, Graphite is oxidized in this process with a 1:3 combination of sulfuric H_2SO_4 and nitric acid HNO_3. The results reveal that the graphene oxidation process [77].

1.13 Reduced Graphene Oxide (rGO)

There are numerous methods for producing reduced graphene oxide (rGO), and they are as follows:

1.13.1 Thermal Reduction

The thermal graphene oxide reduction method involves removing oxygen from graphene oxide and converting it to reduced graphene oxide, using high temperatures up to(2000°C)[78]. The thermal reduction product has a large surface area[79]. In addition, the resulting materials are of high efficiency because they are pure and free of impurities.

1.13.2 Chemical Reduction

Chemical reduction occurs through the use of chemical detectors in a chemical reaction with graphene oxide, It is a cheap and simple method for producing reduced graphene, and it relies on strong reducing chemicals like hydrazine, which is a suitable chemical detector for reducing graphene oxide. and ammonia, as well as eco-friendly natural products, can be employed to decrease graphene oxide[80, 81].

1.13.3 Electrochemical Reduction

The electrochemical reduction of graphene oxide takes place in a normal electrochemical cell using a dielectric aqueous solution at room temperature. Where it is dependent on the electrochemical removal of functional groups of oxygen, and the reduction process occurs through the exchange of electrons between GO and electrodes. In this way, the reduction process with chemical reagents such as hydrazine can be dispensed with, because the chemical reagent results in residues that cause pollution to the resulting substance[82].

1.14 General Properties of Cadmium and Cadmium Oxide

Symbol Cd, atomic weight 112.4, a metallic element, show a close relationship to zinc, with which it is very frequently associated. Cadmium is a non-essential element that is harmful to a wide range of plants and animals. The metal, discovered in 1817, is derived primarily as a byproduct from zinc, copper, and lead ores and has significant industrial applications. Cadmium is used in pigments, , batteries, solar cells and solders. It is often used in electroplating[83]. Cadmium Oxide is a highly insoluble thermally stable Cadmium source used in glass, optics, and ceramics. Cadmium oxide is a crystalline solid that occurs naturally as the mineral monteponite and is commercially made by oxidizing cadmium vapor. Cadmium Oxide (CdO) Powder is used in aeronautical and electrochemical applications such as fuel cells because of its ionic conductivity[84].

Table(1-1) Physical and Chemical Properties of Cadmium[85]

Property	**Cadmium**
Atomic number	**48**
Molecular weight	**112.41 mol\gm**
Color	**Silver-white**
Physical state	**Lustrous metal**
Melting point	**321 °C**
Boiling point	**765 °C**
Density at 20 °C	**8.65 g/cm^3 at 25 °C**
Heat of fusion	**6.21 kJ/mol**
Heat of vaporization	**99.6 kJ/mol**

1.15 General Properties of Tellurium and Tellurium Oxide

Tellurium (Te) is well known as a p-type semiconductor with a band- gap of 0.35 eV at room temperature and possesses a wealth of intriguing properties such as photoconductivity, thermoelectricity, and piezoelectricity [86]. Tellurium is a silver-white semimetallic element that is glossy, crystalline, and brittle. It is often available as a dark grey powder with characteristics of both metals and nonmetals. Tellurium may produce several compounds that are similar to sulfur and selenium. Tellurium displays a greenish-blue flame when burned in the air and produces tellurium dioxide out of the atmosphere. Water and hydrochloric acid have little effect on tellurium, but it dissolves in nitric acid [87]. Tellurium Dioxide will continue to be used in specialist applications such as anti-corrosive materials in batteries. It is really heartening to see how science may extend the reach of fiber optics above and beyond any existing restrictions as it produces greater efficiency and breakthroughs. These new developments may raise demand for high purity tellurium dioxide[87]. .

Table (1-2) Physical and Chemical Properties of Tellurium [87].

Property	**Tellurium**
Atomic number	**52**
Atomic mass	**127.6 g.mol $^{-1}$**
Density	**6.24 g.cm^{-3}**
Melting point	**450 °C**
Boiling point	**988 °C**
Heat of fusion	**17.49 kJ/mol**
Heat of vaporization	**114.1 kJ/mol**
Molar heat capacity	**25.73 J/(mol·K)**

1.16 Antibacterial Activities of Nanoparticles

Bacterial infections and the emergence of antibiotic resistance have created significant health problems in recent years. Antibiotic overuse and misuse in previous decades had a significant influence in this catastrophe. The World Health Organization (WHO) projected in 2019 that antimicrobial resistance (AMR) will kill 10 million people each year, with Gram-negative infections accounting for two-thirds of these fatalities. Notably, *Escherichia coli, Klebsiella pneumonia , Pseudomonasaeruginosa, Proteusmirabilis, Serratiamarcescens and Staphylococcus aureus are* species . As a result of their multidrug resistance, they are responsible for the bulk of clinical infections and present a significant danger to human healthcare [88].

The emergence of new resistant bacterial strains necessitated the development of novel bactericidal materials. In this context, the synthesis of chemicals with antimicrobial characteristics, such as nanoparticles, is critical and has potentially beneficial uses in the battle against antibiotic-resistant pathogenic bacteria, which represent a constant danger to human and animal health [89].

Various types of nanomaterials, are either used directly as an antibacterial agents such as metallic nanoparticles (NPs) (silver, gold, zinc, etc.) or as a nanocarriers to deliver and target the antibiotic to the bacteria and its infected area [90].

Some biological activities of nanoparticles have been reported recently, such as the antimicrobial effect of silver nanoparticles, gold nanoparticles, titanium dioxide nanoparticles, zinc oxide nanoparticles and silica nanoparticles[91].

Metal oxide (M-O) nanoparticles, which range in size from 1 to 100 nm and come in a variety of forms and sizes, are one type of nanomaterial. M-O nanoparticles have distinct physical and chemical properties due to their nanoscale size, providing versatility[92].

MeO NPs have the potential to be effective antibacterial agents against a wide range of microorganisms, including drug-resistant species [92].

The antibacterial activity of Cadmium oxide nanoparticles was investigated using the well diffusion method against several pathogenic bacteria, including *Klebsiella pneumoniae, Acinetobacter baumannii, Pseudomonas aeruginosa, and Staphylococcus aureus*, and it was discovered that Cadmium nanoparticles had an inhibitory effect against all pathogenic bacteria [89].

It has been shown that the antibacterial effects of cadmium oxide nanoparticles on positive gram bacteria are greater than those on negative gram bacteria *Staphylococcus aureus* bacteria were more sensitive to nanoparticles as compared to *Pseudomonas aeruginosa* and increase of cadmium oxide concentration. Antimicrobial properties rise while bacterium growth speed decreases, which is consistent with other study on the effect of nano particles on microorganisms [93].

Its research shows that nano CdO can be utilized to treat infectious diseases caused by *E. coli*. Several researchers have proposed a mechanism involving the interaction of nanomaterials with biological macromolecules. Zhang and Chen think that microorganisms have a positive charge. The microorganisms and treated surface form an "electromagnetic" attraction as a result. Once in touch, the microbe is oxidized and dies instantaneously. Russell and Hugo discovered that strong nanoparticle attachment to the outer membrane of E.coli inhibits active transport, dehydrogenase, and periplasmic enzyme activity, and eventually inhibits RNA, DNA, and protein synthesis, leading to cell lysis. Nanomaterials are thought to emit ions that react with the thiol groups (-SH) of proteins on the bacterial cell surface. These proteins protrude through the bacterial cell membrane, allowing nutrients to pass through the cell wall. Nanomaterials inactivate proteins, reducing membrane permeability and finally inducing cellular death[94].

CdONPs have a broad spectrum of bactericidal activity against both gram positive and gram negative bacteria [95].

When this comes into close touch with the bacterial outer surface, it may breach the cell wall and membrane. This might result in lipid injuries, in which huge volumes of phospholipids are removed from the bacteria via further vanderWaals and hydrophobic bond formation with the charged groups of GO. As a result, the pathogens' membrane integrity may be compromised, rendering several important activities including as respiration, materials transport and energy transduction ineffective. When the bacterial cell's surface is sufficiently covered by GO sheets, the cell becomes physiologically inactive and eventually dies, resulting in the creation of a clear zone of inhibition in the culture plate[88].

Tellurite ions (TeO_3^{2-}) have been studied earlier and are long known to be toxic, killing most Gram-negative bacteria at quantities lower than other dangerous metals. The bactericidal action of Te nanoparticles has been researched, and it has been linked to the generation of reactive oxygen species (ROS) when bacterial cultures are exposed. Furthermore, research shows that antibacterial activity appears to be closely related to nanoparticle dimensions: certainly, nanoparticles of smaller sizes had the strongest activity. The surface-to-volume ratio of nanoparticles increases as their size decreases, suggesting that smaller is better for enhancing biological reactivity [96].

According to Lin et al, Te nanoparticles exhibit stronger antibacterial activity and lesser toxicity [91].

Studies suggest that the TeO_2 NPs inhibit the growth *of E. coli, K. pneumonia and S. aureus bacteria*, Electrochemical and antimicrobial activity of tellurium oxide nanoparticles[97].

1.17 Cytotoxicity

Several studies mentioned that various nanoparticles may be cytotoxic and cause harmful effects or even irreversible damage to human cells [98].

Many studies have been conducted on the genotoxicity and cytotoxicity of NPs, including CdONPs. Cd is frequently utilized in industry and is one of the major environmental toxins that can harm humans through the food chain. Several in vitro and in vivo investigations have been conducted to assess the toxicity of CdO NPs. Their findings reveal that CdO NPs are harmful to live creatures, and that eukaryotic systems are more susceptible than bacterial cells [99].

Small particles have comparatively high surface areas, which allows for increased contact between particle molecules and biomaterials [100].

In vitro cytotoxicity tests were performed with human dermal fibroblasts (HDF) and human melanoma cells for 24 and 48 hours to determine the cytotoxic effect of green-synthesized TeNPs on mammalian cells. After 48 hours of testing, it exhibited a dose-dependent cytotoxic impact on the cells. The Te nanoparticles reduced cell growth in both healthy and malignant cell types. Cancer cells, on the other hand, degrade more rapidly and exhibit more cytotoxicity. Within an optimal range of 5 to 50 g/mL, TeNPs demonstrated both antibacterial and anticancer activities, as well as a low cytotoxic impact on human healthy cells. When nanoparticles are present in the medium, ROS generation increases, with a dose-dependent impact. As a result, an increase in the amount of reactive oxygen species is linked to dose-dependent anticancer activity. Several studies have revealed that Te compounds have anticancer properties, but only a few, if any, have proven this activity in tellurium nanomaterials [96].

Among the diverse metal nanomaterials that exist, cadmium-based nanostructures have piqued the interest of many researchers due to their multiple medicinal uses, particularly in the diagnosis, treatment, and targeted medication delivery of several kinds of cancers [101].

Data from investigations on Cd ion release from CdONPs and $CdCl_2$ cytotoxicity imply that the toxicity of the CdONPs was caused by the NPs themselves, rather than the released Cd ions, because the ions released from the NPs were low. These findings shed the light on cytotoxicity and genotoxicity in human and rodent cell lines, which may be utilized to estimate the danger of CdONPs[102].

Graphene toxicity on many cell types and genetic material is being investigated. GFN cytotoxicity factor has been studied in a number of recent investigations. GO nanosheets were proposed to efficiently intercalate into DNA molecules, and GO sheets combined with copper ions were shown to produce DNA scission. [103].

1.18 Environmental Application of the Prepared Materials

Dyes are considered one of the organic materials polluting water sources, because of their widespread use in various industries. They are used in dyeing, textile industries, in photographic colors, in addition to their use in many different broad fields[104]. Several techniques have been used to remove organic dye from water, including adsorption, which is considered a preferred method due to its low cost and ease of operation[105]. Adsorption is the phenomenon of a liquid or gaseous substance collecting in the form of molecules or atoms of a specific substance called an adsorbate on the surface of another solid substance called an adsorbent[105].

1.18.1 Types of Adsorption

Many studies indicate that the adsorption process can be classified into two types, as the occurrence of this process depends on the nature of the adsorbent material and the adsorbent surface[105]. If the connection between the molecules of the adsorbent material and the adsorbing surface is through weak Vander waals bonds, it is called physical adsorption, and it is defined as the physical attractive forces that occur between the adsorbing surface and the molecules that are adsorbed on the surface, and it is also written″for short(physisorption)[106].

Also, physical adsorption has a small activation energy that does not exceed (40 KJ/mol), and this type of adsorption occurs efficiently at normal temperature[107]. But if the bonding between molecules is with strong chemical bonds, it is called chemical adsorption, and it is called by this name because the surfaces in it tend to form covalent, chemical, or ionic bonds or a mixture of them with atoms, molecules and ions of the substance that is being adsorbed[108].

This process occurs on the surface of the solid material in a large way, and this type of adsorption is the first step of a chemical reaction, so it needs a high activation energy. Chemical adsorption gets on a specific surface under certain conditions of pressure and temperature, so this type of adsorption is selective. The heat content of this type of adsorption is much higher than that of physical adsorption, as it is about (80 KJ/mol)[109].

1.18.2 Factors Affecting on The Adsorption Process

a- Temperature

Both the extent and rate of adsorption are affected by temperature, as the rate of adsorption increases when the temperature rises and decreases when the temperature decreases. As for the extent of adsorption at low temperatures, it will rise and decrease with increasing temperature[110, 111].

b- Nature of Adsorbent

The efficiency of adsorption depends on the chemical and physical properties, and mainly on the chemical composition and the surface area of the adsorbing surface with respect to the presence of basic or acidic groups, since the surface area has a major role in the adsorption process. The greater the surface area, the smaller the adsorbent particles, the greater the number of active sites on the adsorbent surface, and hence the greater the adsorption capacity[112].

c- Nature of Adsorbate

The nature of the adsorbent affects the adsorption process, as the adsorption increases with the increase in the molecular mass of the adsorbent substance, and the adsorption process is affected by the chemical properties of the adsorbent in terms of the presence of effective groups in the composition of the adsorbent material from the absence of it, as well as its solubility in different solvents, as the lower the solubility.The adsorbent in solution increases the adsorption capacity[113].

d- Effect of Equilibrium Time

It means the time period after which there is no decrease in the concentration of the solution, or it is the time during which equilibrium occurs between the adsorbate and the adsorbent, and this time may be hours or days [114].

e- Concentration of Adsorbate

The amount of the adsorbent increases with increasing concentration, which leads to an increase in the adsorption capacity as a result of the increase in the rate of diffusion and mass transfer on the adsorbent surface [115].

1.18.3 Methyl Blue (MB) Dye

Methylene blue is a complex organic compound that has three cyclic structures attached in a chain. Sulphur and nitrogen are attached to the central ring, and chlorine is in a separate group and is negatively charged Molecular Formula – $C_{16}H_{18}ClN_3S$. Molecular Weight 319.9 mole/gm [116]. Figure (1-14) shows the chemical structure of methyl blue dye (MB).

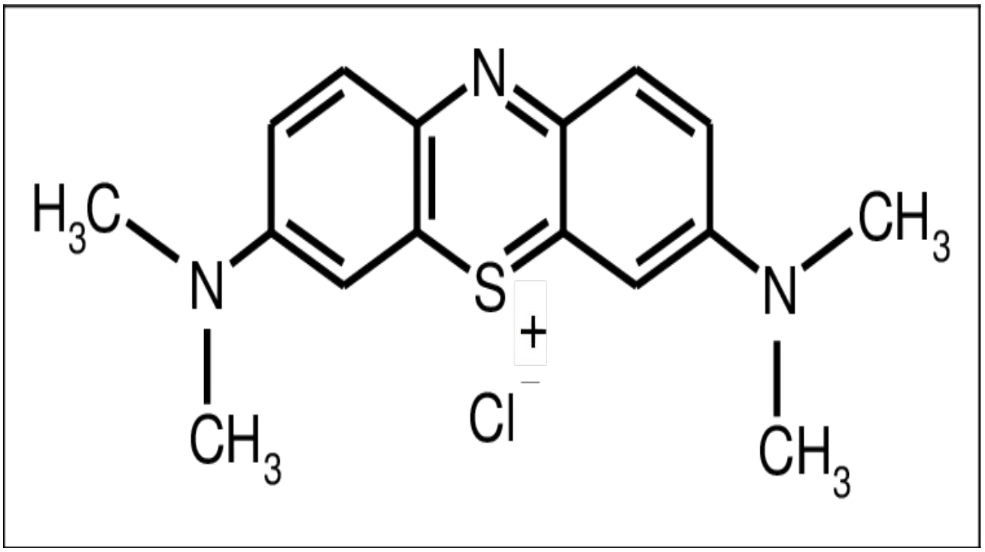

Figure (1-14) The main regions of the chemical structure of methyl blue dye(MB).

1.19 Previous Studies

- A.A. Dakhel, et al,(2010), Vacuum evaporation was used to create Te-doped CdO thin-films (1%, 3%, and 5%) on glass and silicon-wafer substrates. Experimental findings show that Te ions doping somewhat strains the host CdO crystalline structure and alters the optical and electrical characteristics. Because of a little (1%) doping with Te ions, the bandgap of the host CdO was unexpectedly decreased by around 23%. The effects of trap levels overlapping with the conduction band were used to explain the bandgap shrinking. The electrical properties of Te-doped CdO films reveal that they are degenerate semiconductors with bandgaps ranging from 1.7 to 2.2 eV. In comparison to undoped CdO film, 1% Te-doped CdO film increases mobility by around 5 times, conductivity by 140 times, and carrier concentration by 27 times. Finally, the absorption in the near-infrared spectral region was investigated using the traditional Drude theory[117].

-A. E. Ersundu, et al , (2011), CdO-WO3-TeO2 nanocomposite With decreasing TeO_2 concentration, the observed density values increased from 5.82 to 6.22 g/cm. The molar volume of glasses was discovered to grow as the amount of oxygen atoms increased. As the glass structure grows denser, the oxygen molar volume decreases. Refractive indices at 632 nm increased from 2.03 to 2.21 when TeO_2 concentration decreased due to the addition of cations with higher polarizability[118].

-Houlong L. Zhuang, et al, (2012) looked for single-layer oxide materials in the II-VI material family, and discovered that planar hexagonal CdO is a promising material with a low formation energy for upcoming synthesis attempts. According to calculations of the optical characteristics, the absorption is comparable to that of graphene. CdO may be a viable dielectric for graphene applications in electrical devices, according on estimates of the tunneling barrier of a graphene/CdO/graphene heterostructure[119].

-S. So¨nmezog˘lu , et al, (2013) CdO thin films with different Te concentrations were successfully synthesized by using sol–gel method. Also, the fluctuation of these thin films' structural, morphological, and optical characteristics as a function of Te concentration was examined. When Te was added to a thin layer of CdO, the strength of the typical peaks for pure CdO grew steadily as the Te doping concentration increased; Additionally, pure CdO thin films have smaller, more tightly packed grains, whereas doped CdO thin films have bigger, more porous grains[120].

-Chengyan Liu, et al,(2015) rGO/Te nanowires thermoelectric films were prepared, The simultaneous improvement of electrical conductivity (s) ,is essential to realize the thermoelectric materials with high power factor value. The transport characteristics of the hybrid films are also demonstrated based on the measurement of Hall effect. With the increased temperature, the electrical conductivities of the hybrid thin films increase[121].

- Sumeet Kumar, et al , (2016) showed that the nanocomposite CdO/rGO was created by growing highly distributed CdO NPs on rGO sheets using the hydrothermal technique. The current work offers information on the creation of a novel photocatalyst for the removal of organic compounds[122].

-Yao Jun Zhang, et al, (2018) showed that the CdO/graphene For the first time, an alkali-activated steel slag nanocomposite made of graphene and GASSN-loaded CdO was employed to photocatalyze the breakdown of DFB dye wastewater [123].

-Solleti Goutham , et al, (2019) showed that CdO/graphene nanocomposite can be placed as a film on interdigitated electrodes (IDEs), which were then utilized to detect liquid petroleum gas (LPG) chemically using a four probe approach. A LPG exposure greatly reduces a resistivity. It was also possible to examine the flexibility of the sensor by performing mechanical bending; the response was unaffected even when the sensor was bent with a 5 mm radius. The CdO/graphene nanocomposite sensor's optimal graphene content created electrotransfer routes between nanostructured CdO, which helped to reduce the CdO crystallite size[124].

-Sourav Sadhukhan ,et al ,(2019) showed that the CdO/rGO nanocomposite was made utilizing a hydrothermal process. It has been noted that the RGO/CdO nanocomposites exhibit greater electrical conductivity than RGO alone. As a result, it might be a helpful material for many electrical applications. Comparable to CdO NPs and significantly more effective than RGO alone, the antibacterial activity of the nanocomposites has been proven to be effective and safe in the realm of biological applications compared to hazardous CdO. The creation of metal oxide (CdO) adorned RGO nanocomposites via a green approach, as well as the potential applications, are thus indicated by the current work[125].

-Reda Hassanien, et al, (2019) synthesized cadmium oxide and graphene nanocomposite. The outcomes demonstrated that the reduction of graphite to graphene was effective . The production of the CdO NPs was confirmed by FT-IR due to the existence of strong and distinct peaks at 556 and 602 cm1 (Cd-O stretching). CdO NPs had a 260 nm absorption peak with a large direct bandgap (3.11 eV) The results show that this method may be used to synthesize additional metals or metal oxides on graphene sheets and suggest that it may have a variety of biological, industrial, and technological uses[126].

-Hui Wang ,et al , (2020) cite the growing interest in water treatment caused by graphene materials. The adsorption characteristics of cadmium were examined in this work, which also used the modified Hummers technique to create magnetic graphene oxide (MGO). First, the impacts of pH as well as the sorption kinetics and isotherms were examined [127].

-Ashwini P. Alegaonkar, et al, (2020) prepared the Te-rGO nanocomposite, Graphene derivatives has persuasive absorbing ability and its electron transport capacity makes it a great prosperity in many science horizons. Our diffuse reflectance spectra (DRS) studies indicate that Te-rGO has a significant amount of increase in light absorption and red shift in absorption peak[128].

-Dalal Z. Husein, et al, (2021) showed that CdO/G nanocomposite had been prepared, Due to their huge specific area, quick kinetics, and particular affinity towards heavy metal impurities, graphene-based metal oxide nanocomposites are intriguing and promising types of nanocomposites. In this study, CdO nanoparticles (CdO NPs) and a graphene-based CdO nanocomposite (G-CdO) were made using an easy and affordable method. The produced nanoparticles were examined and evaluated for their potential to remove lead from water[129].

1.20 The Aim of The Research

This study aims to prepare the CdONPs, TeO_2NPs, GNS, TeO_2NPs/ CdONPs/GNS nanocomposite (Mix 1) and TeO_2NPs/CdONPs/GNS nanocomposite (Mix 2) by using Q-switched Nd-YAG pulsed laser ablation in water, to using in removing pollutants and some biology application's such as (Some of Bacteria types).

2.1 Introduction:

This chapter describes the synthesis and spectroscopic instruments of CdONPs, TeO_2NPs, Graphene Nano Sheet (GNS), CdONPs/TeO_2NPs/GNS (Mix1), and CdONPs/TeO_2NPs/GNS (Mix2) nanocomposite synthesized by laser ablation in liquid (PLAL). Finally, the structural and optical properties of the prepared samples were characterized using X-ray diffraction, FE-SEM, FTIR, and UV-Vis Absorption spectroscopy.

2.2 The Materials Used:

Figure(2-1) show the sample of a laboratory-prepared graphite target.

Figure (2-1): Graphite target.

Table (2-1): Shows the materials used in this study.

materials		*Company*	*Country*	*purte*
Graphite powder		-	china	99.99%
Cadmium powder		-	china	99.99%
Tellurium powder		-	Iran	99.99%
Distilled water		-	Iraq	99.99%
Ethanol		France Alcools	France	99.99%
Fetal bovine serum (FBS)		Capricorn	Germany	99.99%
MTT(3-(4,5-Dimethylthiazole-2-yl)-2,5-diphenyl-2H-tetrazolium bromide) dye powder		Roth	Germany	99.99%
Penicillin-streptomycin solution		Capricorn	Germany	99.99%
Phosphate buffer saline packets		BioPLUS chemicals	USA	99.99%
RPMI 1640 medium w/L-glutamine, 25mM HEPES (powder)		US Biological life science	USA	99.99%
Sodium bicarbonate powder		Ludeco	Belgium	99.99%
Trypsin-Ethylene diaminetetraacetic acid (EDTA) powder		US biological	USA	99.99%
Millipore filter (0.45mm) Millipore filter (0.22mm)		Biofil	Italy	99.99%
Benson burner		Membrane	Germany	99.99%
Petri dishes 99.99%		Afeco	Jordan	99.99%
Slides		Afeco	Jordan	
Platinum Wire Loop		Afeco	Jordan	

Micropipette tips		Afeco	Jordan	
Plastic test tubes 10 ml		Afeco	Jordan	*purte*
Muller –Hinton agar		Himedia	India	99.99%
Nutrient agar		Himedia	India	99.99%

2.3 Equipment Used for The Measurement of The Prepared Materials:

This study used a variety of instruments, which are listed in Table (2-2) along with the nations that manufactured them and the site of the work.

Table (2-2): List of Instruments and Tools Used in the Study.

Instrument	Company's	Country
Q-Swiched Nd -YAG laser	-	China
UV-Vis Spectrophotometer	-	Japan
X- Ray Diffraction (XRD)	-	Japan
Fourier Transform Infrared Spectrophotometer (FTIR)	-	Germany
Field Emission Scanning Electron Microscopy(FE-SEM)	USA	USA
Oven	-	China
Autoclav	Jeiotech	Korea
Cell culture flask (25ml)	SPL	Korea
Cell culture plate (96- wells)	SPL	Korea
Centrifuge	Rotanta	Germany
Distiller	ROWA	Germany
Double distillation water stills	GFL	Germany

Electric oven	Memmer	Germany
ELISA Reader	Human	Germany
Eppendorf centrifuge 5702 RH	eppendorf	Germany
Incubator	Memmert	Germany
Inverted microscope	T.C Meiji techno	Japan
Laminar airflow cabinet	Labtech	Korea
Micropipettes (different sizes)	Dragon-Med	India
Millipore filter (0.45, 0.22µm)	Biofil	Australia
Refrigerator	Arcelik	Turkey
Sensitive Balance	Labtech	Korea
Syringe 5 ml	MED	China
Water bath	Memmert	Germany

2.4 Laser Ablation System:

The Q-Switched Nd-YAG pulsed laser was used to fragment solid pellets of Te, Cd, and graphite powder and their mixtures in water to obtain TeO_2NPs, CdONPs, GNS, and CdONPs/TeO_2NPs/GNS (Mix1) and CdONPs/TeO_2NPs/GNS (Mix2) nanocomposite as shown in Figure (2-1, a and b). The laser parameters utilized in pulsed laser ablation in liquids are listed in Tables 2 and 3 (PLAL-Method).

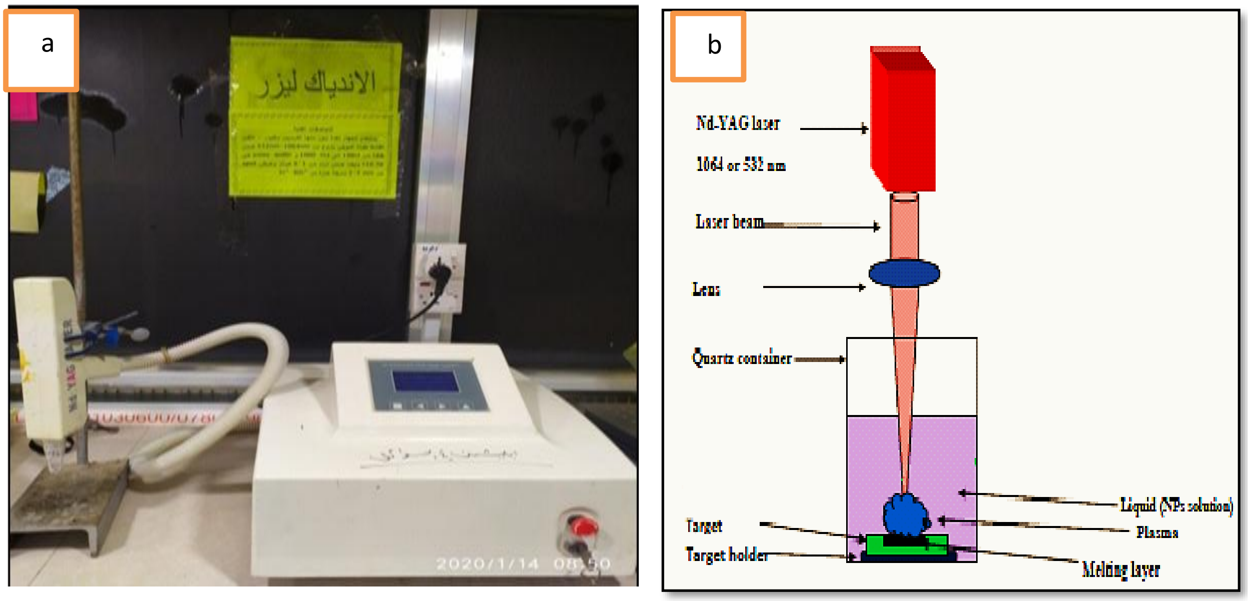

Figure (2-2): a) Q -Switched Nd-YAG laser device.

b) Set up of pulsed laser ablation in liquids.

Table (2-3) The parameters that are used through pulsed laser ablation in liquids (PLAL)

Parameters	**Standard Values**	**Used Values**
Energy (mJ)	1-1000	80
Wavelength (nm)	1064	1064
Pulse duration (ns)	10	10
Pulse repetition rate (PRR)(HZ)	6	6
No. of Pulses	40-1000 pulses	500 pulses

2-5 Preparation of TeO_2NPs , CdONPs, GNS and CdONPs /TeO_2NPs/ GNS Nanocomposite:

2-5-1 Preparation of Cd, Te and graphite pellets (discs):

Cadmium (Cd), Tellurium (Te), and Graphite powders were weighed and compressed by a hydraulic piston JB/T3818-1999 type, which had previously been cleaned with ethanol, to produce a pellet with a diameter of 2 cm and a thickness of 5 mm, which was then placed in an oven type WG43 at a temperature of 500 °C for one hour to anneal the samples, as shown in Figure (2-2, b).

Figure (2-3): a) The hydraulic piston, b) Vacuum oven

2-5-2 Synthesis of CdONPs, TeO$_2$NPs, GNS, CdONPs / TeO$_2$NPs / GNS (Mix1) and CdONPs /TeO$_2$NPs / GNS (Mix 2) by (PLAL-Method):

The materials were prepared by the laser ablation method as shown in the flowchart illustrated in Figure (2-3):

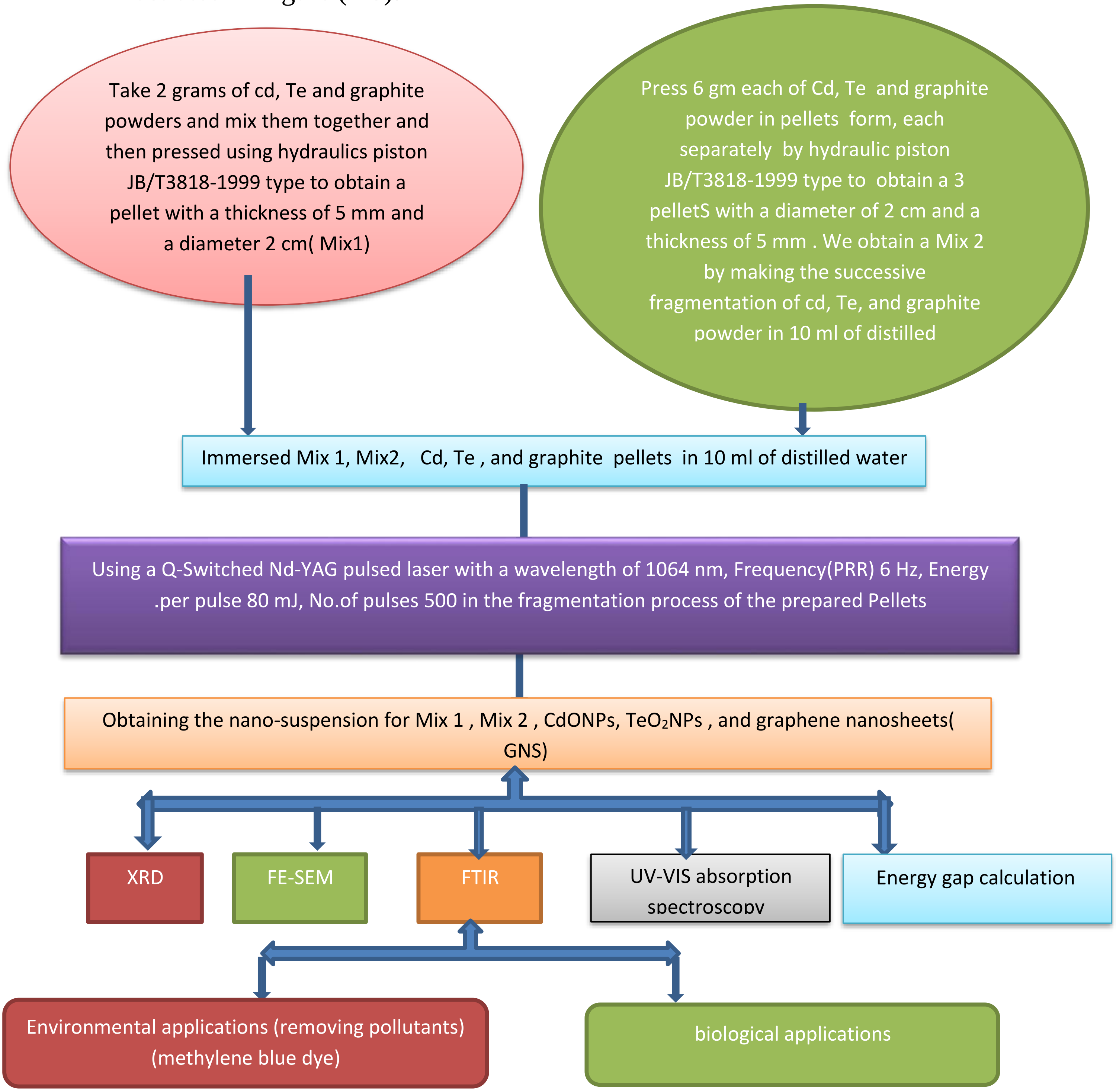

Take 2 grams of cd, Te and graphite powders and mix them together and then pressed using hydraulics piston JB/T3818-1999 type to obtain a pellet with a thickness of 5 mm and a diameter 2 cm(Mix1)

Press 6 gm each of Cd, Te and graphite powder in pellets form, each separately by hydraulic piston JB/T3818-1999 type to obtain a 3 pelletS with a diameter of 2 cm and a thickness of 5 mm . We obtain a Mix 2 by making the successive fragmentation of cd, Te, and graphite powder in 10 ml of distilled

Immersed Mix 1, Mix2, Cd, Te , and graphite pellets in 10 ml of distilled water

Using a Q-Switched Nd-YAG pulsed laser with a wavelength of 1064 nm, Frequency(PRR) 6 Hz, Energy .per pulse 80 mJ, No.of pulses 500 in the fragmentation process of the prepared Pellets

Obtaining the nano-suspension for Mix 1 , Mix 2 , CdONPs, TeO$_2$NPs , and graphene nanosheets(GNS)

Figure (2- 4): Flowchart for preparing CdONPs TeO$_2$NPs, GNS, CdONPs / TeNPs / GNS (Mix1) and CdONPs /TeO$_2$NPs / GNS (Mix 2) by pulsed laser ablation in water (PLAL).

2.6 Measuring Instruments:

2.6.1 X-Ray Diffraction (XRD):

The crystal structures of CdONPs, TeO_2NPs, GNS, CdONPs/TeO_2NPs/GNS (Mix 1), and CdONPs/TeO_2NPs/GNS (Mix 2) films were determined using X-ray diffraction equipment. The crystal structure, orientation, and grain size may all be determined using X-ray diffraction, which is a strong non-destructive approach for material characterization. A typical X-ray wavelength that is equivalent to the interatomic distance in a crystal is used for characterization. When the path difference is an integer multiple of the wavelength, constructive interference occurs. This is the diffraction Bragg condition. In the corresponding directions, the intensity of the reflected beam exhibits distinct peaks. They're known as the Bragg peaks. The Bragg peak can be detected by changing the detector's angle (2θ).

$$2d \sin \theta = m\lambda \quad \ldots\ldots\ldots\ldots\ldots\ldots\ldots\ldots\ldots\ldots\ldots\ldots \text{(2-1)}$$

Where m is an integer, Scherer's formula measures the grain size (D) in a polycrystalline film,:

$$D = \frac{0.9\,\lambda}{\beta\, COS\theta} \ldots\ldots\ldots\ldots\ldots\ldots\ldots\ldots\ldots (2-2)$$

Where β :is the full width at half maximum (in radians) of the peak (FWHM), (θ) :is the Bragg angle. The structure of the samples was investigated using a Shimadzu 6000 X-ray diffractometer (Made in Japan) (λ=1.5406 A^0). Figure (2-4, a and b) illustrates the image and diffraction of a beam of parallel and monochromatic X-rays of wavelength (λ) incident at an angle (θ) on a crystal. A proportional counter with a 40 kV operating voltage and a 30 mA current was used. XRD has a scanning speed of 8 degrees per minute and a range of 5 to 80 degrees. Only if the wavelength in equation (2-1) is less than or equal to twice the distance between two successive planes in the crystal can Bragg diffraction occur.

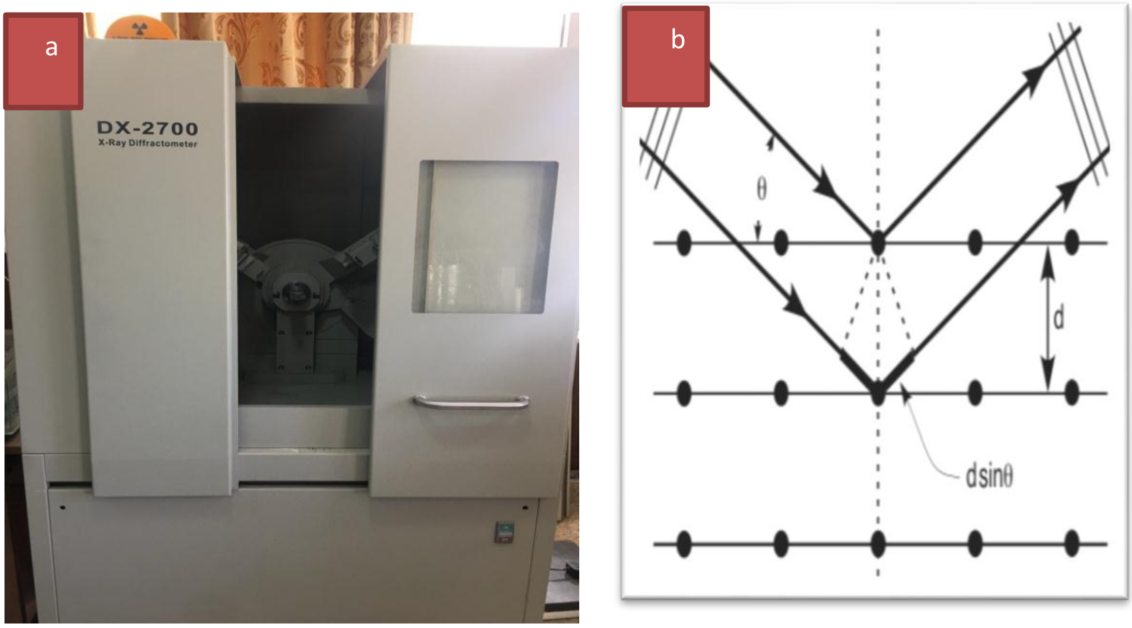

Figure (2-5): a) XRD device used to measure the prepared samples. b) The mechanism of work of the XRD.

2.6.2 Field Emission Scanning Electron Microscopy (FE-SEM):

It is a sort of electron microscope that scans a sample with a beam of electrons rather than light waves, and these electrons are released with a field emission source (electron Gan) in which the sample is scanned in zigzag patterns and accelerates in the high gradient of the electric field. High vacuum columns of primary electrons are fixed by electronic lenses to prepare the narrow scanning beam that bombards the material, and secondary electrons and back-scattered electrons emerge from every point on the body as a result. Figure (2-5, a and b) shows the image of the high resolution scanning electron microscope used in the research (type-INSPECT F50 DS0019_09-11-HOLAND), in which the detectors of this device receive electrons liberated and convert them into an optical image that can be displayed on a screen or a digital image, resulting in a 3D image.

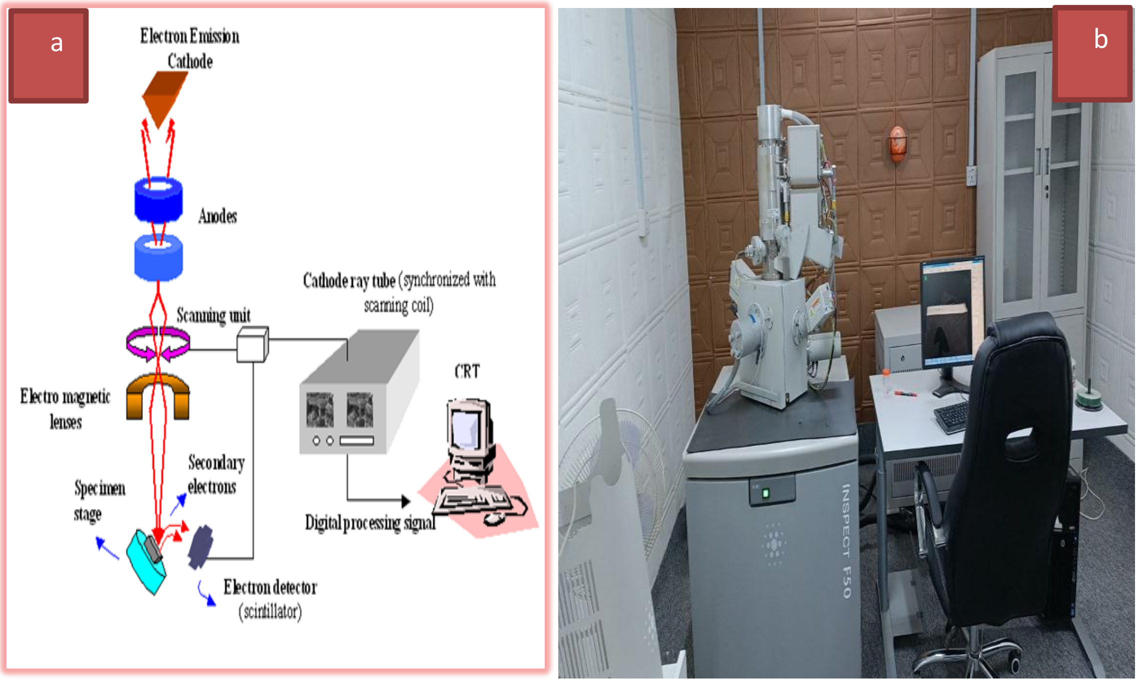

Figure (2-6): a) FE-SEM device used to measure the prepared samples. b) Main components of FE-SEM

2.6.3 Fourier Transform Infrared Spectroscopy (FTIR):

The FTIR technique is used to investigate the structural properties of solids, liquids, and gases. It allows for the investigation of materials' absorptive and emissive characteristics. The FTIR method's choice of IR wavelengths is very beneficial for analyzing chemical bonds that link atoms. These bonds, it turns out, vibrate at frequencies that correspond to infrared wavelength light, and can thus be easily excited by such radiation. By placing some drops in the device (type ALPHA, Germany), the prepared samples were analyzed at room temperature, and the instrument worked within the range (400cm^{-1} - 4000 cm^{-1}). The FTIR device is shown in Figure (2-6, a and b).

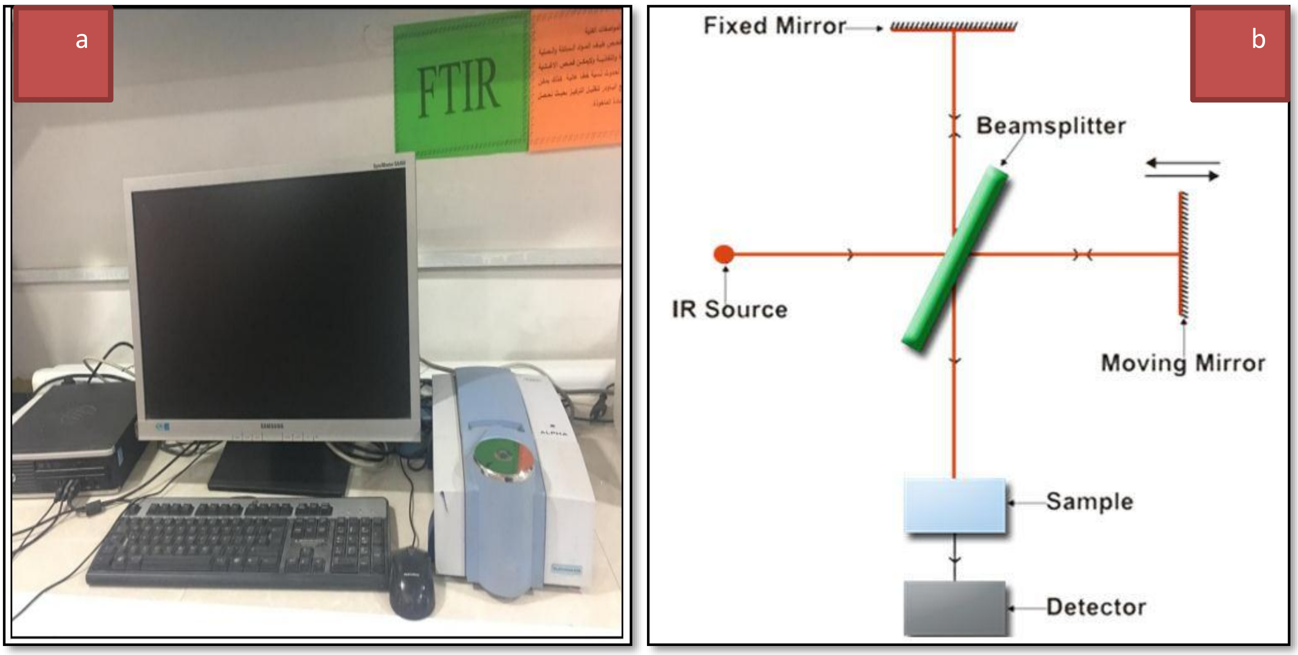

Figure (2-7): a) FTIR device used to measure the prepared samples. b) Main components of FTIR.

2.6.4 UV-Visible Absorption Spectroscopy:

The absorption spectra of TeO_2NPs, CdONPs, GNS, Mix1 and Mix2 nanocomposite solutions were measured using UV-Visible absorption spectroscopy, CECIL CE 7200 (ENGLAND), where the colloidal solutions were placed in a quartz container after the calibration process and filtering of the device. After that, the optical properties (absorption, absorption coefficient, and energy gap) were calculated for all the prepared samples. Figure (2-7, a and b), shows the devices used in the research. The electronic spectrum of the compound is a curve that illustrates the change in absorption intensity as the wavelength of the rays passing through the solution of the compound under study changes. The purpose of this curve is to determine the wavelength at which the absorption intensity is highest, and it is symbolized by the symbol λ_{max}. The absorption spectrum covers the range from 190 nm to 1100 nm.

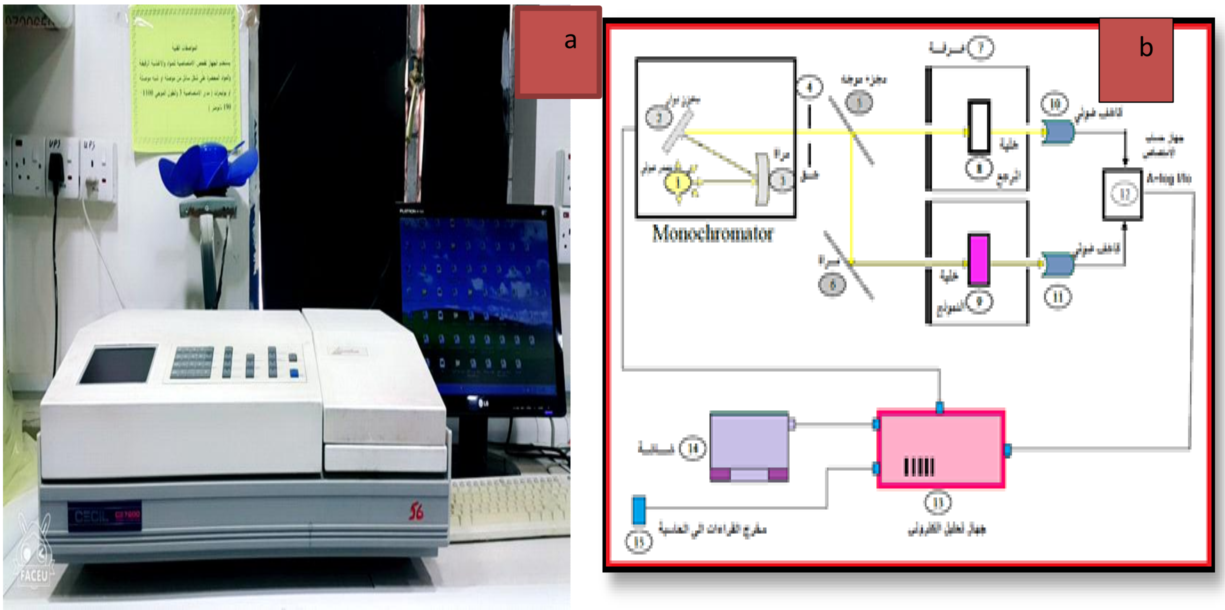

Figure (2-8): a) UV-Visible spectroscopy device used to measure the prepared samples. b) The Main components of the device.

2.7 Environmental Application of CdONPs, TeO_2NPs, GNS, CdONPs / TeO_2NPs / GNS (Mix1) and CdONPs /TeO_2NPs / GNS (Mix 2) :

By adding (0.00319 gram) of methyl blue dye powder to a baker containing (10 ml) of distilled water according to the equation (2-3), a solution of methyl blue dye (MB) at a concentration (10^{-3} M) was prepared :

$$w = \frac{M \times V \times c}{1000} \ldots\ldots\ldots\ldots\ldots\ldots\ldots\ldots\ldots (2-3)$$

So that: W: the weight of dye required to achieve the desired concentration in gm, c: the molarity unit concentration , V: the amount of solvent to be applied to the material in cm^3, M: 319.9 is the molecular weight of the dye in gm/mol. In addition, the prepared concentration was diluted using the dilution relationship below by adding a given amount of solvent (distilled water) to a specific volume of high concentration.

$C_1V_1 = C_2V_2$ ………………………….....(2 – 4)

C_1: The first concentration (high), V_1: The amount of high concentration required, C_2: The second concentration (light), V_2: the volume required to add to the first concentration to get the second concentration.

2.8 Cell lines

Frozen vials of prostate cancer cells (LNCaP) and normal cells (Vero) cell lines were received from the cell culture technique laboratory in the college of medicine/university of Babylon.

2.8.1 Preparation of reagents and solutions

2.8. 1.1 Phosphate buffer saline (PBS):

According to the manufacturer manual, the PBS was prepared by dissolving only one packet in 500 ml of deionized distilled water (DDW) with continuous stirring by a magnetic stirrer at room temperature resulting in a PH value of 7.45 with out need for adjustment. Autoclaving is required for compling sterilization and then the PBS was stored in a closed bottle until used to keep sterile.

2.8.1.2 Trypsin-ethylene diamine Tetraacetic Acid (EDTA) solution:

As indicated by US biological headings, a weight of 10.1g of trypsin-EDTA powder was dissolved in 0.9 liter of DDW with continuous mixing at room temperature. 7.2 of PH value was reached then the volume was completed to 1 litre by DDW, the solution was sterilized using millipore filters of 0.45 and 0.22 μm respectively, after that, the solution was kept at (- 20°C) temperature.

2.8.1.3 Preparing MTT assay solution:

The general purpose of the MTT assay is to measure the viability of the cells in relatively high throughput (96-well plates) with no need for cell counting. Therefore, the most usual use of MTT assay is to find out the cytotoxicity of many drugs at various concentrations. The concept of the MTT assay is to detect the cellular mitochondrial activity of the viable and thereby a rise or decline in the number of viable cells is related to the mitochondrial activity. The mitochondrial activity of the cells is indicated by the changing of the pale-yellow tetrazolium salt (MTT dye) into dark purple formazan crystals by NADH which can be solubilized for homogenous measurement. Thus, any increment or decline in the number of viable cells can be noticed by measuring formazan concentration that is indicated by the measurements of optical density (absorbance) using a plate reader at 570 nm. The darker the solution, the greater the number of viable and metabolically active cells. The following MTT Procedure was performed according to [130]:

1- At the end of the drug exposure period, the media were withdrawn from the wells and rinsed with PBS. To measure unspecific formazan conversion, a blank control used.

2- A volume of 1.2 ml of MTT solution (5 mg/ ml) was added to 10.8 ml medium to obtain final concentration of 0.5 mg/ml. Then, 200 μl of the resulting solution was added to each well.

3- The plate was incubated for three hours at 37°C till intracellular purple formazan crystals were detectable by the inverted microscope.

4- The supernatant was removed and 100 μl DMSO was added to each well to dissolve the formazan crystals.

5- The plate was incubated for 30 minutes at room temperature until the cells had lysed and the purple crystals had dissolved.

6- Absorbance was measured by a microplate reader at 570 nm.

The absorbance of the blank must be subtracted from all samples. The absorbance of the test samples must then be divided by those of the control and multiplied by 100 to give percentage cells viability or proliferation. Absorbance values greater than the control indicate cell proliferation, while lower values indicate cells death or inhibition of proliferation. The percentage of cells viability or percentage of inhibition was calculated by the following formula:

% viability = (AT – AB) / (AC – AB) × 100%

Where, AT = Absorbance of treated cells (drug).

AB = Absorbance of blank (only medium).

AC = Absorbance of control (untreated).

% Inhibition = 100 – % viability

2.9 Preparation of bacterial Culture Media:

It was prepared according to the instructions of the company and sterilized by autoclaving at temp.121^{o}C for 15 min.

2.9.1 Nutrient Agar Medium

This nutrient agar was prepared according to the instruction of supplier company by dissolving 28gm of nutrient agar in 1L of distilled water then sterilized in the autoclave at 121 ^{o}C for 15 min. , this medium was used in general experiment such as cultivation and activation of bacterial isolates when it necessary.

2.9.2 Müller-Hinton agar

This medium was prepared according to the instruction of supplier company by dissolving 38gm from the medium in 1L of distilled water and sterilization by autoclave at 121 ^{o}C for 15 min., this medium used an antibiotic sensitivity test.

2.10 Preparation of tissue culture medium

Liquid RPMI-1640 medium was prepared according to US Biologics from RPMI-1640 medium powder as follows:

An amount of 16.353 grams was dissolved in 900 ml of DDW without heating, 2 g of sodium bicarbonate can be added with gentle stirring to adjust pH additional water was added to obtain 1 liter then filtered using a 0.22 µm syringe filter. A 1% penicillin-Streptomycin and 10% fetal bovine serum was added then filter-sterilized using a 0.22-micron membrane filter. The mixture contains heat-labile compounds that can be damaged with autoclaving. The prepared media should be kept at 4°C and used within a short period.

2.11 Preparation of cell line

2.11.1 Thawing of frozen cell lines

The frozen cell lines vials were removed from the liquid nitrogen container with caution and directly placed into a beaker containing pre-warmed (37°C) sterile DDW. The vials were removed from the water before the ice floccule dissolved completely, and then they were wiped with 70% ethanol. Without delay, the cell suspension content of each vial was pipetted under a laminar flow cabinet into a 15 ml sterile plastic centrifuge tube containing 10 ml of pre-warmed serum-free medium. Centrifugation was done at 1000 rpm for 5 minutes and the supernatant was aspirated and decanted. The cells pellet was resuspended into 5 ml warm (37°C) serum-medium and transferred into a 25 ml size cell culture flask, incubated at 37°C and the serum medium replaced on the next day.

2.11.2 Sub-culturing of cell culture

1- The cells were checked and analyzed using an inverted microscope to ensure that they were healthy, sub-confluent, and free of contamination.

2-Using a pipette, the growth medium was removed from the flask, and the monolayer was washed with enough volume of PBS to remove all of the media from the flask.

3-To allow the cells to detach from the flask's interior surface, a suitable volume of trypsin/EDTA solution was applied to the flask and incubated at 37°C (for 2-10 min).

4-An inverted microscope was used to inspect the cells to confirm that they were all separated and suspended. To release any remaining detached cells, the flask was lightly taped with the palm a couple of times.

5-Trypsin was inactivated in the flask by adding an equal volume of the serum-containing medium.

6-The cell suspension was then split into two flasks, each with a cell line name, passage number, and date labelled on it.

7-The cell line was incubated at 37°C for 24 hours[131].

2.11.3 Maintenance of cell culture

Cells were routinely checked under an inverted microscope for any contamination and the cells were given a new medium (RPMI) every 2 to 3 days based on color changes. The cells were maintained in supplemented medium with 10 % serum and kept at 37 ºC in an incubator. After the cells have achieved more than 80 % confluence, they were subcultured.

2.11.4 Harvesting of cell culture

Harvesting is a technique that uses proteolytic enzymes to separate adherent cells from the surface of the flask. First, the growth medium in the vessel was aspirated and discarded. PBS was used to wash the cells twice. Afterwards, the enzymatic harvesting solution (containing trypsin) was added to the vessel. After 15 minutes, the proteolytic reaction was neutralized by adding the serum-containing culture medium. The cells in the tissue culture flasks were harvested by using different enzymatic solutions composed of different concentrations of trypsin and EDTA[132].

2.12 Cytotoxicity measurement of nanomaterials on the normal and cancer cells.

Cells were cultured in 96 tissue culture plates. Cells were treated with different nanoparticles (four replicates were used for each contype) along with four replicates of untreated cells (control group). The plate was then incubated for 24 hours, after which the cell growth was measured using the MTT cytotoxicity assay. Calculation of cell viability was done by dividing the measured absorbance for each concentration by the absorbance of the control multiplied by 100.

Cell viability = (complete absorbance /cells only absorbance) * 100 = % cell survival

2.13 Statistical analysis

Microsoft Office Excel 2016 and Sigma plot version 12.5 software were used to analyze the data. The ANOVA one-way test was employed to determine whether there were significant differences between the data means. The p-values ($p \leq 0.05$) was declared statistically significant.

3-1 Introduction:

The results of the prepared materials CdONPs, TeO_2NPs, GNS, and CdONP s/TeO_2NPs/GNS (Mix1) and CdONPs/TeO_2NPs/GNS (Mix 2) were discussed in this chapter using XRD, FE-SEM, FTIR, and UV-visible spectroscopy, as well as the results of their application.

3-2 Results of X-Ray Diffraction measurements:

Figure (3-1 a) displayed the strong diffraction peaks at angles of $2\theta = 26.6^0$ and 54.7^0, which corresponded to Miller indices of (002) and (004), respectively. The distance between the crystal levels was d = 3.3858 A°, which is attributed to commercial graphite powder. It's in agreement with that reported in ICDD Grant-in-Aid, (1990). Figure (3-1 b), it indicates the presence of a very small diffraction peak at an angle of 26.9^0, corresponding to Miller's index (002), which is almost negligible in comparison with the graphite powder peak. This peak is due to the formation of graphene nanosheets (GNS), identical to what was stated in the international card ICDD Grant-in-Aid (1990).

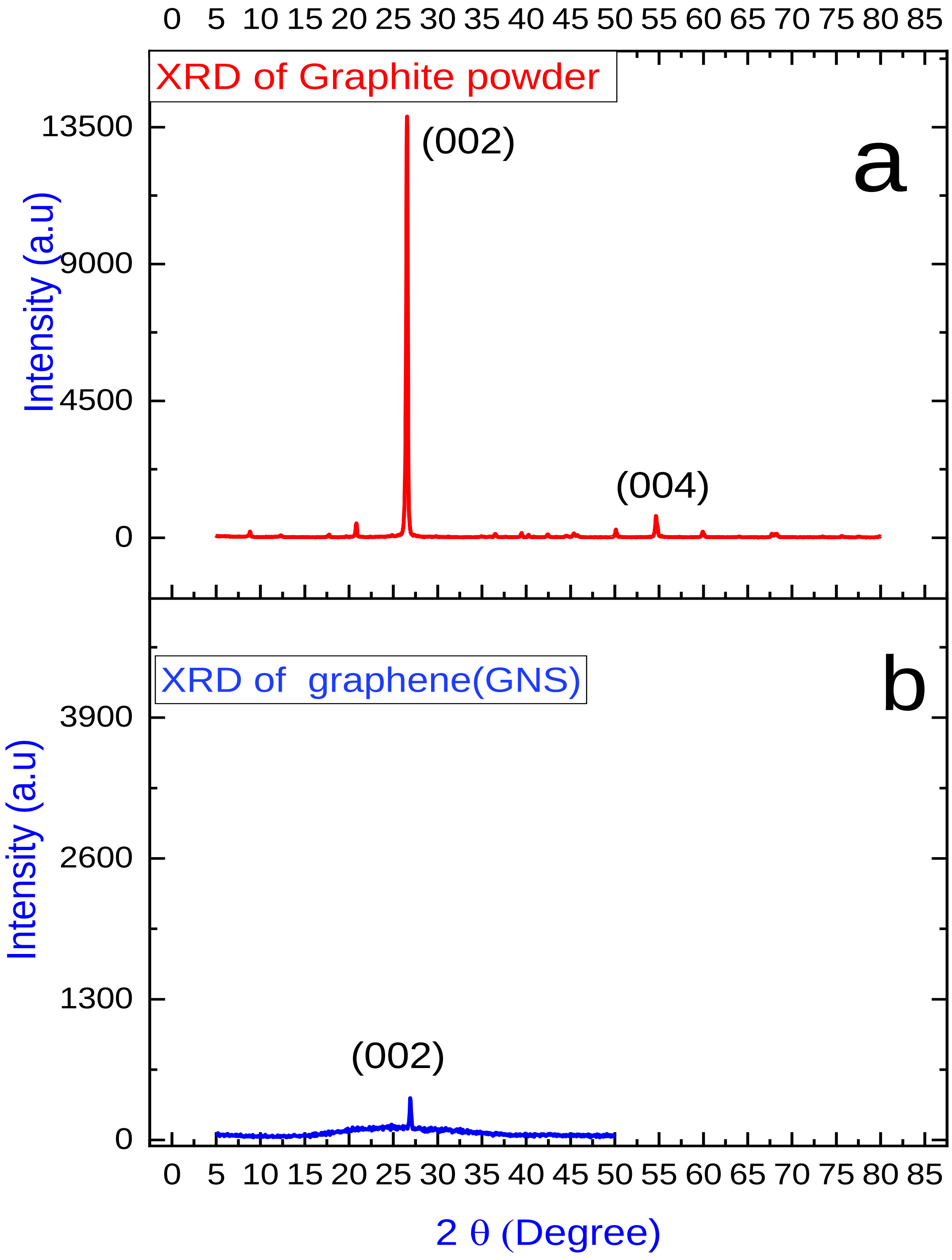

Figure (3-1) : a- XRD of the commercial graphite b- graphene nanosheets(GNS) were prepared by pulsed laser ablation in distilled water.

The diffraction peaks at 32.5 °, 37.80 °, and 54.80 °, which correspond to Miller indices (001), (200), and (220) respectively , are due to the formation of CdONPs. which clearly indexed as a cubic phase of CdO. It's in agreement with that reported in ICDD Grant-in-Aid, (1990), as shown in Figure (3-2).

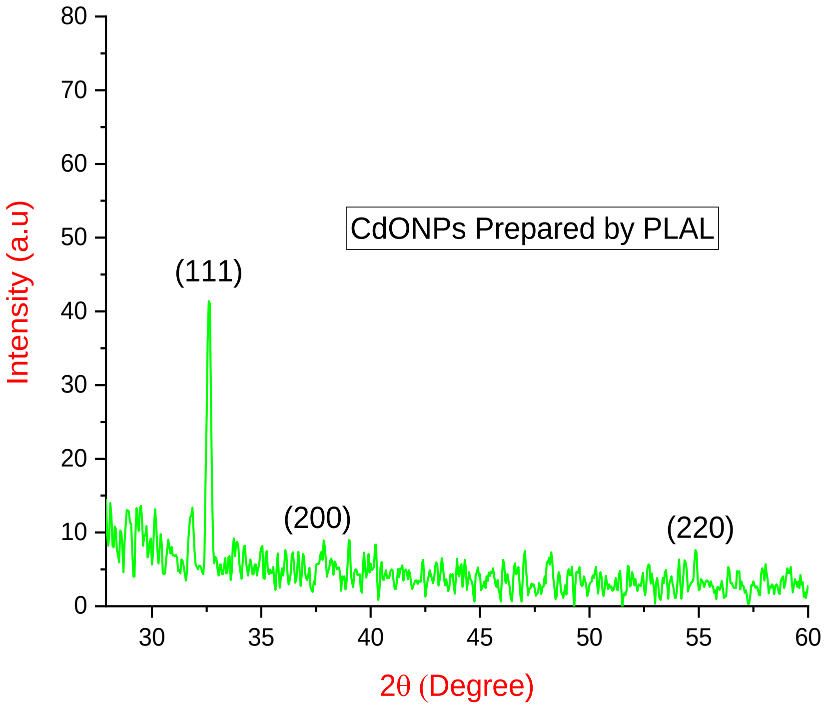

Figure (3-2) :XRD of CdONPs prepared by pulsed laser ablation (PLAL).

Figure (3-3) illustrates the peaks at angles of 26.7^0, 29.6^0, and 33.2°, which correspond to miller indices (100), and (210), respectively, which indicate the formation of TeO_2NPs ,which clearly indexed as a hexagonal phase of TeO_2 and is in agreement with that reported in ICDD Grant-in-Aid, (1990).

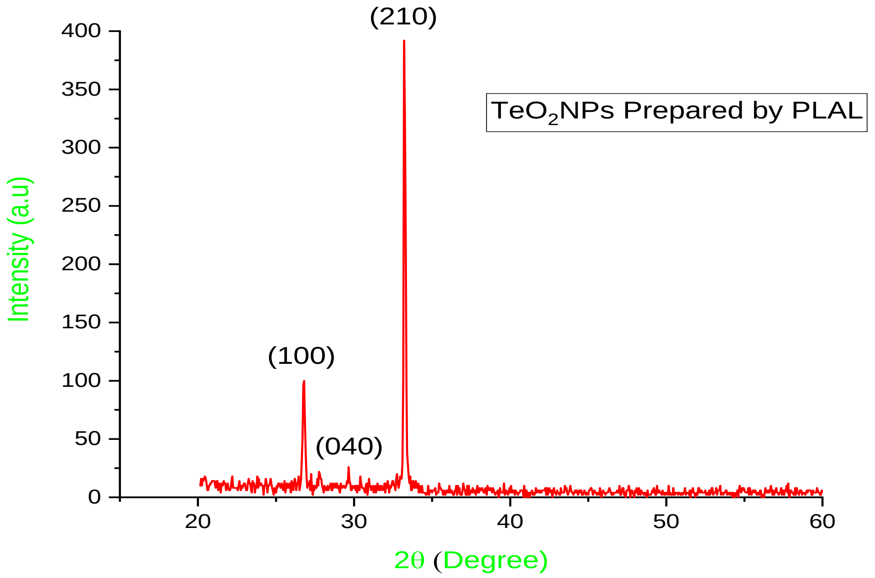

Figure (3-3):XRD of TeO2NPs prepared by pulsed laser ablation (PLAL).

Figure (3-4) shows the diffraction peaks at angles of 33.1^0 and 38.6^0, which correspond to Miller's indices (111) and (200) respectively due to the formation of CdONPs in CdONPs /TeO_2NPs /GNS(Mix1) nanocomposite, but the diffraction peaks at angles of 24^0 and 26.8^0, which correspond to Miller's indices (111) and (100) respectively due to the formation of TeO_2NPs in CdONPs/TeO_2NPs/GNS nanocomposite (Mix1). It is in agreement with that reported in the ICDD Grant-in-Aid, (1990). The highest orientation (crystal growth) of the peak is at (100) for TeO_2NPs in nanocomposite instead of (111) and (210) for individual CdONPs and TeO_2NPs respectively, and this indicates the dominance of TeO_2NPs in nanocomposite. It is noted that a rearrangement of the atoms occurs. The mixing process led to crystal growth at a Miller's index of (111) for CdONPs, and this is evident by the increase in intensity compared to CdONPs before mixing. No diffraction peak of graphite was observed in the CdONPs /TeO_2NPs /GNS nanocomposite (Mix1) nanocomposite, indicating that graphite had completely transformed into graphene nanosheet (GNS).

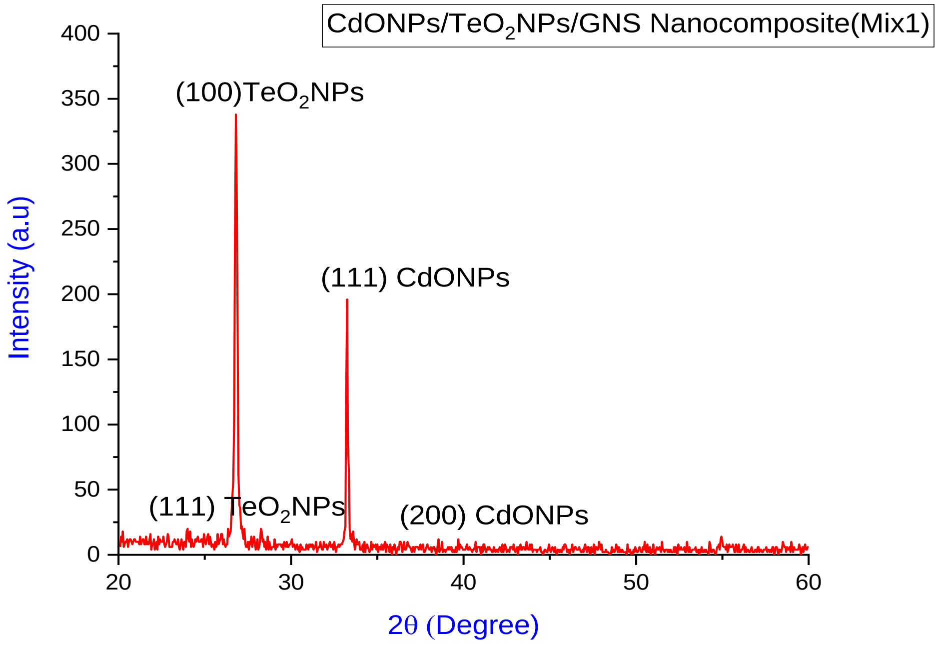

Figure(3-4):XRD of CdONPs / TeO$_2$NPs / GNS Nanocomposite (Mix1) prepared by pulsed laser ablation (PLAL).

Figure(3-5) shows that the diffraction peaks at angles of 27.4^0, 29.7^0, 45.7^0, 52.8^0, and 57.1^0, which correspond to Miller's coefficients (100), (040), (042), (311) and (133), respectively, are due to the formation of TeO$_2$NPs in the CdONPs/TeO$_2$NPs/GNS nanocomposite (Mix2). At the angle of 38.1^0, which corresponds to Miller's index (200) due to the formation of CdONPs in CdONPs/TeO$_2$NPs/GNS nanocomposite (Mix2). It is noted that a rearrangement of the atoms occurs. As the peak at (210) for the TeO$_2$NPs and the peak at (111) for the CdONPs disappeared, peaks are appeared and emerged at (100) for TeO$_2$NPs and (200) for CdONPs. The dominance of TeO$_2$NPs on both CdONPs and GNS is observed in the CdONPs/TeO$_2$NPs/GNS nanocomposite (Mix2).

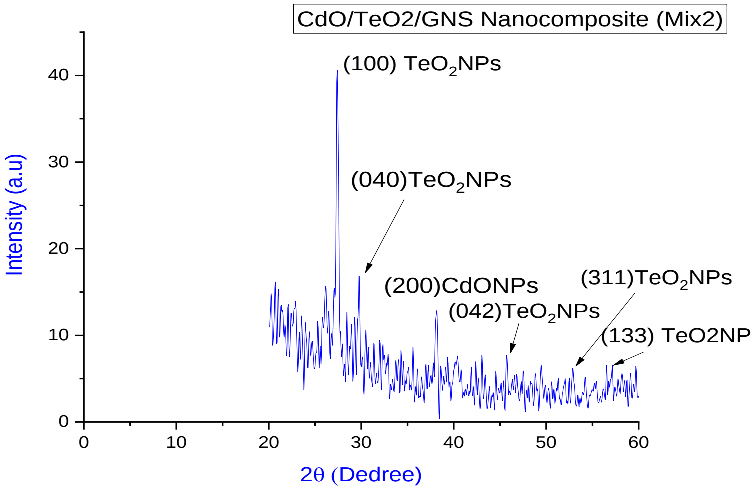

Figure (3-5): XRD of CdONPs / TeO_2NPs / GNS Nanocomposite (Mix 2) prepared by pulsed laser ablation (PLAL).

The Crystallite size of all prepared materials was calculated by using Debye-Scherer equation (2-2) as shown in Table (3-1).

Table (3-1): Crystallite size of CdONPs , TeO_2NPs , Mix1 and Mix2 Nanocomposite.

Structure	**2θ (Deg.)**	**FWHM(Deg.)**	**Crystallite Size(nm)**
TeO_2NPs	33.2	0.1082	73.4
CdONPs	32.5	0.2727	29.1
Mix1	highest peak of TeO_2NPs= 26.8	0.1106	71.8
	peak of CdONPs=33.1	0.11062	71.8
Mix2	highest peak of TeO_2NPs)=27.4	0.2669	29.7
	peak of CdONPs=38.1	0.2669	29.7

It is noticed from Table (3-1) that the crystallite size of TeO_2NPs decreases slightly in Mix 1, while the value of crystallite size of CdONPs increases from 29.1 to 71.8. For Mix 1, it is noticed that the crystallite size of TeO_2NPs decreases from 73.4 to 29.7, while the crystallite size of CdONPs increases slightly. The value of the crystallite size of TeO_2NPs and CdONPs in Mix1 and Mix2 are equal. From the results of XRD in general, it is noticed that there is a slight shift in the peaks before and after mixing, but there is a clear crystal growth of some peaks at the expense of the others after mixing, This is because the bonding process between Te and Cd element in the compound Mix1 and Mix 2 is an interstitud processes, and not a reciprocal process.

3-3 Filed Emission Scanning Electron Microscopy (FE-SEM) Analysis :

The surface morphology of graphene prepared from graphite in water using a pulsed laser is shown in Figure (3-6, a-d). It confirms that the prepared graphene has the Nanosheet shape (GNS), which is in agreement with what was obtained in reference[133].

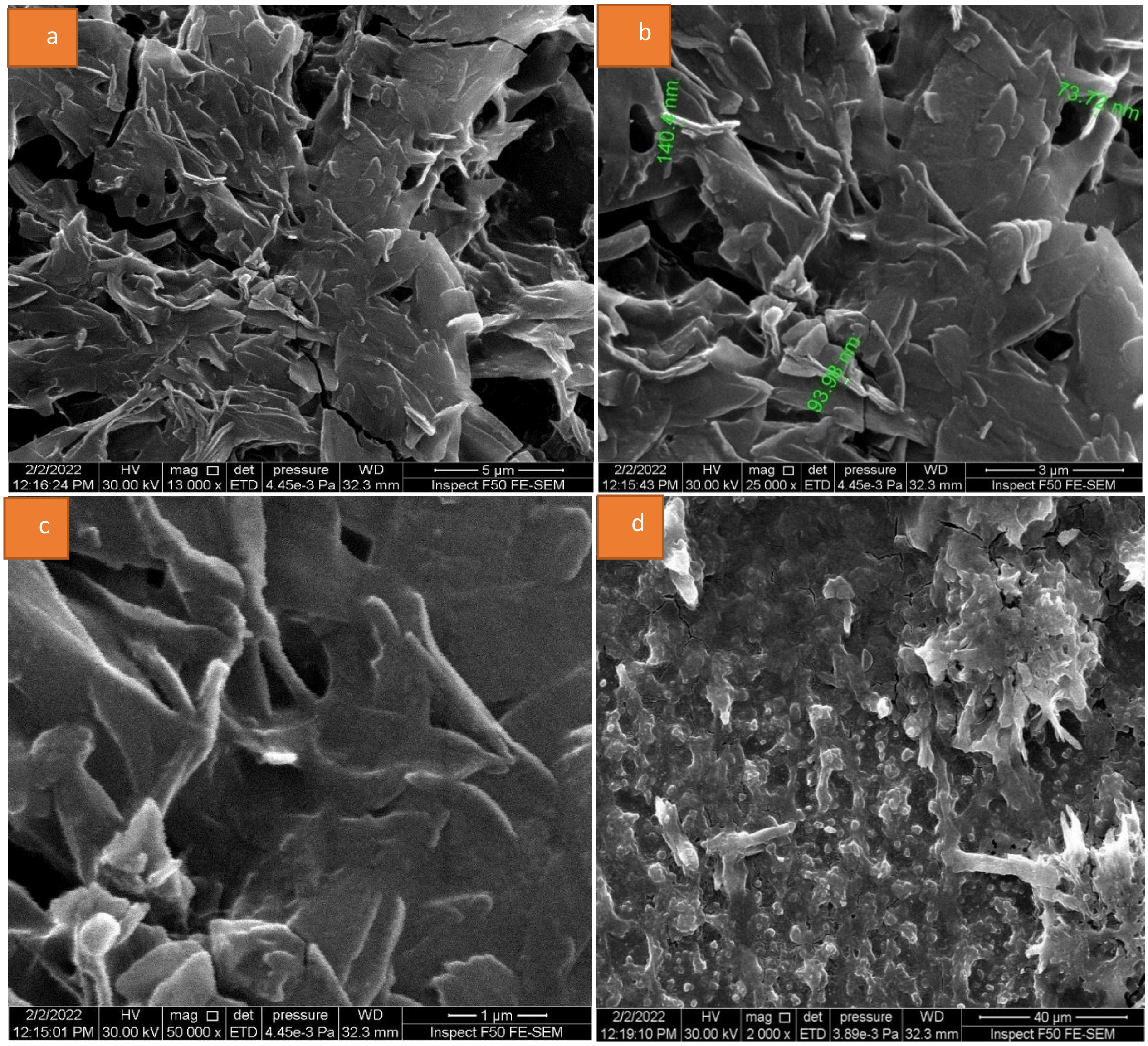

Figure (3-6): a- Field Emission Scanning Electron Microscopy of Graphene nanosheets (GNS)(5µm) b-Graphene (GNS)(3µm) c-Graphene(GNS)(1µm) d-Graphene(GNS)(40µm).

The prepared TeO_2NPs have a spherical shape of different sizes and some agglomerations are observed at various locations as shown in Figure (3-7, a-d).

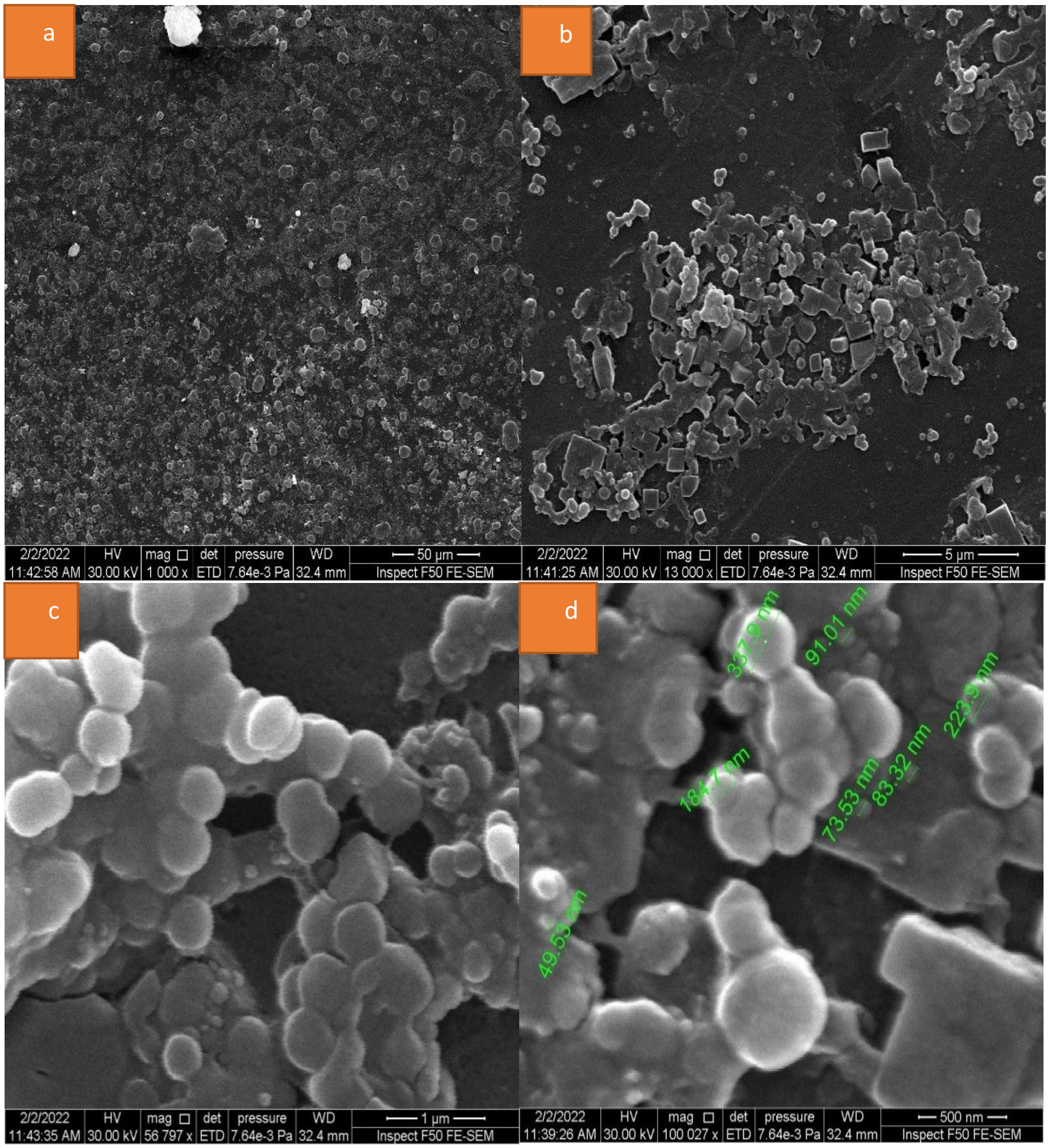

Figure (3-7): a-FE-SEM images of TeO_2NPs(50µm) b-TeO_2 (5µm) c- TeO_2 (1µm) d- TeO_2 (500nm) were prepared by pulsed laser ablation in distilled water .

Figure (3-8) shows the method for calculating the average particle size of TeO_2NPs by using image J program and is equal to 65 nm and it is similar to what was mentioned in the reference [134].

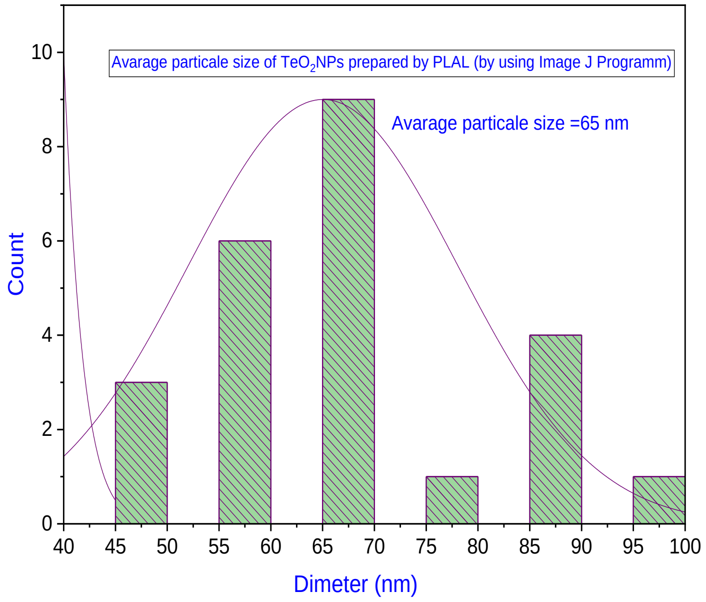

Figure (3-8): Size distribution of the TeO_2NPs.

Figure (3-9, a-d) shows the formation of CdONPs in irregular shapes and some of them are spherical in shape[135].

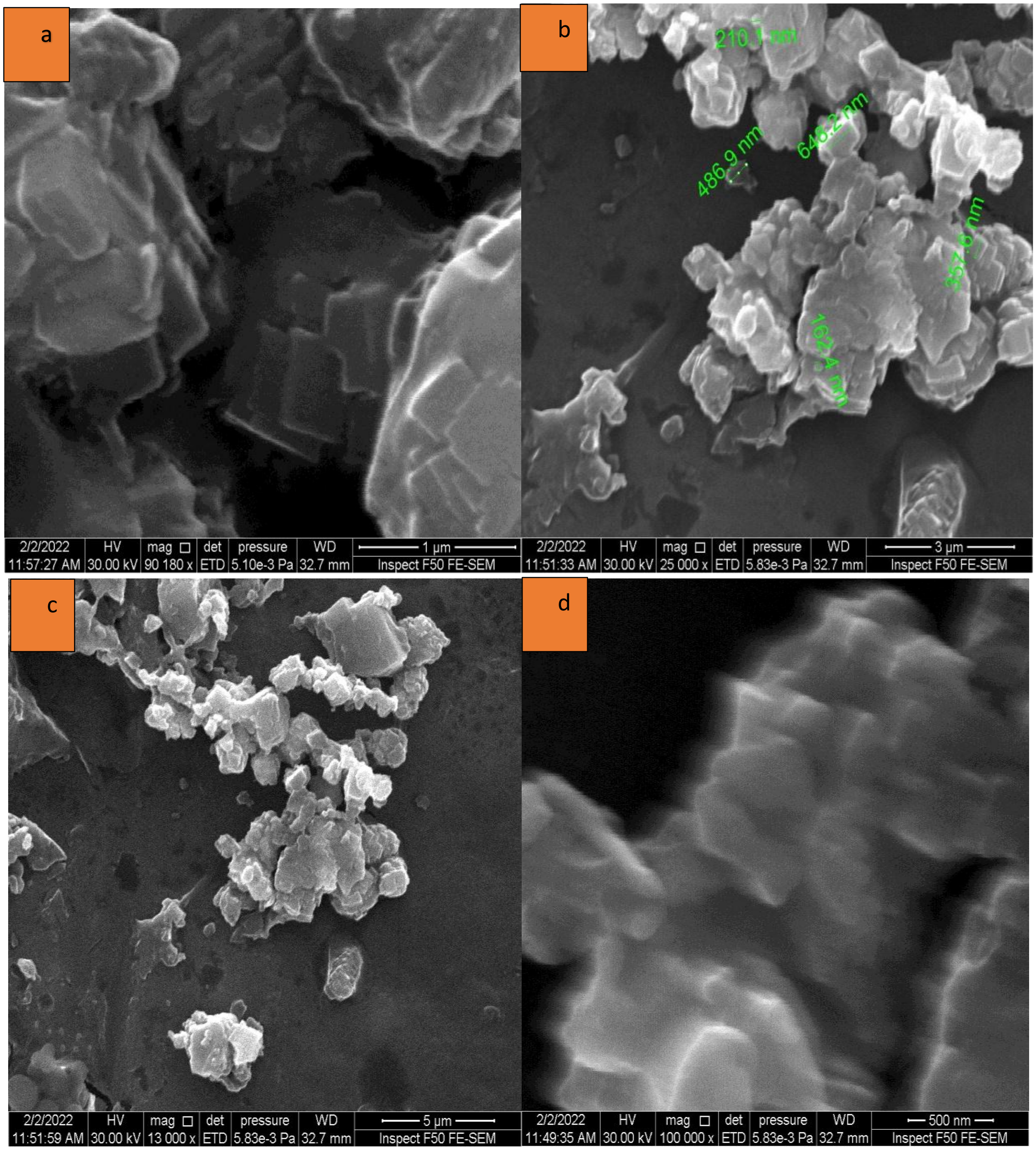

Figure(3-9): a-FE-SEM images of CdONPs(1µm) b-CdO(3µm) c-CdO(5µm) d-CdO(500nm) were prepared by pulsed laser ablation in distilled water .

Figure (3-10) shows the average particle size of CdONPs, which was 98.4 nm.

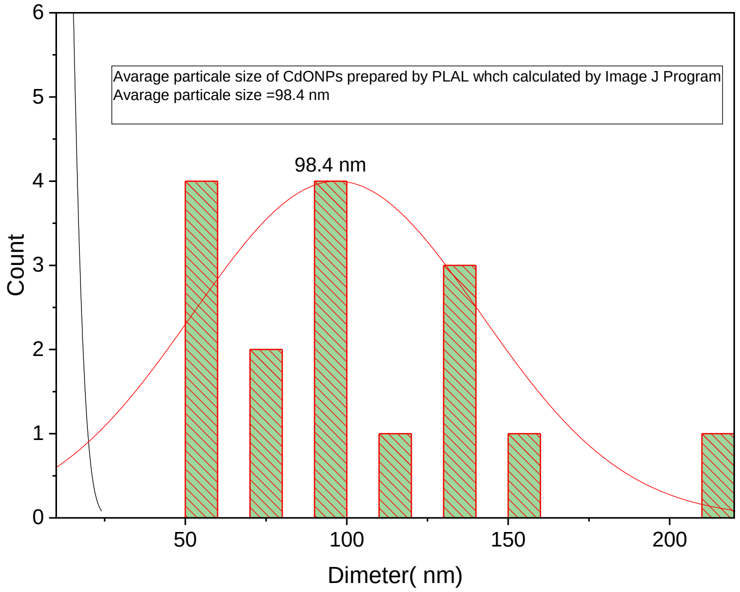

Figure (3-10): Size distribution of the CdONPs.

Figure (3-11) shows the formation of particles of different sizes, some of which are spherical, due to the formation of TeO_2NPs and CdONPs on the graphene nanosheet substrate which led to the formation of the TeO_2NPs/CdONPs/GNS nanocomposite (Mix 1).

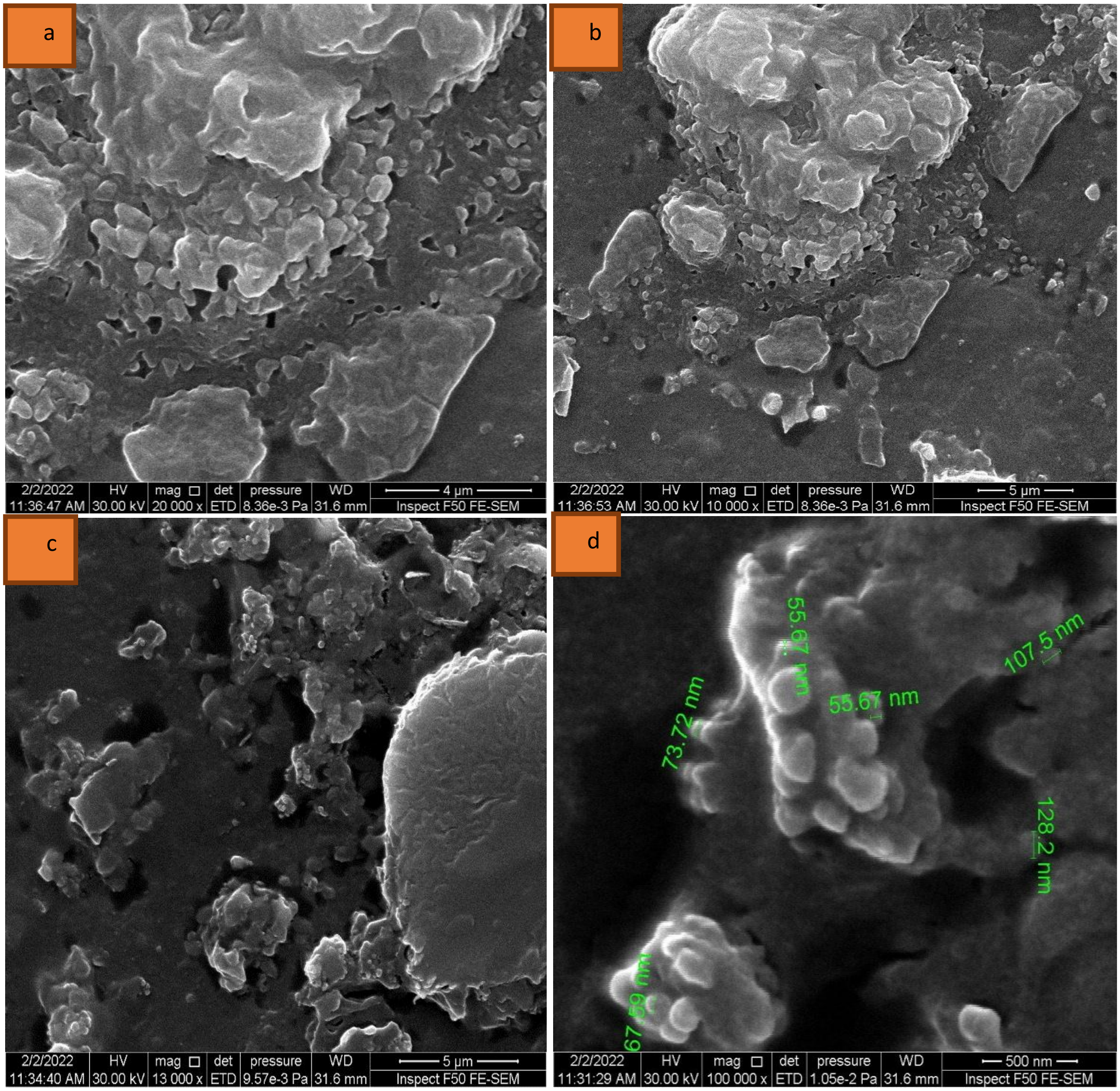

Figure(3-11): a- FE-SEM images of TeO2NPs/CdONPs/GNS (Mix 1)(4µm) b-Mix1(5µm) c-Mix1(3µm) d-Mix1(500nm) Nanocomposite were prepared by pulsed laser ablation in distilled water.

The average particle size of Mix1 is 78.9 nm as shown in the Figure (3-12).

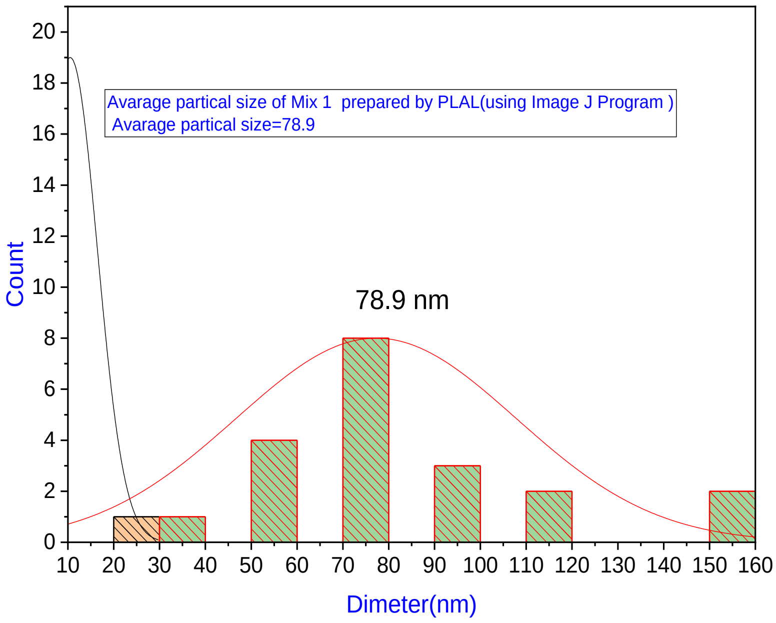

Figure (3-12): Size distribution of the Mix1 Nanocomposite.

Figure (3-13) shows the formation of cubic particles of different sizes due to the formation of CdONPs and TeO_2NPs on the graphene Nanosheet substrate which led to the formation of the TeO2NPs/CdONPs/GNS nanocomposite (Mix 2).

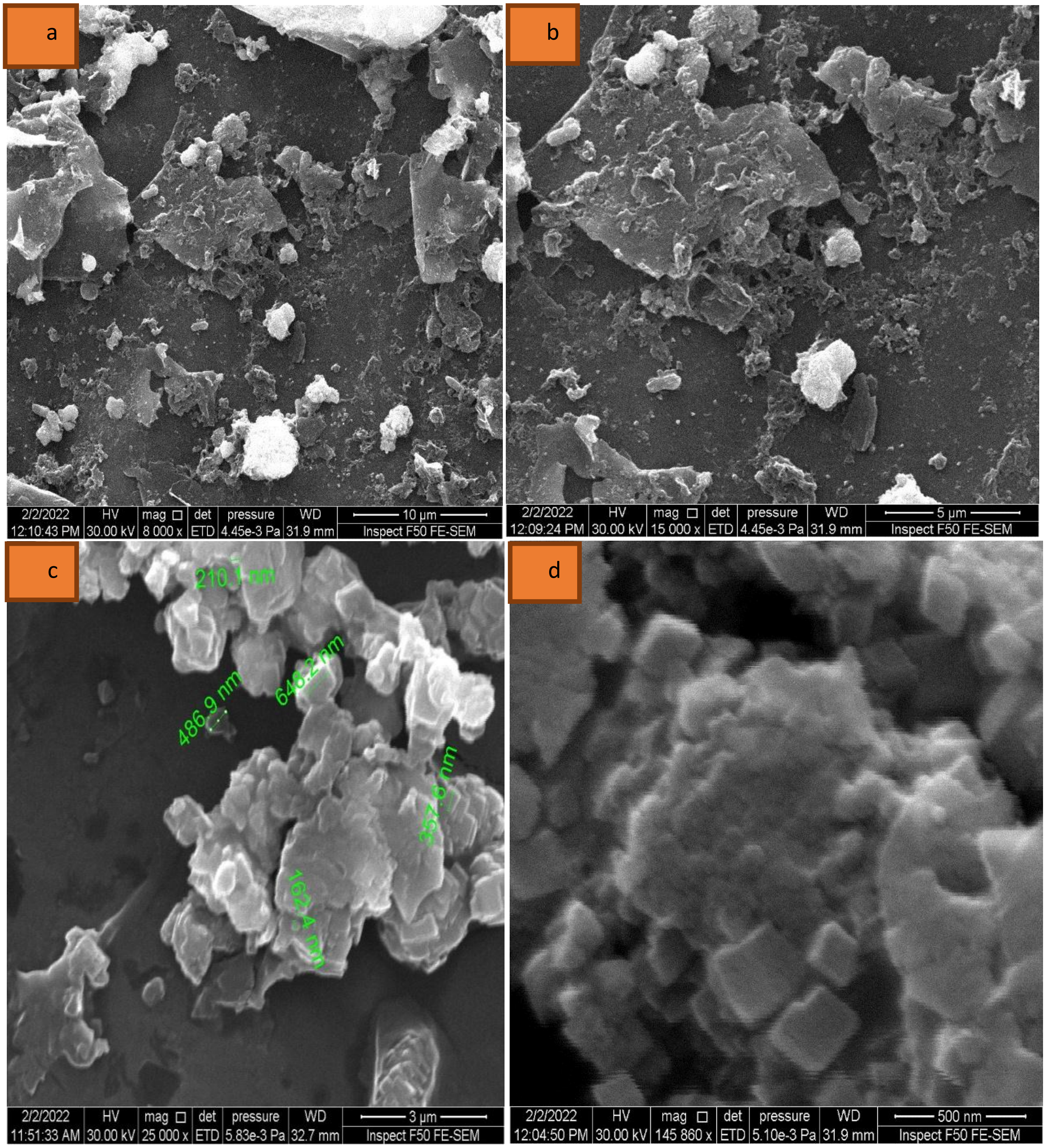

Figure(3-13): a- FE-SEM images of Mix2(10µm) b-Mix2(5µm) c-Mix2(3µm) d-Mix2(500nm) Nanocomposite were prepared by pulsed laser ablation in distilled water.

The average particle size of Mix 2 is 63.5 nm as shown in the Figure (3-14).

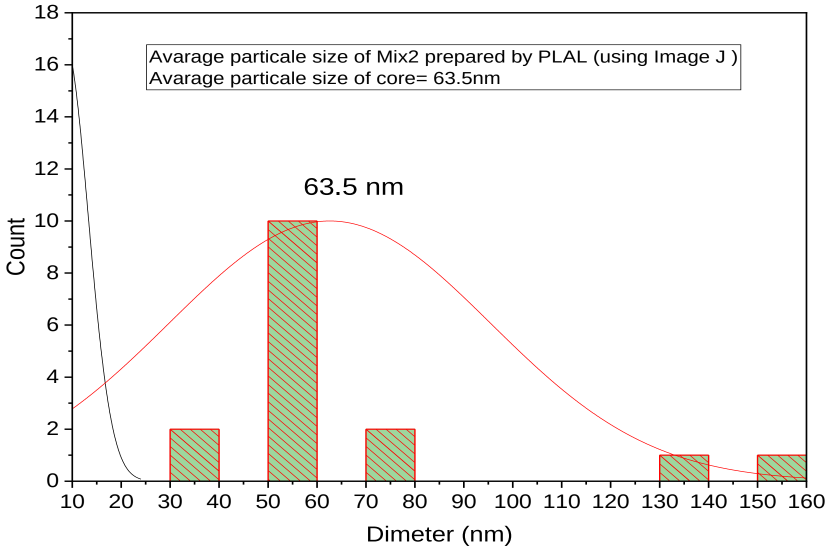

Figure (3-14): Size distribution of the Mix2 Nanocomposite.

3-4 Results of Fourier Transform Infrared Spectroscopy measurement (FTIR):

The FTIR spectrum of prepared GNS was illustrated in Figure (3-15). The appeared intense peaks at (3288.8cm^{-1}) were corresponding to stretching vibrations of hydroxyl (O-H) for water and its in agreement with the reference [104]. The peak at (1632.6 cm^{-1}) refer to C=C stretching vibrations bond (skeletal vibrations from unoxidized graphitic domains). Stretching vibration peaks of C–O (alkoxy) are observed at 1044.4 cm^{-1} and it’s close to the reference[136].

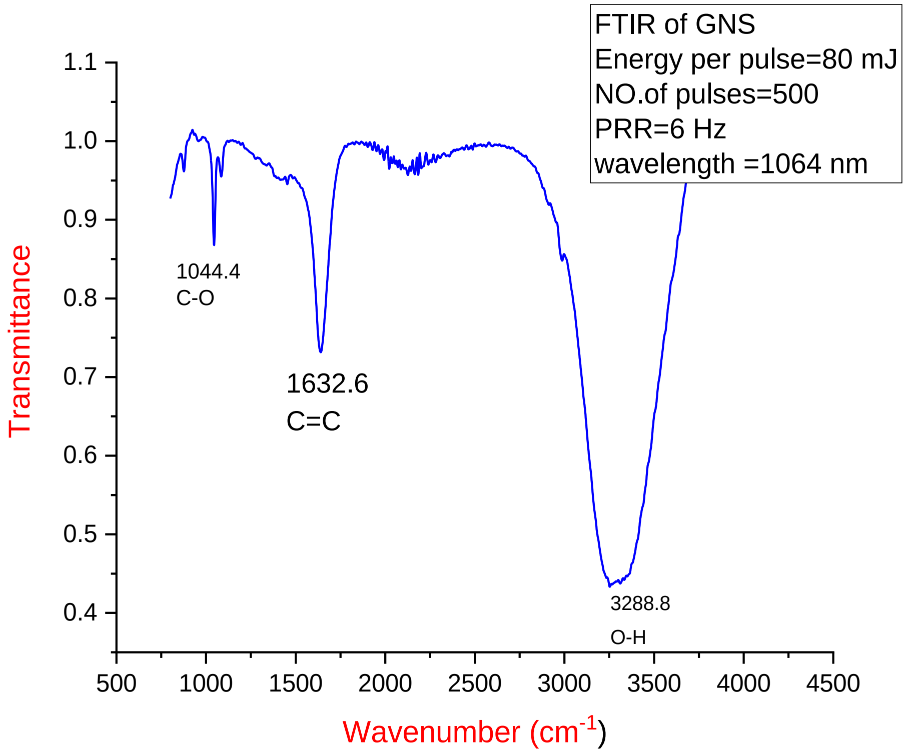

Figure (3-15): The FTIR spectrum of prepared GNS.

The FTIR spectrum of the TeO_2NPs is shown in Figure (3-16). The appeared intense peaks at 3288.8cm^{-1} were corresponding to stretching vibrations of hydroxy (O-H) for water. The peak at the range of (1642. 1cm^{-1}) refer to C=O stretching vibrations bond. Stretching vibration peaks of C–O (alkoxy) are observed at (1048.2 cm^{-1}). The band at (561.5cm^{-1}) is correspond to the Te-O stretching vibrations its close to the reference[137].

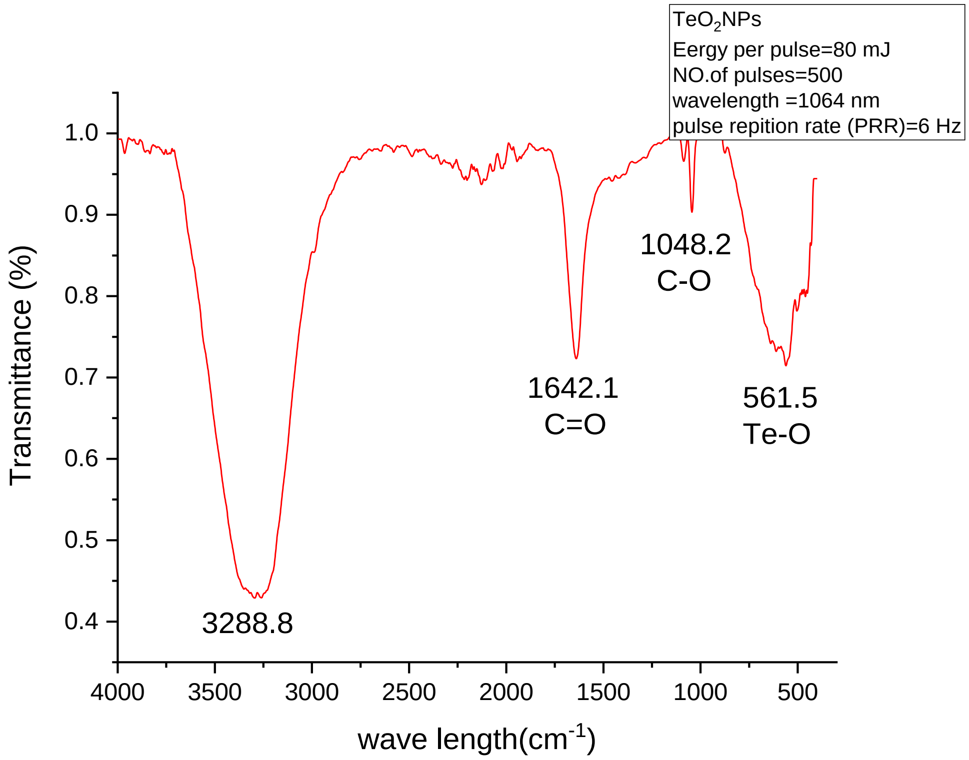

Figure (3-16): FTIR spectra of TeO_2NPs.

Figure (3-17) shows the absorption band of CdONPs prepared by pulsed laser. The stretching vibrations of the O-H group produce a large absorption band at 3286.7 cm^{-1} in the FT-IR spectrum. The stretching vibrations of the C–O (alkoxy bond) are responsible for the absorption bands at 1044cm^{-1}. The stretching vibrations of Cd–O are responsible for the absorption peak at 564.2 cm^{-1}. The existence of this band suggests that the CdO NPs were successfully manufactured [138].

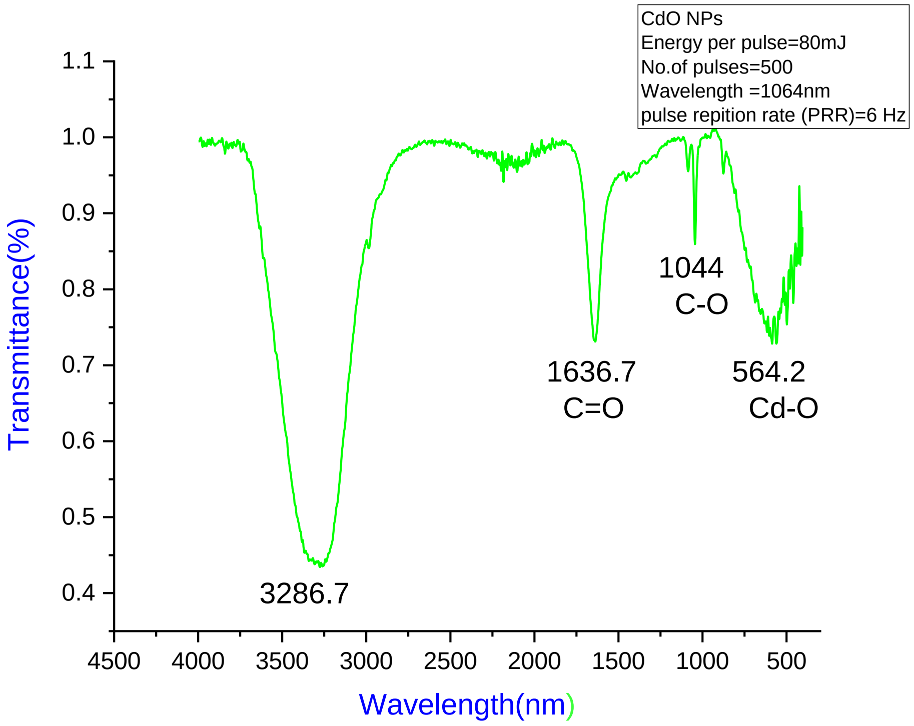

Figure (3-17): FTIR spectra of CdONPs.

Figures (3-18) and (3-19) show the absorption bands of the TeO_2NPs /CdONPs / GNS (Mix 1) and TeO_2NPs / CdONPs / GNS (Mix 2) nanocomposite respectively. The absorption peaks at 580.5 cm^{-1} and 588.2 cm^{-1} are due to the bonding of Cd-O with Te-O on the graphene sheet. As for the absorption peaks at 1044cm^{-1}, 1636.7cm^{-1} and 3286.7 cm^{-1}for both Mix1 and Mix 2 it is corresponding to C–O (alkoxy) stretching vibrations, C=C stretching vibrations bond and the stretching vibrations of the O-H group for water respectivelly.

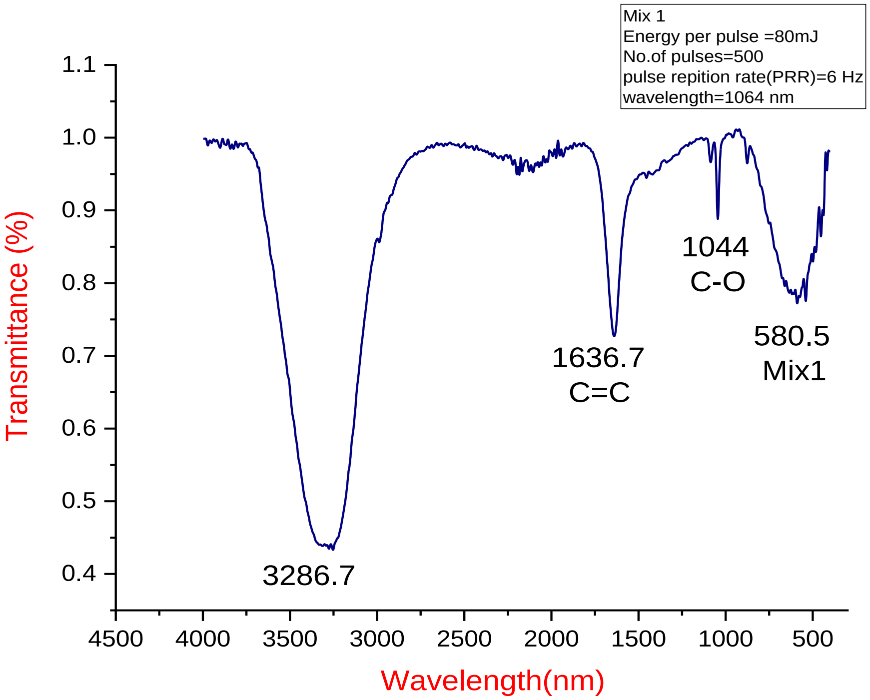

Figure (3-18): FTIR spectra of Mix 1.

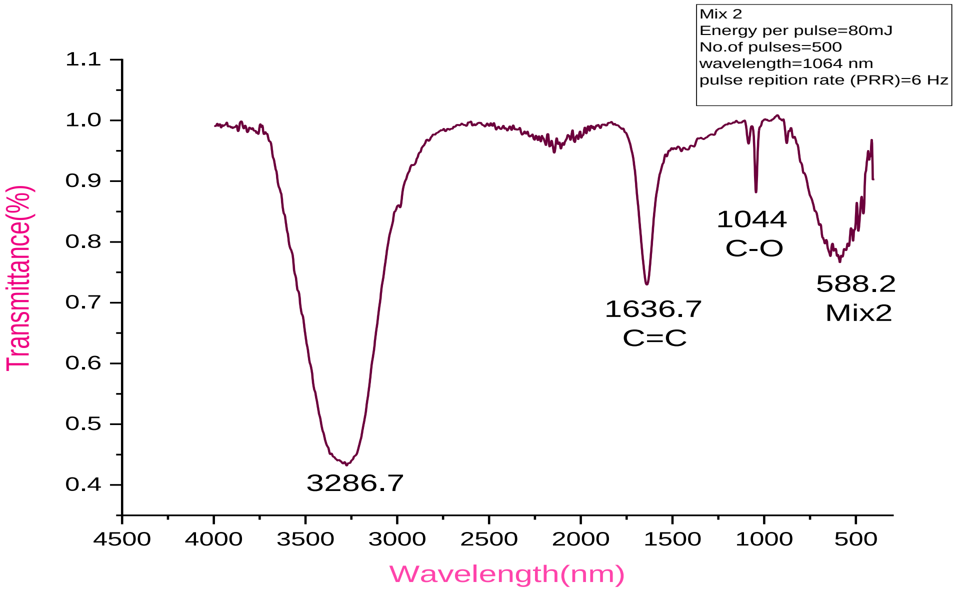

Figure (3-19): FTIR spectra of Mix 2.

3-5 UV-Visible Absorption Spectra:

The optical properties of all nanomaterials prepared by pulsed laser were studied using UV-visible absorption spectroscopy. Figure (3-20) shows the nano-suspension of all the materials used and the product of the fragmentation process using the pulsed laser.

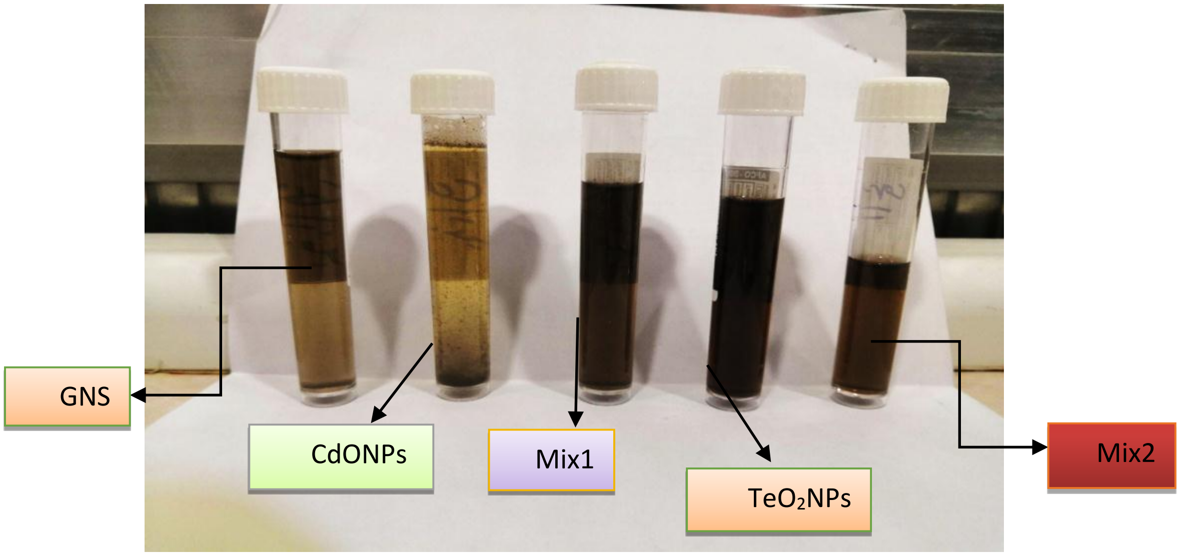

Figure (3-20) : Images of GNS, CdONPS, Mix1, TeO$_2$Nps and Mix2 respectively

Figure (3-21) of GNS shows the presence of an absorption peak at the wavelength of 265 nm, which is due to the π-π* electron transition. This transition indicates the presence of a C-C bond in the prepared nanosuspension, and these results are close to what was obtained in the sources[139].

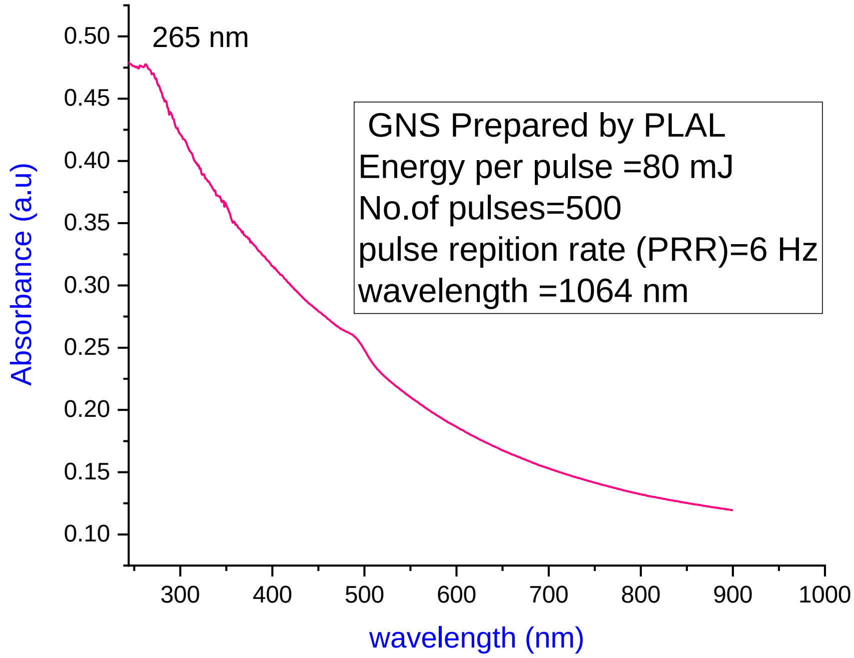

Figure (3-21): The absorption peak of GNS.

Figure (3-22) depicts the absorption peak at 292 nm associated with the formation of TeO_2NPs. This absorption peak resulted from the progressive weakening of the valence band (p-bonding triplet) to the conduction band (p-antibonding triplet) during the oxidation of Te into TeO_2 in water, and it is similar to what is described in the reference[140]. It is noted that a blue shift occurs compared to Te bulk (E_g=0.35 eV) due to the occurrence of the quantum confinement phenomenon resulting from the effect of the pulsed laser.

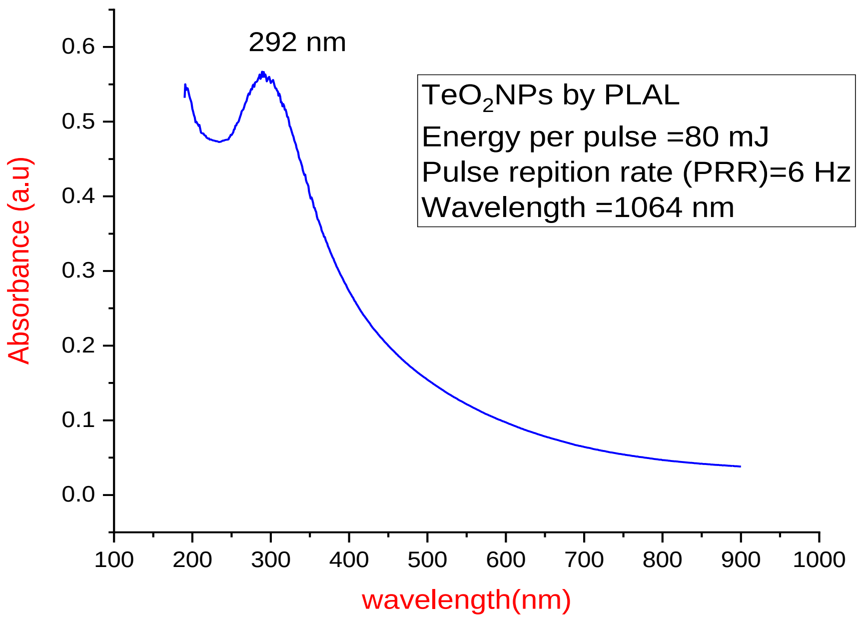

Figure (3-22): The absorption peak of TeO_2NPs.

It can be seen that CdO nanoparticles show absorption in the range 250-500 nm. The onset of absorption is at 285 nm, which clearly indicate formation of CdONPs. UV-vis spectra show that CdONPs exhibit a blue shift in comparison with that of the bulk Cd element due to the occurrence of the quantum confinement phenomenon resulting from the effect of the pulsed laser[141] as shown in the Figure (3-23).

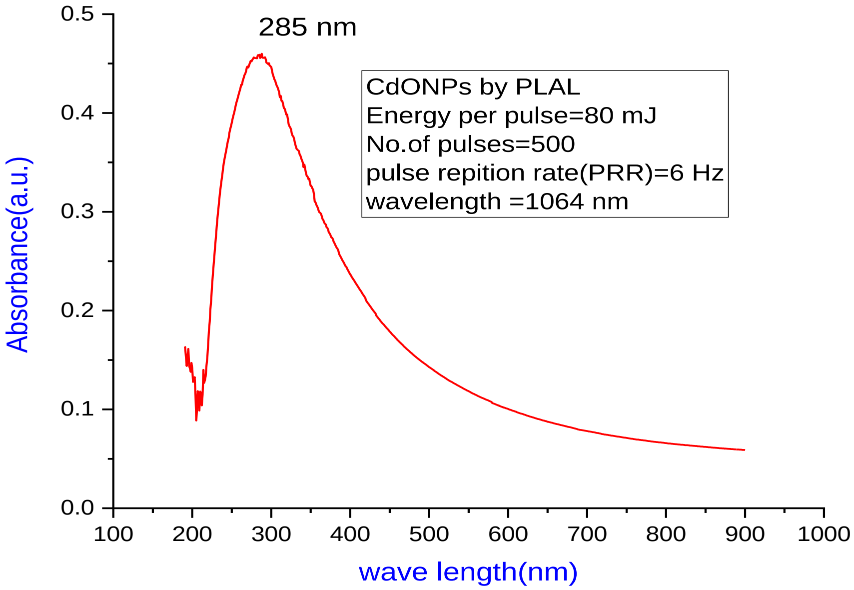

Figure (3-23): The absorption spectrum of CdONPs.

Figure (3-24) and (3-25) illustrates obtaining a new absorption peak at 274.5 nm and 277.3 nm for each mix 1 and mix 2, respectively. The new peak has a red shift compared to GNS and a blue shift compared to TeO_2NPs and CdONPs due to quantum confinement phenomenon resulting from the effect of the pulsed laser. This new peaks indicates the formation of TeO_2NPs /CdONPs /GNS (Mix 1) and TeO_2NPs /CdONPs /GNS (Mix 2) nanocomposite respectively.

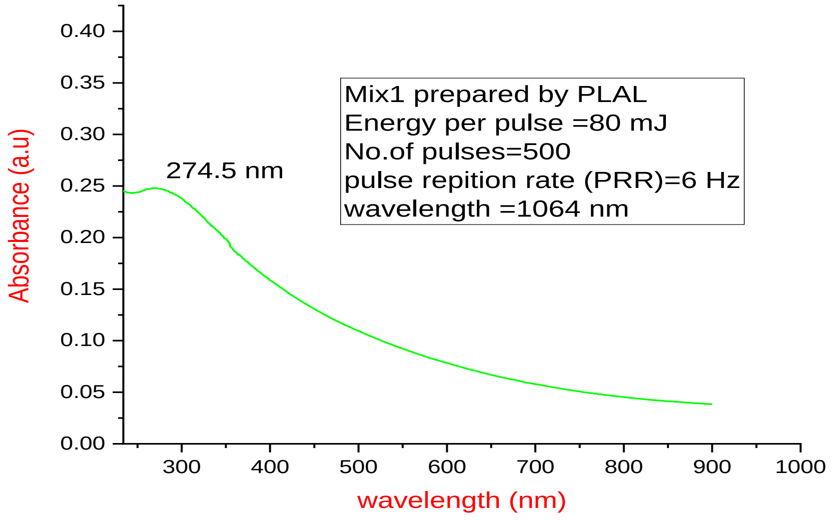

Figure (3-24): The absorption spectrum of Mix 1.

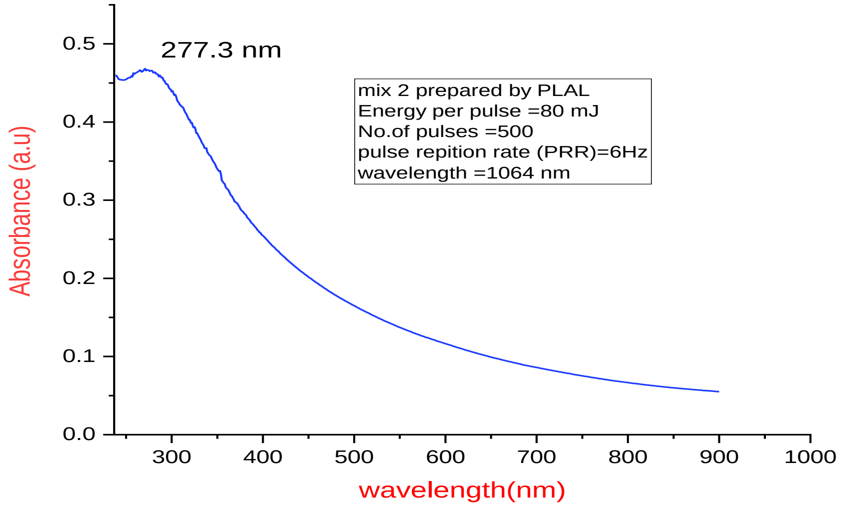

Figure (3-25): The absorption spectrum of Mix 2.

Table (3-2) shows that the energy gap for all samples increased due to the small size of the nanoparticles compared to the bulk materials due to the occurrence of quantum confinement.

Table (3-2): The energy gaps for all samples

Samples	**Absorption Peaks(nm)**	**Absorption Intensity *(a.u.)***	**Energy Gap(eV)**
TeO_2NPs	**292**	**0.564**	**1.40**
CdONPs	**285**	**0.457**	**1.54**
Mix1	**274.5**	**0.245**	**2.20**
Mix2	**277.3**	**0.465**	**3.25**

The energy gap for TeO_2NPs, CdONPs, mix1 and mix2 was calculated using the tauc plot and its values were 1.4 , 1.54, 2.2 and 3.25 eV respectively, as shown in Figure (3-26).

The energy gap for TeO$_2$NPs	The energy gap for CdONPs ,
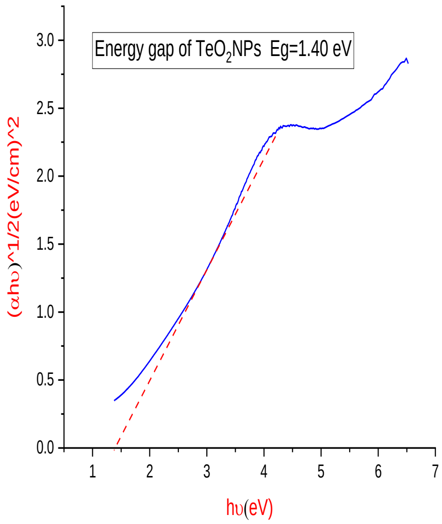	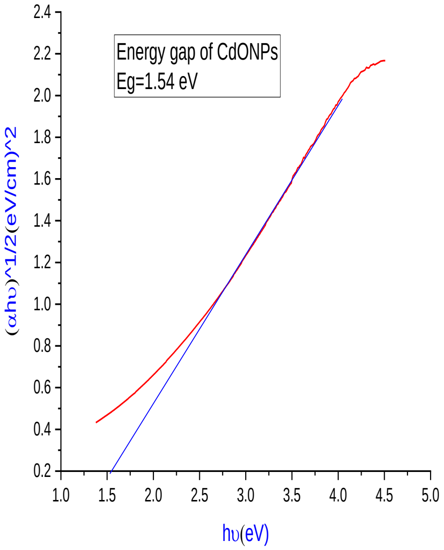
The energy gap for Mix 1	The energy gap for Mix2
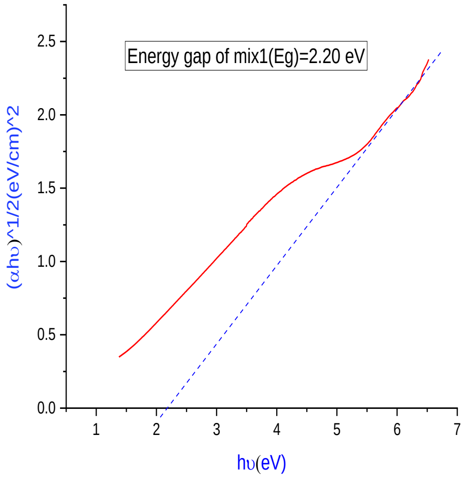	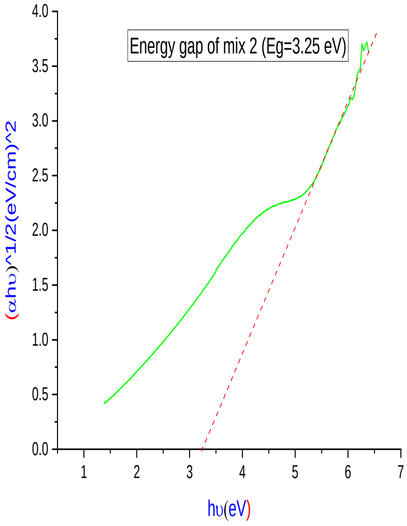

Figure (3-26, a-d): The Energy band gab of (a- TeO$_2$NPs, b-CdONPs, c-mix1 , d-mix2).

3-6 Calculation of the adsorption efficiency of the prepared materials:

The prepared graphene using pulsed laser has a high efficiency in adsorption of methyl blue dye compared with other prepared nanomaterials as in Figure (3-27), where the value of the adsorption efficiency can be calculated by using equation:

$$\text{Removal efficiency \%} = \frac{A^{\circ} - A^{t}}{A^{\circ}} \times 100 \qquad \text{….. …..} \ (3-1)$$

A^0 :intensity of pure MB at t=0

A^t :intensity of MB + GNS at time (t)

And its reached to 65.3% and 68.7% for t = 5 s and t = 15 s, respectively.

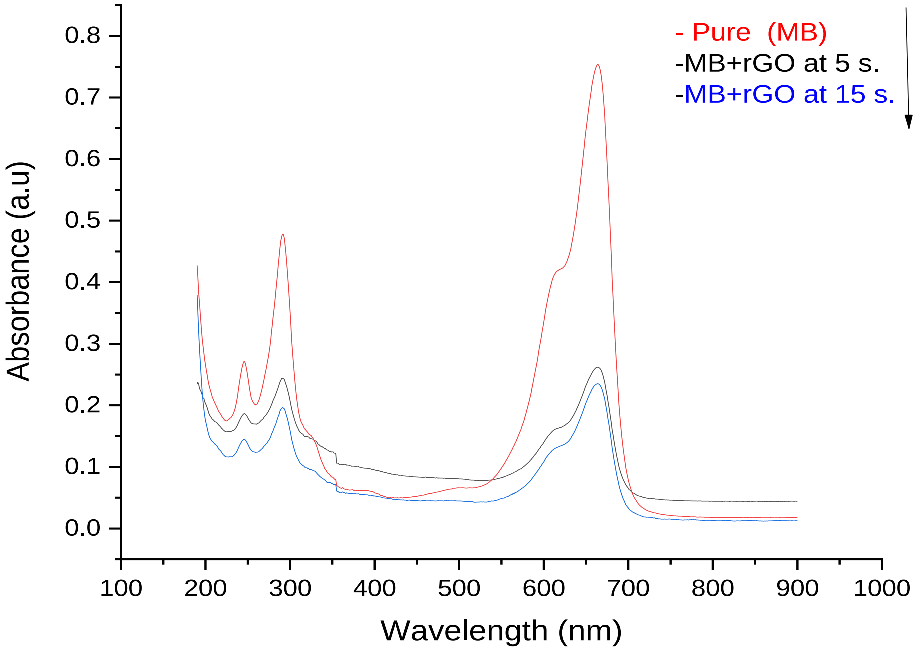

Figure (3-27) : UV – Vis spectrum of pure MB Dye and GNS+MB mixture to remove methyl blue (MB).

Figure (3-28) illustrates the calculation of the adsorption efficiency of all materials prepared by pulsed laser. In general, it is noted that the longer the time, the greater the absorbance intensity excepted GNS+MB+5 and GNS+MB+15 s. This result indicates that it is not possible to use TeO_2NPs, CdONPs, Mix1 and Mix 2 to remove methyl blue (MB) but this can be used in the manufacture of the solar cell because it enhances the absorption in the visible range.

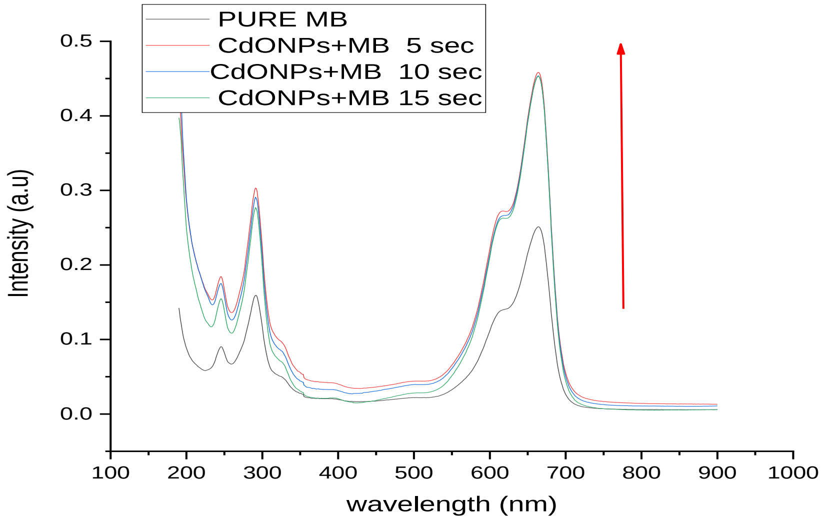

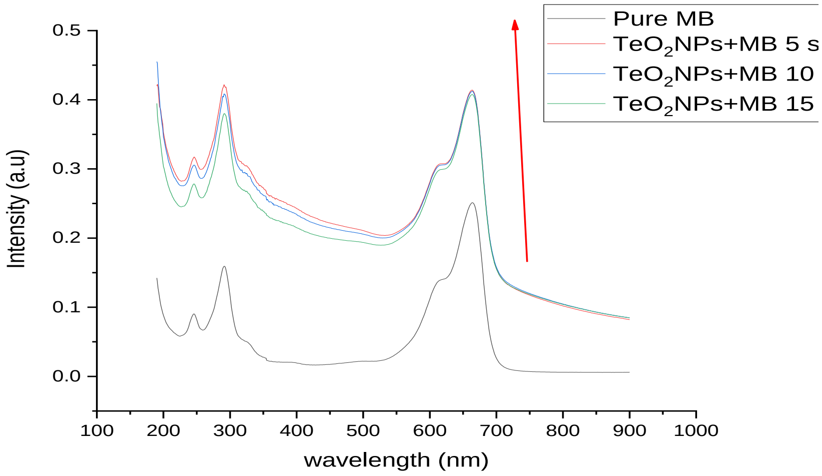

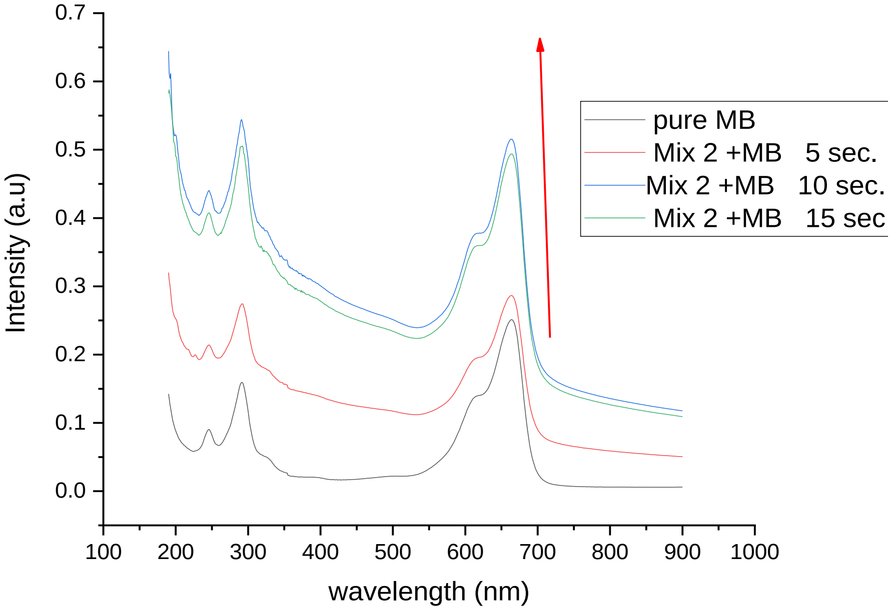

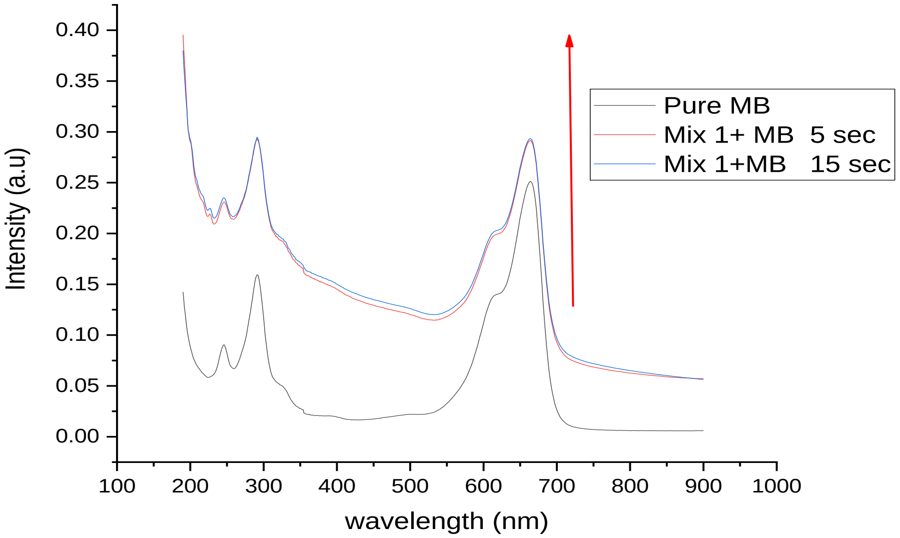

Figure (3-28): UV – Vis spectrum of pure MB Dye, GNS+MB mixture, CdO, TeO_2, Mix1 and Mix2 to remove methyl blue (MB) excepted GNS+MB+5 and GNS+MB+15 s .

3.7 Effect of nanoparticles on bacteria

Four types of bacteria were used to evaluate the effect of the five types of nanoparticles. The bacteria used were staphylococcus aureus, pseudomonas aeruginosa, Escherichia coli, and enterococcus faecalis. As shown in the table, GNS and Mix1 NPs affects the growth of *S. aureus*, while Te and Mix2 affect the growth of *E.coli*, *P.aerugenosa* and *E.faecalis* did not affect by any type of these nanoparticles.

Antibacterial activity of Tellurium is well known for decades. It has been shown that it cause ROS generation , damage the metabolic enzymes, induce glutathione depletion and lipid peroxidation. Te is known to affect gram negative bacteria more than gram positive bacteria due to their Te susceptibility. *E.coli* showed more sensitivity than P.aerugenosa because the later have a known high antimicrobial resistance level[142]. The current works result agrees with Cailing et al results in that TeO_2NPs affect *E.coli* but not *P.aerugenosa* nor *S. aureus* bacteria[143].

Table (3-3): Bacterial growth inhibition zones diameters (mm) caused by the nanoparticles

Bacteria / Nanoparticle types	Inhibition zone diameter (mm)				
	CdONPs	TeO2	GNS	Mix1	Mix2
S. aureus	-	-	22	20	-
P.aerugenosa	-	-	-	-	-
E.coli	-	22	-	-	18
E.faecalis	-	-	-	-	-

Figure (3-29): Well diffusion method for determination of nanoparticle cytotoxicity on bacterial strains. NP effect is measured by measuring the inhibition zone diameter

CdONPs have no effect against all bacterial strains used. This may be related to the particle size and/or concentration used. Studies on CdO NPs with smaller size (30 nm) showed strong antibacterial effect against gram negative and positive bacteria [144]. Nanoforms also affect their activity, thus, CdONPs micelles have potential antibacterial activity particularly, at concentrations above 1% of total liquid culture media[145].

The effects of Mix1 and Mix2 are not fully understood since the two composites contain more than one cytotoxic element. It is believed that part of the cytotoxicity arises from released Cd, which is a toxic metal ion. Cd ions interfere with DNA repair, substitute the physiologic Zn, and induce reactive oxygen species (ROS)[146].

Despite the similar composition of various carbon NPs, they have distinct physical and biological properties depending on their structure. Graphite NP is capable of inducing apoptosis and cell death or inflammatory responses or could inhibit angiogenesis. Different C-atoms hybridization of carbon forms thus, exhibit distinct physical and electrochemical properties. This could explain their differential effects exerted on human cells[147].

3-8 Effect of nanoparticles on normal and cancer cells:

In order to explore the cytotoxicity of NPs on eukaryotic cells, normal and cancer cells were used. Vero cells is a standard normal cell line used worldwide to evaluate the cytotoxicity of drugs, chemicals, and nanoparticles. LNCap cell line is a prostate cancer cells, used in this study to Figure out the effect of these NPs on cancer cell. As shown in Figures (3-30) and (3-31), Te and Cd were the most effective and cytotoxic NPs on both normal and cancer cells. GNS NP was cytotoxic for cancer cells more than normal cells, this feature may indicate that this type of NP may have anticancer activity. These results agree with the documented results by [148].

TeO_2NPs showed strong cytotoxicity against mammalian cells, this effect agrees with a previous study by Diana [149], who treated normal and cancer human cells with smaller size (10 nm), green synthesized TeO_2NPs. They found that TeO_2NPs strongly inhibited human cells at concentrations between (25-100 µg/ml).

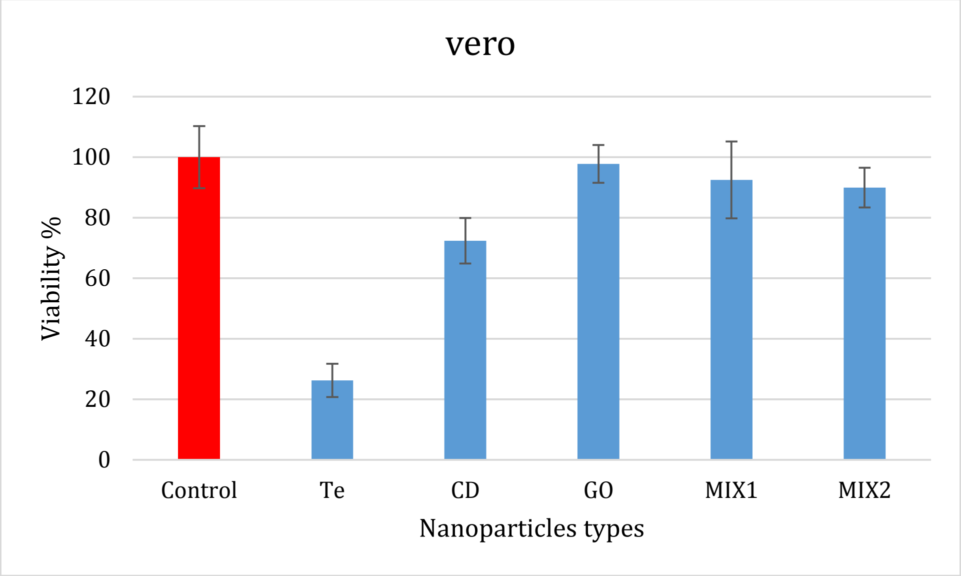

Figure (3-30): Effect of nanoparticles on normal cells

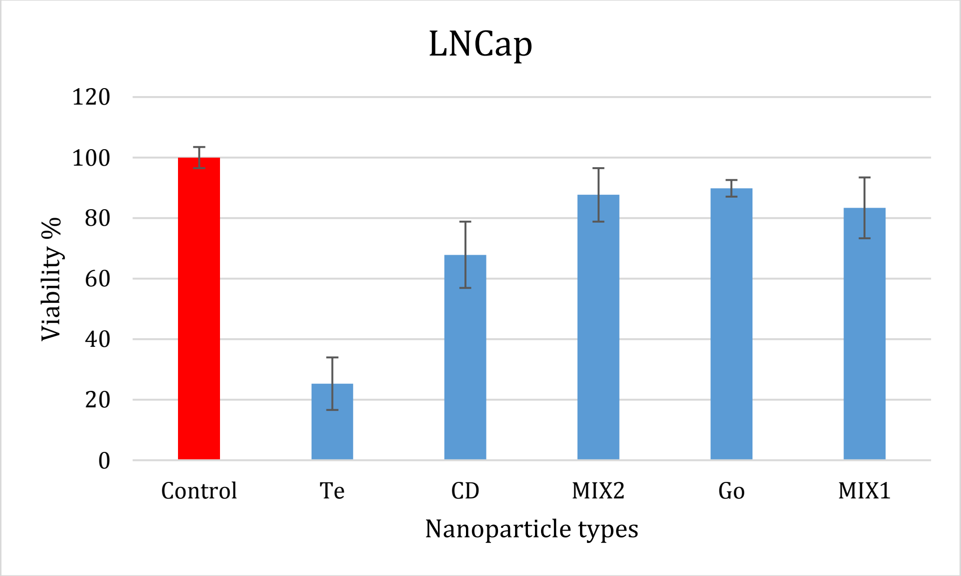

Figure (3-31): Effect of nanoparticles on prostate cancer cells

Future works:

1- Synthesis of CdONPs/TeO_2NPs/CdS Nanocomposite by hydrothermal Technique for Photovoltaic Applications .

2- Syntheses and Spectroscopic Study of TeO_2NPs / CdONPs / ZnONPs nanocomposite for gas sensor application .

3- Study of structural and optical properties of TeO_2NPs / TiO_2NPs / graphene nanocomposite for gas sensor application.

4- Study of linear and nonlinear optical properties of TeO_2NPs /graphene/polymer nanocomposite.

5- Investigate the possible biological applications using different sizes, concentrations, and composition of TeO_2NPs, CdONPs and GNS, particularly their antibacterial and anticancer potential.

Conclusions:

1- The pulsed laser ablation method is an easy, cheap, environmentally friendly, and successful method for preparing TeO_2NPs, CdONPs, GNS, TeO_2NPs/CdONPs/GNS (Mix 1), and TeO_2NPs/CdONPs/GNS (Mix 2).

2- All materials prepared by the pulsed laser ablation method have a crystalline structure, according to XRD results.

3- According to XRD results, there is a slight shift in the peaks before and after mixing, but there is a clear crystal growth (orientation) of some peaks of CdONPs after mixing (Mix 1). This is because the bonding process between Te and the Cd element in the compounds mix1 and mix2 is an interstitial process, and not a reciprocal process. We conclude that the mixing process did not effect on the crytal structure of CdO,TeO_2 and GNS, but it worked on the growth of peaks with in Mix1 and Mix2 .

4- From the results of UV-visible spectroscopy for both Mix 1 and Mix 2, it is clear that there were new absorption peaks at 274.5 nm and 277.3 nm, respectively. The new peak has a red shift compared to GNS and a blue shift compared to TeO_2NPs and CdONPs due to the quantum confinement phenomenon resulting from the pulsed laser.

5- The parameters of the pulsed laser used in this study can convert graphite to graphene, as apparent from UV-visible spectroscopy and XRD measurements.

6- The energy gap for all samples is increased due to the small size of the nanoparticles compared to the bulk materials due to the occurrence of quantum confinement. When comparing mix1 and mix2 with TeO_2NPs and CdONPs, we notice that the energy gap is increasing in the mixture as a result of the small size of nanoparticles due to the phenomenon of quantum confinement resulting from the effect of pulsed laser energy.

7- The method of preparing Mix 1 and Mix 2 samples has a clear role in controlling the size of nanoparticles.

8- The prepared graphene nanosheets (GNS) using pulsed laser have high efficiency in adsorption of methyl blue dye (the environmental application) compared with other prepared nanomaterials and the adsorption efficiency at a time of 15 seconds is higher than that of 5 seconds. While TeO_2NPs, CdONPs, Mix 1, and Mix2 cannot be used to remove methyl blue (MB) but this can be used in the manufacture of the solar cell because it enhances the absorption in the visible range.

9- The prepared nanoparticles have different and selective antibacterial activities that need more attention and more investigation.

10- TeO_2 NPs and CdONPs nanoparticles possess strong cellular toxicity for normal and cancer cells, GNS NP was cytotoxic for cancer cells more than normal cells

References

[1] A. S. Khan, "Application of Simulation for Emulating Nanotechnology and Emerging Technologies in Education," *Nanotechnology: Ethical and Social Implications*, p. 313, 2012.

[2] W. Luther, R. Nass, F. Schuster, M. Kallio, and P. Lintunen, "Industrial application of nanomaterials-changes and risks: Technology analysis," 2004.

[3] D.-I. C. Cimpean, *Development of Silicon Nanoparticles with Tailored Surface Properties*. Friedrich-Alexander-Universitaet Erlangen-Nuernberg (Germany), 2008.

[4] S. Bagheri, K. Chandrappa, and S. Hamid, "Facile synthesis of nano-sized ZnO by direct precipitation method," *Der Pharma Chemica,* vol. 5, no. 3, pp. 265-270, 2013.

[5] Wasan, R. Saleh, M. Saeed Nada, A. Twej Wesam, and Alwan Mohammed. "Synthesis sol-gel derived highly transparent ZnO thin films for optoelectronic applications." Advances in Materials physics and chemistry 2012 (2012).

[6] F. Ahmed, S. Kumar, N. Arshi, M. Anwar, B. H. Koo, and C. G. Lee, "Structural and magnetic study of Co-doped ZnO nanoparticles synthesized by auto combustion method," *International Journal of Nanoscience*, vol. 10, no. 04n05, pp. 1025-1028, 2011.

[7] R. Rani and S. Sharma, "Preparation and characterization of SnO 2 nanofibers via electrospinning," *Advances in Nanoparticles,* vol. 5, no. 01, p. 53, 2016.

[8] K. Okazaki, K. Kubo, T. Shimogaki, D. Nakamura, M. Higashihata, and T. Okada, "Lasing characteristics of ZnO nanosheet excited by ultraviolet laser beam," *Adv. Mat. Lett,* vol. 2, no. 5, pp. 354-357, 2011.

[9] R. Seoudi and F. Al-Marhaby, "Synthesis, characterization and photocatalytic application of different sizes of gold nanoparticles on 4-nitrophenol," *World Journal of Nano Science and Engineering*, vol. 6, no. 03, p. 120, 2016.

References

[10] Z. G. Zheng, Y. Q. Lu, and Q. Li, "Photoprogrammable mesogenic soft helical architectures: a promising avenue toward future chiro‐ optics," *Advanced Materials,* vol. 32, no. 41, p. 1905318, 2020.

[11] A. Mahapatra, "Fabrication and characterization of novel iron oxide/alumina nanomaterials for environmental applications," 2013.

[12] D. Bera, L. Qian, T.-K. Tseng, and P. H. Holloway, "Quantum dots and their multimodal applications: a review," *Materials,* vol. 3, no. 4, pp. 2260-2345, 2010.

[13] U. Woggon, *Optical properties of semiconductor quantum dots*. Springer, 1997.

[14] M. U. Chupel *et al.*, "Exercise and taurine in inflammation, cognition, and peripheral markers of blood-brain barrier integrity in older women," *Applied Physiology, Nutrition, and Metabolism,* vol. 43, no. 7, pp. 733-741, 2018.

[15] F. Sarjani, Y. Yohandri, and Z. Kamus, "Fabrication of digital parabolic motion experiments set based on the ATMEGA328 microcontroller to measure motion parameters," *PILLAR OF PHYSICS,* vol. 10, no. 1, 2017.

[16] D. Beckel *et al.*, "Thin films for micro solid oxide fuel cells," *Journal of Power Sources,* vol. 173, no. 1, pp. 325-345, 2007.

[17] Manceriu, Laura Maria, Aline Rougier, and Anca Duta. "Comparative investigation of the Ti and Mo additives influence on the opto-electronic properties of the spray deposited WO3 thin films." Journal of Alloys and Compounds 630 (2015): 133-145.

[18] E. Kärber et al., "Photoluminescence of spray pyrolysis deposited ZnO nanorods," *Nanoscale research letters,* vol. 6, no. 1, pp. 1-7, 2011.

[19] H. Sun, J. Huang, H. Wang, and J. Zhang, "CO2 Reforming of CH4 over Xerogel Ni− Ti and Ni− Ti− Al Catalysts," *Industrial & engineering chemistry research,* vol. 46, no. 13, pp. 4444-4450, 2007.

References

[20] Y. Gogotsi, *Nanomaterials handbook*. CRC press, 2006.

[21] B. Ben-Nissan, A. H. Choi, I. J. Macha, and S. Cazalbou, "Sol-gel nanocoatings of bioceramics," *Handbook of Bioceramics and Biocomposites*, 2016.

[22] Machui, Florian. Formulation of Semiconductor Solutions for Organic Photovoltaic Devices. Friedrich-Alexander-Universitaet Erlangen-Nuernberg (Germany), 2014.

[23] J. Xue, Z. Tong, Y. Ma, M. Wang, S. Jia, and X. Chen, "Fabrication of volume scattering diffusers by spin-coating SiO 2 microspheres and SU-8 photoresist for speckle reduction investigation," *Optical Materials Express,* vol. 12, no. 2, pp. 479-488, 2022.

[24] Chawarambwa, Fadzai Lesley, Tika Erna Putri, Pankaj Attri, Kunihiro Kamataki, Naho Itagaki, Kazunori Koga, and Masaharu Shiratani. "The Effects of Spin-Coating Rate on Surface Roughness, Thickness, and Electrochemical Properties of a Pt Polymer Counter Electrode." In Advanced Engineering Forum, vol. 45, pp. 1-13. Trans Tech Publications Ltd, 2022.

[25] K. Byrappa and T. Adschiri, "Hydrothermal technology for nanotechnology," *Progress in crystal growth and characterization of materials,* vol. 53, no. 2, pp. 117-166, 2007.

[26] R. Swarnkar, S. Singh, and R. Gopal, "Effect of aging on copper nanoparticles synthesized by pulsed laser ablation in water: structural and optical characterizations," *Bulletin of Materials Science,* vol. 34, no. 7, pp. 1363-1369, 2011.

[27] Yang, Li. "Self-assembly and ordering nanomaterials by liquid-phase pulsed laser ablation." PhD diss., University of Bristol, 2007.

[28] V. Amendola and M. Meneghetti, "What controls the composition and the structure of nanomaterials generated by laser ablation in liquid solution?," *Physical Chemistry Chemical Physics,* vol. 15, no. 9, pp. 3027-3046, 2013.

[29] S. Ibrahimkutty *et al.*, "A hierarchical view on material formation during pulsed-laser synthesis of nanoparticles in liquid," *Scientific reports,* vol. 5, no. 1, pp. 1-11, 2015.

[30] B. Naik, V. Prasad, and N. N. Ghosh, "A simple aqueous solution based chemical methodology for synthesis of Ag nanoparticles dispersed on mesoporous silicate matrix," *Powder technology,* vol. 199, no. 2, pp. 197-201, 2010.

[31] T. Suemoto *et al.*, "Soft X-ray interferometer for time-resolved diagnostics of laser-aided nano-fabrication," in *International Conference on Ultrafast Phenomena*, 2010: Optical Society of America, p. TuE1.

[32] T. Sakka, S. Iwanaga, Y. H. Ogata, A. Matsunawa, and T. Takemoto, "Laser ablation at solid–liquid interfaces: An approach from optical emission spectra," *The Journal of Chemical Physics,* vol. 112, no. 19, pp. 8645-8653, 2000.

[33] R. Brause, H. Moeltgen, and K. Kleinermanns, "Characterization of laser-ablated and chemically reduced silver colloids in aqueous solution by UV/VIS spectroscopy and STM/SEM microscopy," *Applied Physics B,* vol. 75, no. 6, pp. 711-716, 2002.

[34] A. Henglein, "Physicochemical properties of small metal particles in solution:" microelectrode" reactions, chemisorption, composite metal particles, and the atom-to-metal transition," *The Journal of Physical Chemistry,* vol. 97, no. 21, pp. 5457-5471, 1993.

References

[35] A. Kawabata and R. Kubo, "Electronic properties of fine metallic particles. II. Plasma resonance absorption," *Journal of the physical society of Japan,* vol. 21, no. 9, pp. 1765-1772, 1966.

[36] Q. Wu, W.-s. Miao, H.-j. Gao, and D. Hui, "Mechanical properties of nanomaterials: A review," *Nanotechnology Reviews,* vol. 9, no. 1, pp. 259-273, 2020.

[37] S. Abdelbasir and A. E. Shalan, "Intriguing properties and applications of functional magnetic materials," *Functional Materials,* 2019.

[38] C. B. Hitz, *LEOMA and the US Laser Industry: The Good and Bad Moves for Trade Associations in Emerging High-tech Industries*. John Wiley & Sons, 2014.

[39] B. Prats-Mateu, P. Bock, M. Schroffenegger, J. L. Toca-Herrera, and N. Gierlinger, "Following laser induced changes of plant phenylpropanoids by Raman microscopy," *Scientific reports,* vol. 8, no. 1, pp. 1-12, 2018.

[40] J. Geusic, H. Marcos, and L. Van Uitert, "Laser oscillations in Nd- doped yttrium aluminum, yttrium gallium and gadolinium garnets," *Applied Physics Letters,* vol. 4, no. 10, pp. 182-184, 1964.

[41] C. Kittel and P. McEuen, *Kittel's Introduction to Solid State Physics*. John Wiley & Sons, 2018.

[42] J. T. Bell and G. T. Mola, "Improved charge transport in P3HT: PCBM bulk heterojunction PV cell under ambient environment," *Physica B: Condensed Matter,* vol. 437, pp. 63-66, 2014.

[43] M. F. C. Ladd, R. A. Palmer, and R. A. Palmer, *Structure determination by X-ray crystallography*. Springer, 1977.

[44] F. O. T. DESIGN and A. T. D. UNIT III, "TEXTBOOKS," *COURSE TITLE CATEGORY,* p. 4.

[45] D. Carlson *et al.*, *Amorphous semiconductors*. Springer, 1986.

References

[46] Ibraheim, Adil M., and Maki A. Sameer. "Effect of The Cu Doping on The Structural and Optical Properties of AlSb Thin Films Deposited by Thermal Evaporation Method." In Journal of Physics: Conference Series, vol. 1879, no. 3, p. 032121. IOP Publishing, 2021.

[47] D. K. Ferry, *Semiconductor transport*. CRC Press, 2016.

[48] J. Singh, *Electronic and optoelectronic properties of semiconductor structures*. Cambridge University Press, 2007.

[49] F. Abeles, "Optical properties of solids," 1972.

[50] A. Beiser, *Concepts of modern physics*. Tata McGraw-Hill Education, 2003.

[51] M. Dongol, "Effect of composition and annealing on some of the optical parameters of Gex Te100-x thin films," *Egyptian Journal of Solids*, vol. 23, pp. 297-306, 2000.

[52] C. F. Klingshirn, *Semiconductor optics*. Springer Science & Business Media, 2012.

[53] G. R. Fowles, *Introduction to modern optics*. Courier Corporation, 1989.

[54] Hilo, Mahmoud Hamid Mahmoud, and Amna Babikir. "Studying the Optical Properties of Cadmium Acetate Thin Films by UV-Vis Technique." International Journal of High Energy Physics 9, no. 1 (2022): 6."

[55] E. H. Ali and A. A. Nafie, "Diagnosis of Sickle Cell Anemia Using Laser Emission Spectroscopy among Sudanese Patients," *African Journal of Medical Sciences*, vol. 5, no. 10, 2020.

[56] J. A. Hutchby and R. L. Fudurich, "Theoretical analysis of Al x Ga1− x As-GaAs graded band- gap solar cell," *Journal of Applied Physics*, vol. 47, no. 7, pp. 3140-3151, 1976.

[57] I. M. Ali, I. M. Ibrahim, and I. S. Naji, "CV AND IV CHARACTERISTICS OF In2O3/GaAs HETEROJUNCTION," *Journal of Electron Devices*, vol. 17, pp. 1427-1432, 2013.

[58] S. O. Kasap, *Principles of electronic materials and devices*. McGraw-Hill New York, 2006.

[59] E. H. Falcao and F. Wudl, "Carbon allotropes: beyond graphite and diamond," *Journal of Chemical Technology & Biotechnology: International Research in Process, Environmental & Clean Technology,* vol. 82, no. 6, pp. 524-531, 2007.

[60] T. N. Hoheisel, S. Schrettl, R. Szilluweit, and H. Frauenrath, "Nanostructured carbonaceous materials from molecular precursors," *Angewandte Chemie International Edition,* vol. 49, no. 37, pp. 6496-6515, 2010.

[61] B. Draine and H. M. Lee, "Optical properties of interstellar graphite and silicate grains," *The Astrophysical Journal,* vol. 285, pp. 89-108, 1984.

[62] N. Baccile and M.-M. Titirici, "Proteins Induced Formation of Hydrothermal Nitrogen Doped Carbons," *MRS Online Proceedings Library,* vol. 1219, no. 1, pp. 4051-4056, 2009.

[63] W. Li *et al.*, "Flexible circuits and soft actuators by printing assembly of graphene," *ACS applied materials & interfaces,* vol. 8, no. 19, pp. 12369-12376, 2016.

[64] P. Cataldi, A. Athanassiou, and I. S. Bayer, "Graphene nanoplatelets-based advanced materials and recent progress in sustainable applications," *Applied Sciences,* vol. 8, no. 9, p. 1438, 2018.

[65] K. De Silva, H.-H. Huang, R. Joshi, and M. Yoshimura, "Chemical reduction of graphene oxide using green reductants," *Carbon,* vol. 119, pp. 190-199, 2017.

[66] A. Mallick, A. Mahapatra, A. Mitra, J.-M. Greneche, R. Ningthoujam, and P. Chakrabarti, "Magnetic properties and bio-medical applications in hyperthermia of lithium zinc ferrite nanoparticles integrated with reduced graphene oxide," *Journal of Applied Physics,* vol. 123, no. 5, p. 055103, 2018.

[67] J. Liu, Y. Xue, M. Zhang, and L. Dai, "Graphene-based materials for energy applications," *MRS bulletin,* vol. 37, no. 12, pp. 1265-1272, 2012.

[68] D. K. Gupta, R. S. Rajaura, and K. Sharma, "Synthesis and characterization of graphene oxide nanoparticles and their antibacterial activity," *Int. J. Environ. Sci. Technol,* vol. 1, no. 1, pp. 16-24, 2015.

[69] B. Paulchamy, G. Arthi, and B. Lignesh, "A simple approach to stepwise synthesis of graphene oxide nanomaterial," *J Nanomed Nanotechnol*, vol. 6, no. 1, p. 1, 2015.

[70] K. P. Loh, Q. Bao, G. Eda, and M. Chhowalla, "Graphene oxide as a chemically tunable platform for optical applications," *Nature chemistry,* vol. 2, no. 12, pp. 1015-1024, 2010.

[71] N.-F. Chiu, T.-Y. Huang, H.-C. Lai, and K.-C. Liu, "Graphene oxide-based SPR biosensor chip for immunoassay applications," *Nanoscale Research Letters,* vol. 9, no. 1, pp. 1-7, 2014.

[72] T.-F. Yeh, J. Cihlář, C.-Y. Chang, C. Cheng, and H. Teng, "Roles of graphene oxide in photocatalytic water splitting," *Materials Today,* vol. 16, no. 3, pp. 78-84, 2013.

[73] S. Paul and S. Mahanta, "Preparation and Characterization of Self-Assembled Graphene Oxide Supramolecular Structures," *Journal of Medical and Bioengineering Vol*, vol. 4, no. 6, 2015.

[74] H. M. Aziz, M. H. Al-Mamoori, and L. H. Aboud, "Synthesis and characterization of TiO2-rGO nanocomposite by pulsed laser ablation in liquid (PLAL-Method)," in *Journal of Physics: Conference Series*, 2021, vol. 1818, no. 1: IOP Publishing, p. 012206.

[75] Cao, Ning, and Yuan Zhang. "Study of reduced graphene oxide preparation by Hummers' method and related characterization." Journal of Nanomaterials 2015 (2015).

References

[76] C. A. Vélez *et al.*, "Glucose oxidation reaction at palladium-carbon nano-onions in alkaline media," *Journal of Solid State Electrochemistry,* vol. 25, no. 1, pp. 207-217, 2021.

[77] R. Joshi *et al.*, "Precise and ultrafast molecular sieving through graphene oxide membranes," *science,* vol. 343, no. 6172, pp. 752-754, 2014.

[78] C. K. Chua and M. Pumera, "Reduction of graphene oxide with substituted borohydrides," *Journal of Materials Chemistry A,* vol. 1, no. 5, pp. 1892-1898, 2013.

[79] G. Ijeomah, F. Samsuri, and M. A. M. Zawawi, "A review of surface engineering of Graphene for electrochemical sensing applications," *International Journal of Engineering Technology and Sciences,* vol. 4, no. 2, pp. 1-31, 2017.

[80] C. Gómez-Navarro *et al.*, "Electronic transport properties of individual chemically reduced graphene oxide sheets," *Nano Letters,* vol. 9, no. 5, pp. 2206-2206, 2009.

[81] G. Williams, B. Seger, and P. V. Kamat, "TiO2-graphene nanocomposites. UV-assisted photocatalytic reduction of graphene oxide," *ACS nano,* vol. 2, no. 7, pp. 1487-1491, 2008.

[82] Z. Wang, X. Zhou, J. Zhang, F. Boey, and H. Zhang, "Direct electrochemical reduction of single-layer graphene oxide and subsequent functionalization with glucose oxidase," *The Journal of Physical Chemistry C,* vol. 113, no. 32, pp. 14071-14075, 2009.

[83] M. M. Gottschlich, "Differential effects of three feeding regimens on tube feeding tolerance, clinical outcome, and selected nutritional and immunologic parameters in thermally injured patients.(Volumes I and II)," The Ohio State University, 1988.

References

[84] A. M. Mostafa, S. A. Yousef, W. H. Eisa, M. A. Ewaida, and E. A. Al-Ashkar, "Synthesis of cadmium oxide nanoparticles by pulsed laser ablation in liquid environment," *Optik,* vol. 144, pp. 679-684, 2017.

[85] M. Rehkämper, F. Wombacher, T. Horner, and Z. Xue, "Natural and anthropogenic Cd isotope variations," in *Handbook of environmental isotope geochemistry*: Springer, 2012, pp. 125-154.

[86] B. Kim and B.-K. Park, "Synthesis of self-aligned tellurium nanotubes by a sodium thiosulfate-assisted polyol method," *Electronic Materials Letters,* vol. 8, no. 1, pp. 33-36, 2012.

[87] F. Arab, M. Mousavi-Kamazani, and M. Salavati-Niasari, "Facile sonochemical synthesis of tellurium and tellurium dioxide nanoparticles: Reducing Te (IV) to Te via ultrasonic irradiation in methanol," *Ultrasonics Sonochemistry,* vol. 37, pp. 335-343, 2017.

[88] M. T. H. Aunkor, T. Raihan, S. H. Prodhan, H. Metselaar, S. U. F. Malik, and A. K. Azad, "Antibacterial activity of graphene oxide nanosheet against multidrug resistant superbugs isolated from infected patients," *Royal Society open science,* vol. 7, no. 7, p. 200640, 2020.

[89] A. N. Abd, M. F. Al-Marjani, and Z. A. Kadham, "Antibacterial activity of cadmium oxide nanoparticles synthesized by chemical method," *Journal of Multidisciplinary Engineering Science and Technology,* vol. 3, no. 6, pp. 5007-5011, 2016.

[90] M. Barani *et al.*, "Nanomaterials in the management of gram-negative bacterial infections," *Nanomaterials,* vol. 11, no. 10, p. 2535, 2021.

[91] C. L. Zhong, B. Y. Qin, X. Y. Xie, and Y. Bai, "Antioxidant and antimicrobial activity of tellurium dioxide nanoparticles sols," in *Journal of Nano Research*, 2013, vol. 25: Trans Tech Publ, pp. 8-15.

[92] A. Raghunath and E. Perumal, "Metal oxide nanoparticles as antimicrobial agents: a promise for the future," *International journal of antimicrobial agents,* vol. 49, no. 2, pp. 137-152, 2017.

[93] B. Salehi, E. Mortaz, and P. Tabarsi, "Comparison of antibacterial activities of cadmium oxide nanoparticles against Pseudomonas Aeruginosa and Staphylococcus Aureus bacteria," *Advanced biomedical research,* vol. 4, 2015.

[94] M. Shukla, S. Kumari, S. Shukla, and R. Shukla, "Potent antibacterial activity of nano CdO synthesized via microemulsion scheme," *J. Mater. Environ. Sci,* vol. 3, no. 4, pp. 678-685, 2012.

[95] Z. Azam *et al.,* "Microbial synthesized cadmium oxide nanoparticles induce oxidative stress and protein leakage in bacterial cells," *Microbial pathogenesis,* vol. 144, p. 104188, 2020.

[96] D. M. Cruz *et al.*, "Citric juice-mediated synthesis of tellurium nanoparticles with antimicrobial and anticancer properties," *Green Chemistry,* vol. 21, no. 8, pp. 1982-1998, 2019.

[97] P. K. Gupta, P. P. Sharma, A. Sharma, Z. H. Khan, and P. R. Solanki, "Electrochemical and antimicrobial activity of tellurium oxide nanoparticles," *Materials Science and Engineering: B,* vol. 211, pp. 166-172, 2016.

[98] M. C. Zambonino *et al.*, "Green synthesis of selenium and tellurium nanoparticles: current trends, biological properties and biomedical applications," *International Journal of Molecular Sciences,* vol. 22, no. 3, p. 989, 2021.

[99] E. Demir *et al.*, "Cytotoxicity and genotoxicity of cadmium oxide nanoparticles evaluated using in vitro assays," *Mutation Research/Genetic Toxicology and Environmental Mutagenesis,* vol. 850, p. 503149, 2020.

References

[100] A. Skheel, M. Jaduaa, and A. Abd, "Biosynthesis and characterization of CdO nanostructure and its influence on cancer cells of (HT29)," in *Journal of Physics: Conference Series*, 2021, vol. 1853, no. 1: IOP Publishing, p. 012047.

[101] M. Adeli-Sardou *et al.*, "Cytotoxicity and anti-biofilm activities of biogenic cadmium nanoparticles and cadmium nitrate: a preliminary study," 2022.

[102] S. T. Hossain and S. K. Mukherjee, "Toxicity of cadmium sulfide (CdS) nanoparticles against Escherichia coli and HeLa cells," *Journal of hazardous materials,* vol. 260, pp. 1073-1082, 2013.

[103] T. H. Nguyen, M. Lin, and A. Mustapha, "Toxicity of graphene oxide on intestinal bacteria and Caco-2 cells," *Journal of food protection,* vol. 78, no. 5, pp. 996-1002, 2015.

[104] D. Dambournet, I. Belharouak, and K. Amine, "Tailored preparation methods of TiO2 anatase, rutile, brookite: mechanism of formation and electrochemical properties," *Chemistry of materials,* vol. 22, no. 3, pp. 1173-1179, 2010.

[105] I. M. Tawfeeq and A. J. Mohammed, "Adsorption Ability and Kinetic of (Congo Red, Methyl Green) Dyes on Iraqi Siliceous Rocks," 2009.

[106] D. H. Everett, "Manual of symbols and terminology for physicochemical quantities and units, appendix II: Definitions, terminology and symbols in colloid and surface chemistry," *Pure and Applied Chemistry,* vol. 31, no. 4, pp. 577-638, 1972.

[107] P. Atkins, P. W. Atkins, and J. de Paula, *Atkins' physical chemistry*. Oxford university press, 2014.

[108] I. D. Brown, *The chemical bond in inorganic chemistry: the bond valence model*. Oxford University Press, 2016.

References

[109] Y. Li, H. Yi, X. Tang, F. Li, and Q. Yuan, "Adsorption separation of CO2/CH4 gas mixture on the commercial zeolites at atmospheric pressure," *Chemical Engineering Journal,* vol. 229, pp. 50-56, 2013.

[110] R. L. Ferriter, "Study of brine-crude oil interfacial tension, A," *1970-1979-Mines Theses & Dissertations,* 1973.

[111] A. Ndabigengesere, K. S. Narasiah, and B. G. Talbot, "Active agents and mechanism of coagulation of turbid waters using Moringa oleifera," *Water research,* vol. 29, no. 2, pp. 703-710, 1995.

[112] J. A. Schramke, S. F. Murphy, W. J. Doucette, and W. D. Hintze, "Prediction of aqueous diffusion coefficients for organic compounds at 25 C," *Chemosphere,* vol. 38, no. 10, pp. 2381-2406, 1999.

[113] E. Don-Pedro, "THE EFECTS OF SOIL PROPERTIES AND CLAY MINERALS ON THE BIOREMEDIATION OF SOILS CONTAMINATED WITH PENTACHLOROPHENOL," University of Akron, 2005.

[114] S. J. Randtke and V. L. Snoeyink, "Evaluating GAC adsorptive capacity," *Journal‐ American Water Works Association,* vol. 75, no. 8, pp. 406-413, 1983.

[115] S. J. Allen, Q. Gan, R. Matthews, and P. A. Johnson, "Mass transfer processes in the adsorption of basic dyes by peanut hulls," *Industrial & engineering chemistry research,* vol. 44, no. 6, pp. 1942-1949, 2005.

[116] A. Waheed, N. Baig, N. Ullah, and W. Falath, "Removal of hazardous dyes, toxic metal ions and organic pollutants from wastewater by using porous hyper-cross-linked polymeric materials: A review of recent advances," *Journal of Environmental Management,* vol. 287, p. 112360, 2021.

[117] A. Dakhel, "Effect of tellurium doping on the structural, optical, and electrical properties of CdO," *Solar Energy,* vol. 84, no. 8, pp. 1433-1438, 2010.

References

[118] A. Ersundu, M. Çelikbilek, N. Solak, and S. Aydın, "Characterization of glasses in the TeO2-WO3-CdO system," in *Materials Science and Technology Conference and Exhibition-MS&T'11*, 2011, pp. 48-51.

[119] H. L. Zhuang and R. G. Hennig, "Computational identification of single-layer CdO for electronic and optical applications," *Applied Physics Letters,* vol. 103, no. 21, p. 212102, 2013.

[120] S. Sönmezoğlu, T. Termeli, S. Akın, and İ. Askeroğlu, "Synthesis and characterization of tellurium-doped CdO nanoparticles thin films by sol–gel method," *Journal of sol-gel science and technology,* vol. 67, no. 1, pp. 97-104, 2013.

[121] Gao, Jie, Chengyan Liu, Lei Miao, Xiaoyang Wang, Chao Li, Rong Huang, Yu Chen, and Sakae Tanemura. "Power factor enhancement via simultaneous improvement of electrical conductivity and Seebeck coefficient in tellurium nanowires/reduced graphene oxide flexible thermoelectric films." Synthetic Metals 210 (2015): 342-351.

[122] S. Kumar, A. K. Ojha, and B. Walkenfort, "Cadmium oxide nanoparticles grown in situ on reduced graphene oxide for enhanced photocatalytic degradation of methylene blue dye under ultraviolet irradiation," *Journal of Photochemistry and Photobiology B: Biology,* vol. 159, pp. 111-119, 2016.

[123] Y. J. Zhang, P. Y. He, and H. Chen, "A novel CdO/graphene alkali-activated steel slag nanocomposite for photocatalytic degradation of dye wastewater," *Ferroelectrics,* vol. 522, no. 1, pp. 1-8, 2018.

[124] S. Goutham, N. Jayarambabu, C. Sandeep, K. K. Sadasivuni, D. S. Kumar, and K. V. Rao, "Resistive room temperature LPG sensor based on a graphene/CdO nanocomposite," *Microchimica Acta,* vol. 186, no. 2, pp. 1-8, 2019.

References

[125] S. Sadhukhan *et al.*, "Green synthesis of cadmium oxide decorated reduced graphene oxide nanocomposites and its electrical and antibacterial properties," *Materials Science and Engineering: C*, vol. 99, pp. 696-709, 2019.

[126] R. Hassanien, D. Z. Husein, and M. Khamis, "Novel green route to synthesize cadmium oxide@ graphene nanocomposite: optical properties and antimicrobial activity," *Materials Research Express*, vol. 6, no. 8, p. 085094, 2019.

[127] H. Wang *et al.*, "Optimization of Cadmium Adsorption by Magnetic Graphene Oxide Using a Fractional Factorial Design," *International Journal of Environmental Research and Public Health*, vol. 17, no. 18, p. 6648, 2020.

[128] A. P. Alegaonkar, S. K. Pardeshi, and P. S. Alegaonkar, "Tellurium-reduced graphene oxide two-dimensional (2D) architecture for efficient photo-catalytic effluent: Solution for industrial water waste," *Diamond and Related Materials*, vol. 108, p. 107994, 2020.

[129] D. Z. Husein, R. Hassanien, and M. Khamis, "Cadmium oxide nanoparticles/graphene composite: synthesis, theoretical insights into reactivity and adsorption study," *RSC advances*, vol. 11, no. 43, pp. 27027-27041, 2021.

[130] J. V. Meerloo, G. J. Kaspers, and J. Cloos, "Cell sensitivity assays: the MTT assay," in Cancer cell culture: Springer, 2011, pp. 237-245.

[131] P. Meleady and R. O'Connor, "General procedures for cell culture," in Cell Biology: Elsevier, 2006, pp. 13-2.0

[132] S. Viazzi, T. Lambrechts, J. Schrooten, I. Papantoniou, and J.-M. Aerts, "Real-time characterisation of the harvesting process for adherent mesenchymal stem cell cultures based on on-line imaging and model-based monitoring," Biosystems Engineering ،vol. 138, pp. 104-113, 2015

[133] S. Stankovich et al., "Graphene-based composite materials," nature, vol. 442, no. 7100, pp. 282-286, 2006.

[134] R. Swan, A. Ray, and C. Hogarth, "Optical absorption in thin tellurium films," physica status solidi (a), vol. 127, no. 2, pp. 555-560, 1991.

[135] G. Somasundaram, J. Rajan, P. Sangaiya, and R. Dilip, "Hydrothermal synthesis of CdO nanoparticles for photocatalytic and antimicrobial activities," Results in Materials, vol. 4, p. 100044, 2019.

[136] M. Jahanshahi, A. Morad Rashidi, and A. Asghar Ghoreyshi, "Synthesis and characterization of thermally-reduced graphene," Iranian (Iranica) Journal of Energy & Environment, vol. 4, no. 1, 2013.

[137] G. Upender and M. Prasad, "Raman, FTIR, thermal and optical properties of TeO2-Nb2O5-B2O3-V2O5 quaternary glass system," Journal of Taibah University for Science, vol. 11, no. 4, pp. 583-592, 2017.

[138] K. Sujatha, S. Sharmila, A. Sudha, and O. Shanmugasundaram, "Surfactant assisted spectroscopic application of cadmium oxide nanoparticles prepared via co-precipitation method," Materials Today: Proceedings, vol. 50, pp. 48-52, 2022.

[139] A. K. Jeryo and Q. A. Abbas, "Synthesis of Graphene Oxide Nanoparticles by Laser Ablation System," Iraqi Journal of Science, pp. 2241-2250, 2020.

[140] S. K. Mahto, T. Vinod, J.-K .Kim, and S.-W. Rhee, "Cytotoxic potentials of tellurium nanowires in BALB/3T3 fibroblast cells," Bulletin of the Korean Chemical Society, vol. 32, no. 9, pp. 3405-3410, 2011.

[141] A. Aldwayyan et al., "Synthesis and characterization of CdO nanoparticles starting from organometalic dmphen-CdI2 complex," Int. J. Electrochem. Sci, vol. 8, no. 8, pp. 10506-10514, 2013.

[142] R. C. Molina-Quiroz, C. M. Muñoz-Villagrán, E. De La Torre, J. C. Tantaleán, C. C. Vásquez, and J. M. Pérez-Donoso, "Enhancing the antibiotic antibacterial effect by sub lethal tellurite concentrations: tellurite and cefotaxime act synergistically in Escherichia coli," PloS one, vol. 7, no. 4, p. e35452, 2012.

[143] C. L. Zhong, B. Y. Qin, X. Y. Xie, and Y. Bai, "Antioxidant and antimicrobial activity of tellurium dioxide nanoparticles sols," in Journal of Nano Research, 2013, vol. 25: Trans Tech Publ, pp. 8-15 .

[144] B. Salehi, E. Mortaz, and P. Tabarsi, "Comparison of antibacterial activities of cadmium oxide nanoparticles against Pseudomonas Aeruginosa and Staphylococcus Aureus bacteria," Advanced biomedical research, vol. 4, 2015.

[145] M. Shukla, S. Kumari, S. Shukla, and R. Shukla, "Potent antibacterial activity of nano CdO synthesized via microemulsion scheme," J. Mater. Environ. Sci, vol. 3, no. 4, pp. 678-685, 2012.

[146] L. Ou et al., "Toxicity of graphene-family nanoparticles: a general review of the origins and mechanisms," Particle and fibre toxicology, vol. 13, no. 1, pp. 1-24, 2016.

[147] K. E. Zakrzewska et al., "Analysis of the cytotoxicity of carbon-based nanoparticles, diamond and graphite, in human glioblastoma and hepatoma cell lines," PloS one, vol. 10, no. 3, p. e0122579, 2015.

[148] H. Wen et al., "Comparative study of the cytotoxicity of the nanosized and microsized tellurium powders on HeLa cells," Frontiers in biology, vol. 8, no. 4, pp. 444-450, 2013.

[149] D. Lomelí-Marroquín *et al.*, "Starch-mediated synthesis of mono-and bimetallic silver/gold nanoparticles as antimicrobial and anticancer agents," *International journal of nanomedicine*, vol. 14, p. 2171, 2019.